

---

# SVD PERSPECTIVES FOR AUGMENTING DEEPONET FLEXIBILITY AND INTERPRETABILITY

---

**Simone Venturi**

Extreme Scale Data Science & Analytics  
Sandia National Laboratories  
Livermore, CA, 94550  
sventur@sandia.gov

**Tiernan Casey**

Extreme Scale Data Science & Analytics  
Sandia National Laboratories  
Livermore, CA, 94550  
tcasey@sandia.gov

April 28, 2022

## ABSTRACT

Deep operator networks (DeepONets) are powerful and flexible architectures that are attracting attention in multiple fields due to their utility for fast and accurate emulation of complex dynamics. As their remarkable generalization capabilities are primarily enabled by their projection-based attribute, in this paper, we investigate connections with low-rank techniques derived from the singular value decomposition (SVD). We demonstrate that some of the concepts behind proper orthogonal decomposition (POD)-neural networks can improve DeepONet’s design and training phases. These ideas lead us to a methodology extension that we name SVD-DeepONet. Moreover, through multiple SVD analyses of scenario- and time-aggregated snapshots matrices, we find that DeepONet inherits from its projection-based attribute strong inefficiencies in representing dynamics characterized by symmetries. Inspired by the work on shifted-POD, we develop flexDeepONet, an architecture enhancement that relies on a pre-transformation network for generating a moving reference frame and isolating the rigid components of the dynamics. In this way, the physics can be represented on a latent space free from rotations, translations, and stretches, and an accurate projection can be performed to a low-dimensional basis. In addition to improving DeepONet’s flexibility and interpretability, the proposed perspectives increase its generalization capabilities and computational efficiencies. For instance, we show flexDeepONet can accurately surrogate the dynamics of 19 thermodynamic variables in a combustion chemistry application by relying on 95% less trainable parameters than the ones of the “vanilla” architecture. As stressed in the paper, we argue that DeepONet and SVD-based methods can reciprocally benefit from each other. In particular, the flexibility of the former in leveraging multiple data sources and multifidelity knowledge in the form of both unstructured data and physics-informed constraints has the potential to greatly extend the applicability of methodologies such as POD and principal component analysis (PCA).

**Keywords** Deep learning, Scientific machine learning, Surrogate models, Neural Operators, DeepONet, SVD, PCA, POD with symmetries, Combustion

## 1. Introduction

The computational burden required to numerically solve partial differential equations (PDEs) for complex systems still precludes their application to numerous real-world problems that need fast predictions (e.g., predictive control) or a large number of replicas (e.g., optimization and uncertainty quantification). As significant progress has been made in exploiting machine learning (ML) techniques to reduce these computational costs in many fields, expensive fully physics-based simulations are being replaced with efficient ML-based surrogates [1–3]. Given that they can integrate multifidelity observational data [4] and enforce physical laws [5, 6], these emulators are able to achieve high predictive accuracy for a broad spectrum of problems [7]: from contexts involving small amounts of available data and extensively known physics, to cases of big data and fully missing physics.

In the last few years, multiple research communities worldwide have been attracted by a particular subclass of ML-based surrogates, called neural operators [8–19]. These emulators can learn the physical system at the operator level, and they are then effective in predicting the system responses under different initial/boundary conditions, forcing terms, or PDE parameters. Among the variety of techniques that have been recently proposed, the Deep Operator Network (DeepONet) by Lu *et al.* [12, 13] has become one of the methods of choice primarily because of the low generalization errors, simplicity of implementation, fast learning with respect to the training data, and high flexibility. In fact, one of its main strengths is the capability of being trained by multifidelity data or by heterogeneous sources of experimental data and simulations [20–22]. Additionally, DeepONet’s building blocks are not constrained to a particular architecture, and they can be implemented in multiple ways (e.g., as feed-forward neural networks (FNNs) or convolutional neural networks (CNNs)). Since it was introduced in 2019, DeepONet has been successfully applied to operator surrogation in various fields, including fluid and gas dynamics [23–26], combustion [27], hypersonics [28–30], energy conversion [31], material science [32, 33], medicine [34], seismology [35], and finance [36, 37]. Physics-informed extensions (PI-DeepONets) have also been proposed to enforce known physical constraints [32, 38–40].

DeepONet’s approach to surrogate construction relies on uncovering a projection that approximates the operator with good accuracy. The bases of this projection are assumed to be nonlinear functions of the operator’s independent variables (e.g., time and spatial coordinates), while the components are constructed as nonlinear functions of the operator input (e.g., initial conditions). DeepONet autonomously discovers the appropriate projection from the data at the training phase by learning the coefficients of two separate networks, called branch and trunk nets, which approximate the coefficients-to-input and basis-to-independent-variables mappings.

As the projection is the keystone of DeepONet, this paper aims to draw analogies with other techniques that detect suitable bases for representing data and/or describing dynamics. In particular, we focus on linking the DeepONet to methodologies derived from the singular value decomposition (SVD) [41–43], such as the proper orthogonal decomposition (POD) [44–47]. While ongoing work is focused on formalizing and contextualizing these parallelisms to the standpoint of PDEs, similarities and contrasts are highlighted in this paper mainly through the investigation of test cases built upon ordinary differential equations (ODEs). It is worth noticing that PDEs reduce to coupled ODEs in the method of lines discretization used in most numerical treatments of differential equations in continuum mechanics. We choose a mass-spring-damper model as the first problem to address the DeepONet components’ interpretability. A novel SVD-DeepONet is constructed by fitting the data set to the basis and the coefficients of the  $\ell_2$ -optimal projection using trunk and branch nets. Resemblances with the recently developed POD-DeepONet approach by Lu *et al.* are also discussed. Despite the instructive attribute of the SVD-formulation and its practical benefits for some fully data-driven applications, the analysis also allows us to stress the numerous advantages of the original DeepONet [12, 13] for real-world problems.

The second test case that we study is a toy problem in which the evolution of a dynamical state is described as a hyperbolic tangent shifted in time as a function of an initial condition. While lacking an explicit physical analog, the system calls attention to the limitation of DeepONet in describing dynamics characterized by translations. We conjecture that this shortcoming is traceable to the DeepONet being a linear projection-based method and, as such, being inefficient in processing symmetries that include translations, rotations, and stretchings [48]. However, rather than fully revolutionizing the architecture and renouncing the advantages of a linear subspace for the complexity of non-linear manifolds, we propose a simple but effective modification. Similar to what was independently developed by Hadorn [49], we introduce an additional building block, which we call a pre-transformation network. This aims to discover a moving reference frame with respect to which the multiple scenarios can be efficiently summarized by fewer modes. We refer to this augmented structure as a flexible DeepONet (flexDeepONet). We also discuss similarities with the shifted-POD methods [50–52] developed for overcoming the issue arising from symmetries in transport-dominated flows.

This toy problem is propaedeutic to the third test case, a combustion chemistry model in an idealized homogeneous reactor with a zero-spatial variation assumption, such that gradient-based mass transport effects are ignored. As for the previous system, the dynamics are also characterized by symmetries that cause noticeable oscillations in the vanilla DeepONet architecture’s predictions and prevent it from achieving high precision. As formerly adopted by Lu *et al.* [53], here and in what follows, the adjective “vanilla” simply refers to the unmodified version of the DeepONet architecture as firstly introduced in [12, 13]. This regression task for the chemical system time integration is also complicated by the large number of thermodynamic variables involved and by their different orders of magnitude.

While the first three test cases aim to show that various ideas previously developed for SVD-based methods can further improve DeepONet’s flexibility and generalization capabilities, the fourth problem we present has the purpose of showing that DeepONet’s architecture and training paradigm can also benefit the generic projection-based methods. In the last test case, we study the dynamics of a rigid body that rotates, translates, and stretches with time. Due to the complex rigid motions involved, classical POD analysis would require a large number of POD modes (more than 150) to characterize the dynamics accurately. Despite that, flex-DeepONet is found to be an efficient and effective surrogate capable of accurate predictions even at spatial locations outside the training domain.

The paper is organized as follows. Sec. 2 summarizes the DeepONet approach and the SVD-derived methodologies. In

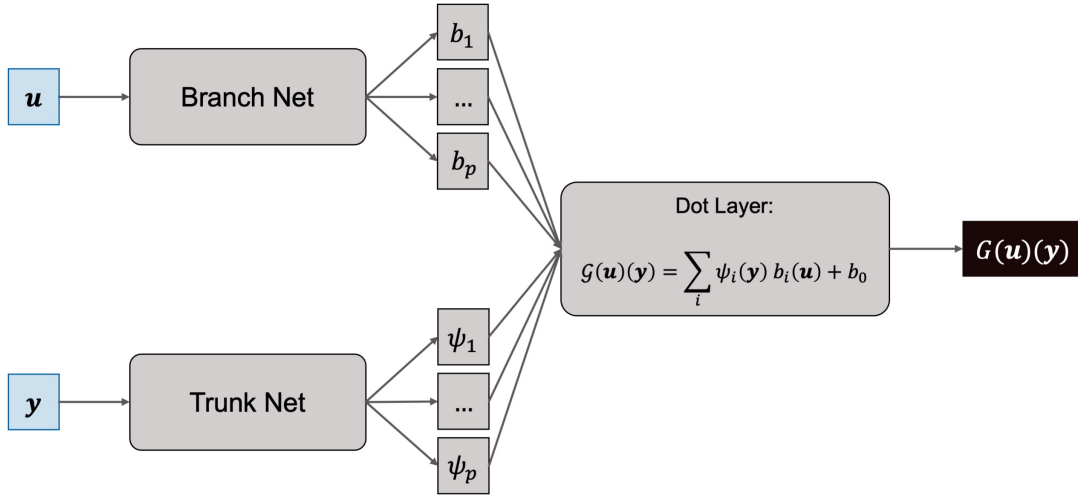


Figure 1: **Architecture of the (unstacked) vanilla DeepONet** [12, 13].

Sec. 3, we apply the DeepONet to the four test cases: i) a mass-spring-damper system, ii) a shifting hyperbolic tangent function, iii) a chemical system in an isobaric reactor undergoing combustion processes, and iv) a two-dimensional rigid body that translates, rotates, and stretches in time. We analyze the drawbacks of the vanilla architecture and propose improvements in light of analogies with SVD-based methods. Finally, Sec. 5 summarizes the findings and outlines future directions.

## 2. Methods

This section introduces the Deep Operator Network (DeepONet) approach to operator regression and the singular value decomposition (SVD) along with the techniques derived from it. By analyzing four test cases, Sec. 3 will link these two families of methodologies and propose extensions in light of their connections.

### 2.1. Deep Operator Networks (DeepONets)

As in all the neural operator approaches, a deep operator network (DeepONet) [12, 13] aims to learn an operator,  $\mathcal{G}$ , that takes an input function  $\mathbf{u}$  (e.g., initial conditions, boundary conditions, forcing terms) and gives an output function  $\mathcal{G}(\mathbf{u})$ . When this last quantity is evaluated at any point in the space of the independent variables,  $\mathbf{y}$  (e.g., spatial coordinates and/or time instants), the result is a real number,  $\mathcal{G}(\mathbf{u})(\mathbf{y})$ . In the following, we will refer to the values of  $\mathbf{y}$  as time instants or locations, and the dynamics corresponding to different  $\mathbf{u}$  as scenarios. Therefore, a scenario is a time-evolving solution corresponding to any particular initial value of  $\mathbf{u}$ .

The DeepONet architecture has been heavily inspired by the universal approximation theorem for operators by Chen and Chen [11], which states that a neural network (NN) with a single hidden layer can accurately approximate any nonlinear continuous functional and operator. The theorem has been later extended to deep NNs [13]. Of the four marginally different DeepONet structures introduced by the original paper [13], we consider “vanilla” the architecture corresponding to an unstacked configuration with bias, which is also the one with the lowest generalization errors. The DeepONet is composed of two subnetworks: i) the branch net, that generates the  $p$ -dimensional vector  $\mathbf{b}$  by encoding the input functions,  $\mathbf{u}$ , at fixed sensor points, and ii) a trunk net, that produces the  $p$ -dimensional vector  $\boldsymbol{\psi}$  by encoding the independent variables,  $\mathbf{y}$ . In order to predict the operator’s value, the latent outputs  $\mathbf{b}$  and  $\boldsymbol{\psi}$  are then merged via a dot product layer, which can also include a trainable bias  $b_0$  [13]. The resulting architecture is illustrated in Fig. 1. The DeepONet approach comes with theoretical guarantees of universal approximation by construction. Additionally, recent works theorized the upper bounds for the approximation error in terms of network size, operator type, and data regularity [54, 55] and showed that DeepONets can approximate the solution operators of elliptic PDEs with exponential accuracy [56].

To construct and train the vanilla DeepONet and the extensions proposed in this paper (see Sec. 3), we utilize the ROMNet software package (i.e., neural Networks for Reduced-Order Modeling), a toolbox developed within Sandia National Laboratories that relies on the Tensorflow library [57]. In this work, all the building blocks are implemented as

feed-forward neural networks (FNNs), and all the training is performed by applying the Adam optimizer [58] and using mean squared error (MSE) as the loss function.

## 2.2. Singular Value Decomposition (SVD)

The singular value decomposition (SVD) [41–43] is a technique that extracts low-rank patterns from high-dimensional data without any knowledge or constraints arising from the underlying physics. The main strengths of SVD compared to other decompositions are i) its numerical robustness and efficiency, ii) the fact that it provides a hierarchical representation of the data, and iii) its existence for any matrix, including those that are non-square. SVD is the underlying algorithm of many ubiquitous analysis methods in science and engineering. Most of them have been independently proposed for dimensionality reduction, and they mainly differ in the way they pre-process the data [48]. Some examples include principal component analysis (PCA) [59–62], proper orthogonal decomposition (POD) [44–47], the Karhunen-Loeve transform [63, 64], singular value expansion (SVE) [65], and dynamic mode decomposition (DMD) [66–68]. In the following, we will briefly outline the SVD approach, and details about the methodology can be found in [48, 69].

For a given data matrix  $\mathbf{X} \in \mathbb{C}^{n \times m}$ , there exists a unique decomposition:

$$\mathbf{X} = \mathbf{U}\mathbf{\Sigma}\mathbf{V}^*, \quad (1)$$

where  $\mathbf{U} \in \mathbb{C}^{n \times n}$  and  $\mathbf{V} \in \mathbb{C}^{m \times m}$  are unitary matrices.  $\mathbf{\Sigma} \in \mathbb{C}^{n \times m}$  is a real non-negative diagonal matrix, and its non-zero values (i.e.,  $\sigma_i = \Sigma_{i,i}$ ) are ranked in descending order (i.e.,  $\sigma_1 \geq \sigma_i \geq \sigma_m$ ). The columns of  $\mathbf{X}$  are typically referred to as snapshots, those of  $\mathbf{U}$  and  $\mathbf{V}$  are named left and right singular vectors respectively, and  $\sigma_i$  are referred to as singular values. If we now truncate  $\mathbf{\Sigma}$ ,  $\mathbf{U}$ , and  $\mathbf{V}$  by retaining only the largest  $r$  singular values and their associated vectors, it can be proved that the resulting rank- $r$  approximation:

$$\mathbf{X} \approx \tilde{\mathbf{U}}\tilde{\mathbf{\Sigma}}\tilde{\mathbf{V}}^* \quad (2)$$

is optimal in the  $\ell_2$  sense, where  $\tilde{\mathbf{U}}$ ,  $\tilde{\mathbf{\Sigma}}$ , and  $\tilde{\mathbf{V}}$  represent the truncated matrices. POD-based methods rely on the columns of  $\tilde{\mathbf{U}}$  as optimal modes, and employs them as low-rank, orthogonal basis to represent the dynamics [48].

If we assume that  $\mathbf{X}$  is centered (i.e., the mean values of its columns are equal to zero), we can construct its  $m \times m$  column-wise covariance matrix as:

$$\mathbf{C} = \frac{\mathbf{X}^*\mathbf{X}}{n-1} = \mathbf{V} \frac{\mathbf{\Sigma}^2}{n-1} \mathbf{V}^*. \quad (3)$$

Recalling that  $\mathbf{V}$  is unitary, Eq. 3 corresponds to the diagonalization of  $\mathbf{C}$  (i.e.,  $\mathbf{C} = \mathbf{V}\mathbf{\Lambda}\mathbf{V}^*$ , with  $\mathbf{\Lambda} = \mathbf{\Sigma}^2/(n-1)$ ). Following the PCA nomenclature, the columns of  $\mathbf{V}$  are also called principal directions (or principal axes), as they are the eigenvectors corresponding to the column-wise covariance matrix. Moreover, because they are organized in descending order based on  $\lambda_i = \sigma_i^2/(n-1)$ , these columns capture decreasing contributions to the covariance with increasing  $i$ . The projection of  $\mathbf{X}$  in the principal directions gives the principal components (or scores):

$$\mathbf{U}\mathbf{\Sigma} = \mathbf{X}\mathbf{V}. \quad (4)$$

From this perspective, the approximation of  $\mathbf{X}$  in Eq. 2 can be rewritten as:

$$\mathbf{X} \approx \mathbf{\Phi}_x \mathbf{A}_x^* = \sum_{i=1}^{N_\phi} \phi_{x_i} \alpha_{x_i}^* \quad (5)$$

where  $N_\phi = r$  is the number of retained singular values,  $\mathbf{\Phi}_x = \tilde{\mathbf{U}}\tilde{\mathbf{\Sigma}}$  represents the reduced principal components and has dimensions  $[n \times N_\phi]$ , while  $\mathbf{A}_x = \tilde{\mathbf{V}}$  corresponds to the reduced principal directions and has dimensions  $[m \times N_\phi]$ . For some of the SVD-derived methods to work properly and so that the decomposition can focus only on the relevant variations, the snapshots matrix needs to be first centered by representing the components of each column as deviations about their mean values. Additional common practice is to scale the centered snapshots matrix for (de-)emphasizing correlations among different groups of columns, especially if these have different units and vary over different scales. For example, auto-scaling produces snapshots with unitary standard deviations in order for the SVD to analyze the data based on correlations instead of covariances. In contrast, variable stability (VAST) scaling reserves higher importance to columns that do not show strong variation. Descriptions of the centering and scaling techniques and their effects on data reduction can be found in [70–73]. To include centering and scaling into our analysis, we allow for a generic pre-processing step to transform the raw-data snapshots matrix,  $\mathbf{X}_{Raw}$ , before SVD is performed:

$$\mathbf{x}_i = \frac{\mathbf{x}_{Raw_i} - c_{x_i}}{d_{x_i}}, \quad (6)$$

where  $\mathbf{x}_{Raw_i}$  and  $\mathbf{x}_i$  respectively represent the  $i$ -th columns of the raw-data and pre-processed snapshots matrix. Additionally,  $c_{x_i}$  and  $d_{x_i}$  respectively indicate the components of the  $\mathbf{c}_x$  and  $\mathbf{d}_x$  centering and scaling vectors, both with dimensions  $[n \times 1]$ .



### 3. Results

In this section, the DeepONet is applied to four test cases, which have been selected *ad hoc* to highlight the approach’s effectiveness, draw connections with SVD-derived methodologies, and propose improvements in light of these. The first analysis that we carry out involves employing DeepONets to learn the operator characterizing a mass-spring-damper model. This physical system is chosen for the simplicity of the underlying ODEs and the presence of multiple state variables as a prelude to the multi-dimensional state spaces typical of physics applications. The second investigation focuses on a toy problem constructed by representing the time evolution of a single state variable as a hyperbolic tangent affected by a delay proportional to the initial condition. Despite the resulting ODE lacking a direct physical analog, this simple test case highlights and motivates some limitations of the original DeepONet architecture. Moreover, the problem is propaedeutical to the third test case of direct physical relevance, involving combustion chemistry in a zero-dimensional isobaric reactor, characterized by 19 thermodynamic variables. Finally, the fourth problem focuses on a rigid body that rotates, translates, and stretches as non-linear functions of time.

#### 3.1. Test Case 1: Mass-Spring-Damper System

We start by analyzing a simple mass-spring-damper model under the assumption of no external forcing term acting on the body. The system can be described by the following linear ODEs:

$$\begin{bmatrix} \frac{dx(t)}{dt} \\ \frac{dv(t)}{dt} \end{bmatrix} = \begin{bmatrix} 0 & 1 \\ -\frac{k}{m} & -\frac{c}{m} \end{bmatrix} \begin{bmatrix} x \\ v \end{bmatrix}, \quad (7)$$

$$\begin{bmatrix} x(0) \\ v(0) \end{bmatrix} = \begin{bmatrix} x_0 \\ v_0 \end{bmatrix}, \quad (8)$$

where  $x$  and  $v$  represent the body’s displacement and velocity respectively, while  $k$ ,  $c$ , and  $m$  represent the spring constant, the damping coefficients, and the body’s mass. In the following, the values of these three parameters are set to 3 [N/m], 0.5 [N s/m], and 1 [kg], respectively. One hundred pairs of  $x_0$  and  $v_0$  initial conditions (i.e.,  $N_S=100$ ) are randomly sampled in the space  $(x_0, v_0) \in (-4, 4)$  [m]  $\times$   $(-4, 4)$  [m/s] based on a Latin hypercube strategy [74], and collected in a  $[N_S \times 2]$  matrix,  $[x_0, v_0]$ . For each of these scenarios, the system is integrated in time, and the  $x$  and  $v$  variables are collected at five hundred time instances (i.e.,  $N_t=500$ ) equally spaced between 0 and 15 [s], composing the vector  $\mathbf{t}_S$ . The resulting 50,000 data points are used to train a vanilla DeepONet characterized by the structure in Fig. S2. Figure 2A compares the displacements and velocities predicted by the surrogate at five test scenarios, unseen during training, with those obtained via direct time integration. The DeepONet performs well despite the output layers of its branch and trunk nets being composed of only two neurons (i.e.,  $p = 2$ ). This means that the operator information content learned through the sampled scenarios is effectively summarized by the four outputs of the  $x$  and  $v$  trunk nets, which are shown in Fig. 2B. We now propose an alternative approach to the construction of DeepONet-based surrogates under the perspective of the singular value expansion (SVE) [65, 75]. Beforehand, we concatenate displacements and velocities from different scenarios as multiple columns of two data matrices,  $\mathbf{X}_{Raw}$  and  $\mathbf{V}_{Raw}$ , with dimensions  $[N_t \times N_S]$ . When performing SVD on matrices assembled in this way we refer to this as scenario-aggregated SVD, as each column is a snapshot of the dynamics arising from a specific initial condition, or scenario. We highlight that in the case of a generic time-and-space-dependent PDE, the columns of the resulting scenario-aggregated snapshots matrices would contain the full spatio-temporal solution for a given scenario. This contrasts with the POD-based methods, for which each snapshot represents a spatially varying solution, and different columns correspond to different time instants. That being said, we center each of the matrices’ columns and generate the scenario-dependent vectors  $\mathbf{c}_x$  and  $\mathbf{c}_v$ . We then perform auto-scaling (i.e., scale each of the columns based on its standard deviation), obtaining the scenario-dependent vectors  $\mathbf{d}_x$  and  $\mathbf{d}_v$ . At this point, we carry out the singular value decompositions and produce the corresponding matrices  $\Phi_x$ ,  $\mathbf{A}_x$ ,  $\Phi_v$ , and  $\mathbf{A}_v$  based on Eq. 9. Schematics are presented in Figs. 3 and S4. Consistent with the vanilla DeepONet’s predictions for  $x$  and  $v$  being effectively summarized by two trunk outputs each, two singular values are sufficient for effectively decomposing both  $\mathbf{X}$  and  $\mathbf{V}$ . In fact, the cumulative energy content of their first two singular values exceeds 99.9999%, and the resulting encoding-decoding errors are below machine precision. For the application under analysis, we also note that such reductive effectiveness does not depend on the choice of centering and scaling.

Subsequently, two feed-forward neural networks (FNNs) with one input and two outputs each are constructed to regress  $x$  and  $v$ ’s principal components as functions of time. These blocks are independently trained in a fully data-driven fashion by relying on the data points  $(\mathbf{t}_s; \Phi_x)$  and  $(\mathbf{t}_s; \Phi_v)$ , respectively. Here and in the following, we want to communicate through the notation  $(\mathbf{I}; \mathbf{O})$  that the surrogate’s training is performed by taking the  $\mathbf{I}$  data matrix as input and comparing the resulting output with the  $\mathbf{O}$  data matrix. Two additional FNNs with two inputs and four outputs

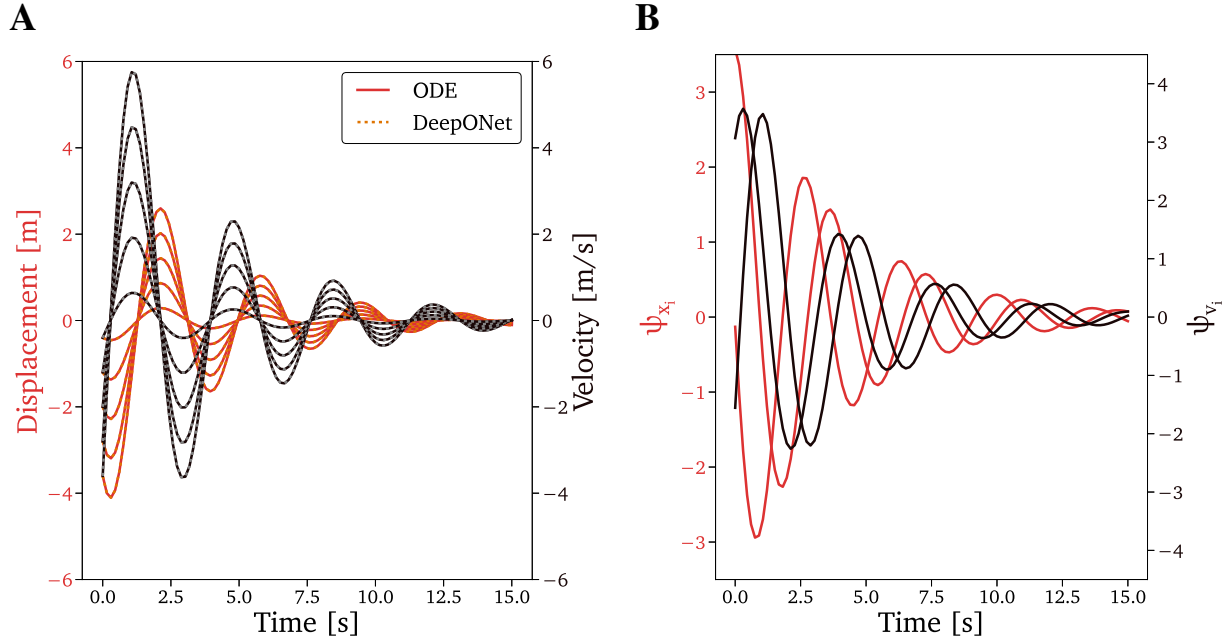


Figure 2: Vanilla DeepONet applied to the mass-spring-damper test case. (A): Displacements and velocities at five test scenarios as the results of the ODE integration (solid lines) and as predicted by the DeepONet (overlapping dotted lines). (B): Outputs of the trunk nets for displacements (red curves) and velocities (black curves). See Fig. S2 for details about the vanilla DeepONet’s structure.

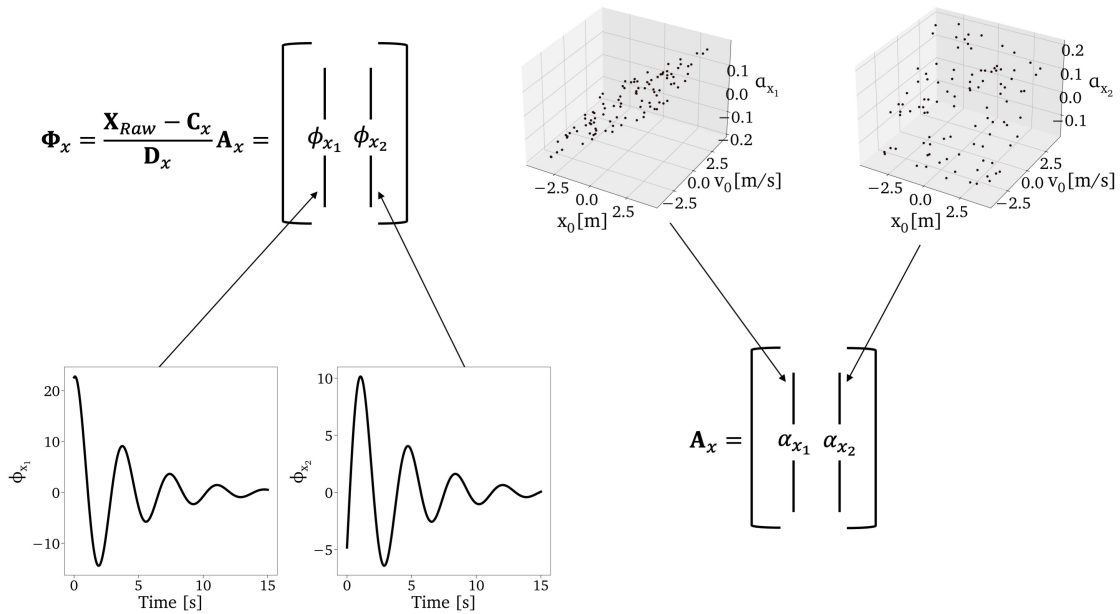


Figure 3: **SVD of the displacement data matrix.** Schematics of the columns resulting from the decomposition.

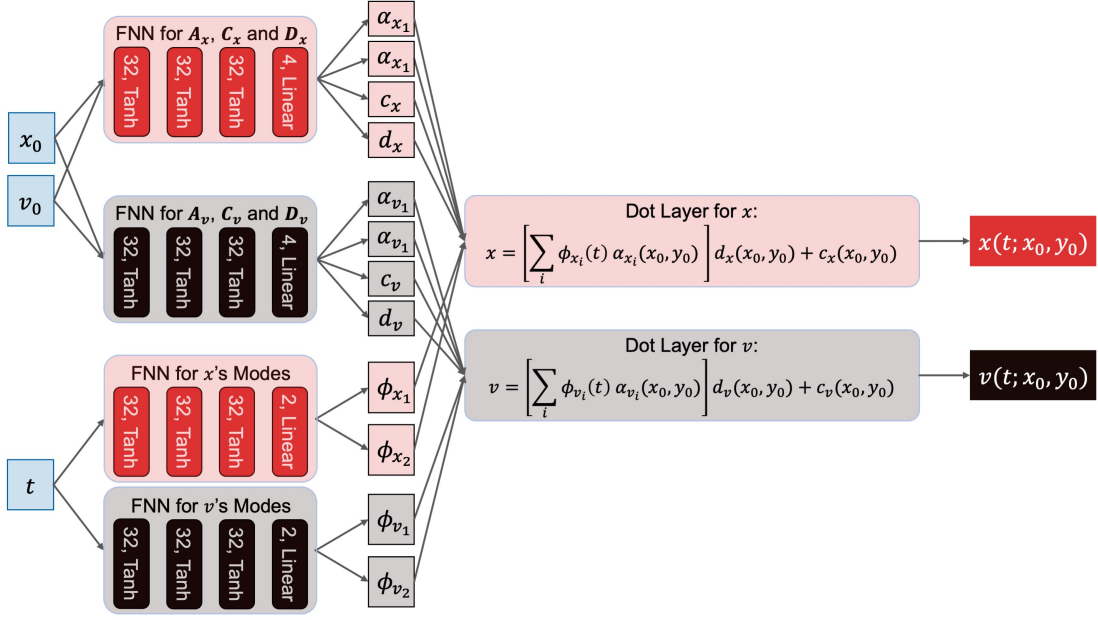


Figure 4: **Assembled architecture of the SVD-DeepONet for the mass-spring-damper test case.** After being independently trained as feed-forward neural networks (FNNs), the four blocks are assembled as DeepONet’s trunk nets and branch nets to predict displacements and velocities at unseen times and for unseen initial conditions.

each are generated to regress  $x$  and  $v$ ’s principal directions as functions of the initial conditions. These blocks are also independently trained in a fully data-driven fashion by relying on the data points  $([x_0, v_0]; \mathbf{B}_x)$  and  $([x_0, v_0]; \mathbf{B}_v)$ , respectively. Here, the generic  $\mathbf{B}_j$  matrix is constructed by concatenating  $\mathbf{A}_j$ , the vector  $\mathbf{c}_j$ , and the vector  $\mathbf{d}_j$ :

$$\mathbf{B}_j = \begin{bmatrix} \alpha_{1_j} & \alpha_{2_j} & c_j & d_j \end{bmatrix}, \quad (9)$$

with  $j \in \{x, v\}$ . A visual outline of these steps is shown in Fig. S5. Finally, in the last phase, the four FNNs are assembled as trunk and branch nets of a DeepONet that does not require any additional training, as its prediction phase relies on the parameters already learned during the sub-nets’ calibrations and simply involves the evaluation of the blocks and dot product layer. We call this explicit SVD-inspired construction and training approach SVD-DeepONet. Figures 4 and 5 respectively sketch the architecture and show the resulting predictions for unseen scenarios, which are in excellent agreement with the time-integrated dynamics. The present work draws similar connections between SVD-derived techniques and DeepONets as some recent works. In particular, Meuris *et al.* interpreted the trunk outputs as unprocessed POD modes. After extracting and transforming them into hierarchical orthonormal basis, they used these outputs to expand the solutions of time-dependent PDEs [76]. Almost simultaneously, Lu *et al.* developed the POD-DeepONet approach by performing POD on the training data, employing the resulting modes as the trunk net, and using the branch net to learn the coefficients of the decomposition while training the DeepONet [53, 77]. From this perspective, the SVD-DeepONet presented in this work consists of three main modifications of the POD-DeepONet approach: i) the trunks are FNNs that fit the principal components, rather than being POD modes, ii) the branches recover the principal directions, rather than the POD coefficients, and iii) the training of the branches do not involve the trunk nets. This last attribute is in analogy with the offline stage of the POD-neural network (POD-NN) method by Hesthaven *et al.* [78, 79]. In other words, SVD-DeepONet trains trunks and branches as fully-independent FNNs, and it assembles these building blocks as the DeepONet architecture only at the prediction phase. One advantage of this approach is a simplification of the training stage compared to the POD-DeepONet. Particularly, the resulting embarrassingly parallelizable workload has vast implications in the case of stacked [12, 13, 53] POD-DeepONets, which contain one branch net for each of the projection matrix’s columns. As an additional example, if the DeepONet’s building blocks involve multiple libraries or coding languages (e.g., trunk nets constructed as polynomial chaos expansions by relying on legacy code or libraries), the training of the assembled DeepONet requires the breakage of the full-architecture’s graph within the training and increases the computational costs. In contrast SVD-DeepONet would not have to face these issues, as each of the building blocks can separately rely on its own library during calibration. For the sake of completeness, it is worth mentioning that, as for POD-DeepONet, SVD-DeepONet shares similarities

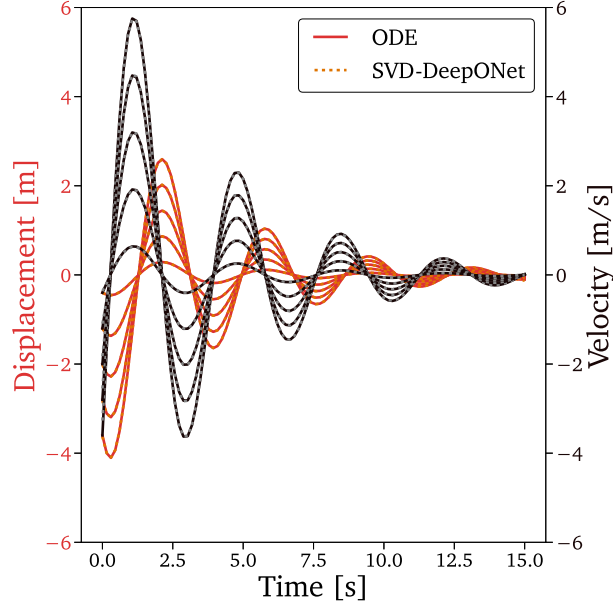


Figure 5: **SVD-DeepONet applied to the mass-spring-damper test case.** Displacements and velocities at five test scenarios as the results of the ODE integration (solid lines) and as predicted by the SVD-DeepONet (overlapping dotted lines) with structure as in Fig. 4.

with the PCA-NN approach of Bhattacharya *et al.* [14]. As stated by Kovachki *et al.*, both POD- and SVD-DeepONet “finite-dimensionalize the output in the span of PCA modes, bringing them (the DeepONets) closer to the method introduced in Bhattacharya *et al.* [14], but with a different finite-dimensionalization of the input space.” [10].

For operators that involve multiple states, as the mass-spring-damper system analyzed here, the SVD-DeepONet strategy to the surrogate learning can be pursued differently. In fact, instead of computing separate principal components and related principal directions for each of the snapshots matrices (e.g., for  $\mathbf{X}$  and  $\mathbf{V}$  in the test case under analysis), one can concatenate all or some of them and perform SVD on the resulting matrix,  $\mathbf{Z}$  (e.g.,  $\mathbf{Z} = [\mathbf{X}, \mathbf{V}]$ ). The dimensions of  $\mathbf{Z}$  are  $[N_t \times N_o N_S]$ , with  $N_o$  being the number of states sharing the same trunk. The shared components,  $\Phi_z$ , can then be fitted by a single FNN, and the columns of the  $\mathbf{A}_z$  matrix together with the related  $\mathbf{c}_z$  and  $\mathbf{d}_z$  vectors can be retrieved by  $N_o$  FNNs. Figures S7-S10 outline and report the application of this approach to the mass-spring-damper test case. It should be noted that the idea of sharing trunks between variables was one of the four strategies suggested by Lu *et al.* [53] for dealing with multiple outputs. However, in light of SVD-DeepONet, it must also be stressed that this technique has the potential of being significantly advantageous only if the dynamics of the state variables that share the trunk take place on comparable time/space scales and can be represented by similar principal components. Moreover, scenario-dependent scaling and centering become crucial if the state variables sharing the trunk have different units or span different ranges.

Finally, in view of what has been discussed above concerning its SVD-extension, we want to call attention to the benefits of the vanilla DeepONet as originally proposed in [12, 13]:

- In POD- and SVD-DeepONets, the eigenbasis of the empirical covariance operator needs to be computed *a priori* via POD/SVD. On the contrary, as pointed out by Lanthaler *et al.*: “(vanilla) DeepONets do not require any explicit knowledge of the covariance operator. In fact, our analysis shows that DeepONets implicitly and concurrently learn a suitable basis in output space along with an approximation of the projected operator” [54]. This generality, however, comes at the expense of predictive accuracy, as proven by the fact that the POD-DeepONet significantly outperformed the vanilla approach in the 16 benchmarks of [53]. Indeed, POD- and SVD-DeepONets produce orthonormal basis that are optimal in the  $\ell_2$  sense.
- Vanilla DeepONet autonomously learns a scenario-dependent scaling, as this variable is implicitly absorbed into the branches’  $p$  outputs as a function of the initial conditions (i.e.,  $b_i(x_0) = \tilde{b}_i(x_0) * d(x_0)$ ). On the contrary, because it uses a scalar bias [13, 34] that corresponds to a shift of the entire snapshots matrix based on its overall mean value, the vanilla architecture cannot learn a scenario-dependent centering. Instead, by adding a  $p + 1$ -th output to the branch net,  $c(x_0, v_0)$ , we enable the discovery of the proper scenario-dependent bias, which can further improve the generalization capabilities of the overall architecture.

- Although [32] and [53] recommended a hybrid physics-data training rather than a fully physics-informed approach, the vanilla DeepONet can theoretically learn a good approximation of the operator by simply relying on the residuals of the governing equations without using data points [38–40]. A physics-informed attribute can be given to the SVD-DeepONets by refining the sets of FNNs blocks learned independently from data through the training of the entire architecture using the governing equations in the loss.
- The vanilla DeepONet can work with sparse datasets. Most importantly, while it still requires a discretization of the branch input functions, it does not prerequisite any for the inputs to the trunks.
- Theoretically, the vanilla DeepONet can be trained on the fly (i.e., while more data is being acquired from sensors or additional simulations).

### 3.2. Test Case 2: A Shifting Hyperbolic Tangent Function

The second test case that we analyze is a toy problem constructed from the following ODE:

$$\frac{dx(t)}{dt} = a \operatorname{sech}^2 (bx_0 - t) \tag{10}$$

$$x(0) = x_0 \tag{11}$$

where  $t \in (0, 15)$ , the coefficients  $a$  and  $b$  are both set to 1, and the initial condition,  $x_0$ , is randomly selected from the interval  $(5, 10)$  based on Latin hypercube sampling. The ODE has the analytical solution

$$x(t) = a \tanh (t - bx_0) + a \tanh (bx_0) + x_0, \tag{12}$$

which corresponds to a hyperbolic tangent shifted in time and space as a function of the initial conditions  $x_0$ .

To construct a surrogate of the operator, we simulate 100 scenarios characterized by different initial conditions, and for each, we uniformly sample 500 time instants. We use the resulting 50,000 data points to train vanilla DeepONets with multiple numbers of neurons for trunk and branch output layers,  $p$ .

For clarity, in this test case we employ a vanilla DeepONet architecture as the starting point in order to motivate distinct improvements required to represent the underlying dynamics. In Fig. 6, the resulting predictions at five test scenarios are compared to the time-integrated solutions. In relation to the simplicity of the ODE, a relatively large network structure is required in the DeepONet (see Fig. S12), which also employs  $\tanh$  as activation functions consistently with the analytical solution. Notwithstanding, all the surrogates with  $p < 8$  (i.e., many modes) show noticeable inaccuracies.

In order to investigate this limitation on the expressive power of the vanilla DeepONet, we perform an analysis analogous to that carried out for the previous test case. We start by constructing a scenario-aggregated snapshots matrix,  $\mathbf{X}_{Raw}$ , that concatenates the 100 different scenarios as columns of dimensions  $[500 \times 1]$ , and, after having centered and auto-scaled, we decompose it via SVD. Two results are highlighted. Firstly, the energy contained in the singular values shows a slower decay (Fig. S13) than the one observed for the mass-spring-damper test case. This fact is also testified by the large encoding-decoding error generated by data matrix compressions that rely on less than eight modes, as reported in Fig. 7 for three training scenarios. From comparing this last figure with Fig. 6A, we can draw analogies between the dynamics predicted by the under-parameterized DeepONet and that reconstructed from the over-compressed data matrix. An insufficient number of neurons in the output layers of the trunk and branch nets acts as a bottleneck similar to scarce cumulative energy content in the retained singular values. Secondly, the complexity of the basis increases with the number of preserved singular values, as principal components corresponding to smaller singular values are characterized by higher frequencies (Fig. S14), and large oscillations also affect the related columns of the principal directions (Fig. S15) [75]. In analogy, this observation also has repercussions on the DeepONet’s performance. In order to fully exploit additional outputs, trunk and branch nets demand higher capacity as their regression tasks are complicated by oscillatory latent dynamics. This requirement may translate into deeper and/or wider trunks and branches, increasing the training efforts and the predictive computational costs.

The leading cause of slow singular value decay is the translational symmetry that characterizes this particular dynamical system. In fact, it is well known that SVD is highly contingent on the coordinate system adopted for representing the data. As a consequence, as stated by Brunton and Kutz [48], “the SVD rank explodes when objects in the columns translate, rotate, or scale, which severely limits its use for data that has not been heavily pre-processed”. Given the strong parallelisms between SVD and DeepONet discussed so far, it is not surprising to find the latter is also affected by similar limitations in processing shifts, rotations and scaling. Here we adopt a simple but effective modification to DeepONet’s original structure that, if viewed under the SVD paradigm, acts as an artificial intelligence (AI)-operated data alignment aimed at symmetry removal. The proposed improvement allows the automatic discovery of a moving frame of reference with respect to which the multiple scenarios result as overlapping as possible, and they then can be efficiently compressed to a lower number of modes. The frame’s motion is uncovered by an additional DeepONet block, which we call pre-transformation network (pre-net). As sketched in Fig. 8 for a generic PDE with independent variables  $\mathbf{y}$ , this new component takes the same inputs as the branch nets,  $\mathbf{u}$ , and it outputs a scaling factor,  $\bar{s}$ , a vector of angles,

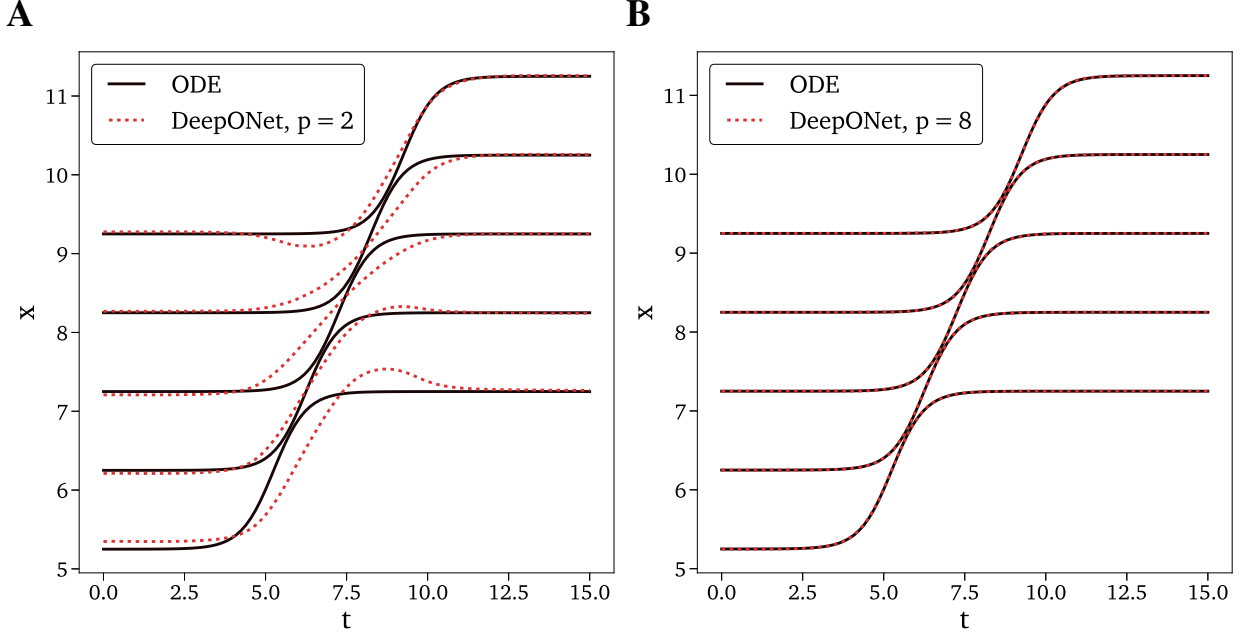


Figure 6: **Vanilla DeepONet applied to the shifting hyperbolic function test case.**  $x$  at five test scenarios as the results of the ODE integration (solid black lines) and as predicted by vanilla DeepONets (red dotted lines) with trunk and branch’s output layers composed of two (A) and eight (B) neurons. See Fig. S12 for details on the vanilla DeepONet’s structure.

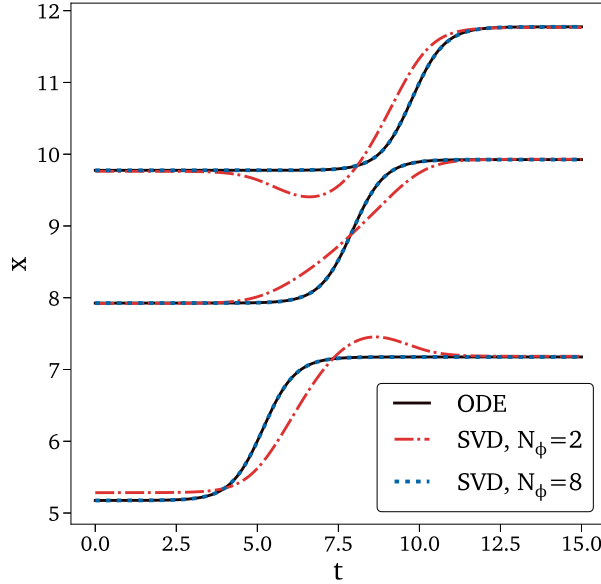


Figure 7: **Training scenarios reconstructed via SVD.** Three of the training scenarios for the shifting hyperbolic function from the ODE integration (black solid lines) and after being encoded-decoded based on SVD’s first two (red dashed lines) and first eight (blue dotted lines) singular values.

$\bar{\theta}$ , and a vector of shifting coefficients,  $\bar{y}$ . In a subsequent transformation layer, a rotation matrix  $\bar{\Theta}$  composed of sines and cosines is constructed from  $\bar{\theta}$ , and the independent variables (i.e., the input of vanilla DeepONet’s trunk) are rotated, scaled, and shifted before they enter the trunk net. We call the vanilla architecture augmented by the pre-net and one additional branch output a “flexible DeepONet” (flexDeepONet). While this paper was being written, a very similar approach, called Shift-DeepONet, has been independently proposed by Hadorn [49] to improve the performance of

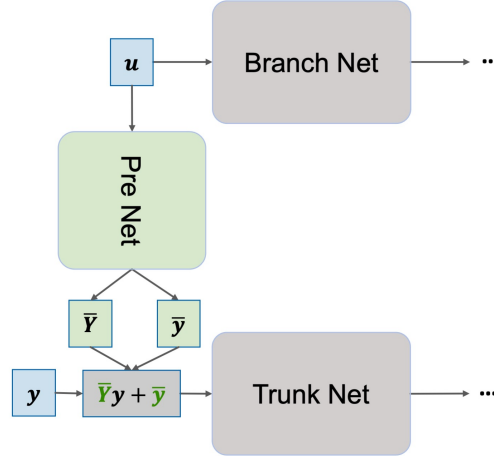


Figure 8: **DeepONet’s pre-transformation network (pre-net), as proposed in the present work.** The block implements a transformation that automatically discovers a moving frame of reference with respect to which the multiple scenarios are efficiently compressible in fewer modes. In this way, the pre-net extends DeepONet’s flexibility with learning operators characterized by dynamics that shift, rotate, and/or scale. Note: in the transformation layer subsequent to the pre-net, a rotation matrix  $\Theta$  composed of sines and cosines is constructed from  $\bar{\theta}$ .

DeepONet applied to problems involving discontinuities. However, there are three main differences between the two techniques: i) flexDeepONet allows for the realignment of data affected by rotations, as it includes the matrix  $\Theta$ . In this sense, Shift-DeepONet’s pre-processing block is a particular instance of a flexDeepONet’s pre-net characterized by diagonal  $\Theta$ . ii) FlexDeepONet’s pre-net has  $N_y$  outputs, where  $N_y$  represents the dimensionality of  $\mathbf{y}$ . In contrast, Shift-DeepONet’s pre-processing block produces  $N_y \times p$  outputs, which are all used as trunk’s inputs. From this perspective, Shift-DeepONet has more expressivity than flexDeepONet, as each of the trunk’s modes is constructed as a non-linear combination of the  $N_y \times p$  pre-processing block’s outputs. Nevertheless, such versatility might come at the expense of interpretability and generalization in low-data regimes. iii) Shift-DeepONet’s branch produces  $p$  outputs, while FlexDeepONet’s branch has  $p + 1$  outputs, as motivated in the following discussion. For reasons of completeness, it should be mentioned that the idea of linking  $\mathbf{u}$  and  $\mathbf{y}$  before DeepONet’s inner product layer was already proposed by Wang *et al.* [80]. However, the trunk-branch connections those authors devised were multiple (i.e., the outputs of each branch’s hidden layers entered the trunk) and bidirectional (i.e., the outputs of each trunk’s hidden layers also entered the branch). Their improvement, in fact, was consistent with different reasoning. As Wang *et al.* mentioned, “(in the vanilla architecture), the final information fusion may be inefficient if the DeepONet input signals fail to propagate through a deep branch network or trunk network at initialization, leading to an ineffective training process and poor model performance” [80].

Recently, Oommen *et al.* proposed to learn complex dynamics via DeepONet in a latent and low-dimensional space through the employment of autoencoders [33]. In their application, they reduced the dimensionality of images with resolution  $[128 \times 128]$  into coded variables with dimensions of the order  $\mathcal{O}(10 - 100)$ . The dynamics represented in the latter quantities resulted in being less affected by high gradients and more easily representable via DeepONets. While they both benefit from transformations into latent spaces of independent variables that simplify the surrogation by disentangling the dynamics, the autoencoded-DeepONet and the flexDeepONet approaches have different primary focuses. Indeed, while an autoencoder is an extremely powerful addition in applications that require dimensionality reduction, the so performed transformations to the latent spaces lack interpretability and do not necessarily guarantee the separation of the rigid components of the motion. However, we believe that these aspects can be improved by introducing in the autoencoded-DeepONets paradigm some of the concepts from [81]. As stated in their work, Mojjani and Balajewicz trained “a diffeomorphic spatio-temporal grid, that registers the output sequence of the PDEs on a non-uniform parameter/time-varying grid, such that the Kolmogorov n-width of the mapped data on the learned grid is minimized.” In addition, in autoencoded-DeepONets the detection of the effective (reduced-dimensional) reference frame precedes the DeepONet, as the training of the autoencoder takes place before the training of the surrogate. This fact might represent a limitation in streaming machine learning applications. In contrast, flexDeepONet discovers the new reference frame while learning the dynamics. We also acknowledge that, almost simultaneously with the work of Oommen *et al.*, the idea of coupling DeepONets and autoencoders was suggested by Zhang *et al.* [82] for surrogating

stochastic differential equations (SDE).

Fig. 9 represents the flexDeepONet architecture for the shifting hyperbolic function test case, in which the generic pre-net is simplified to a shifting block with a single output. The depths and widths of trunk and branch nets are

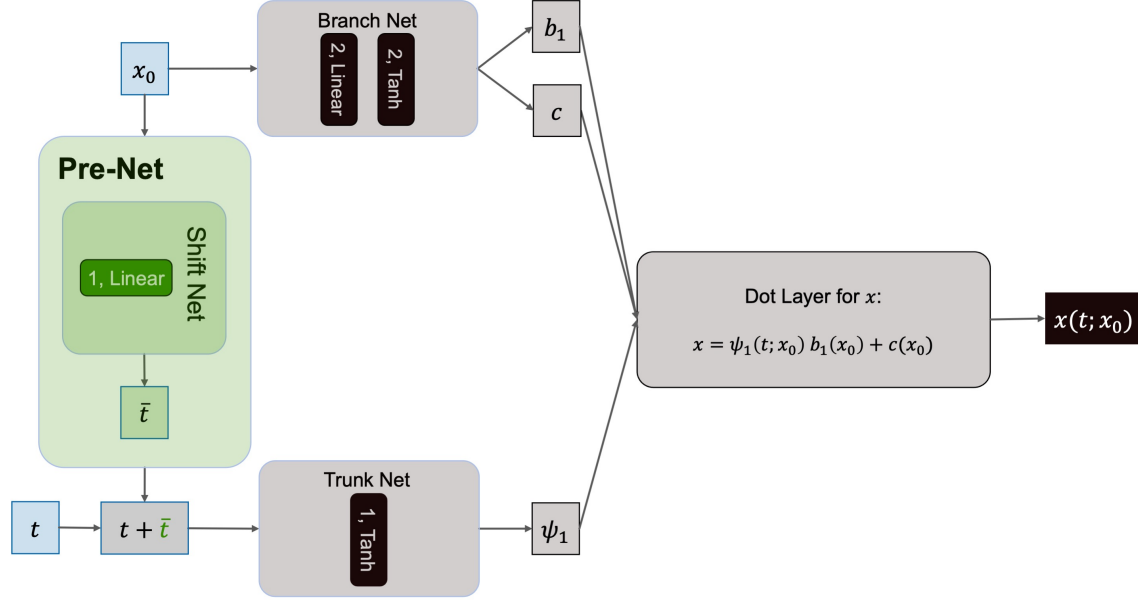


Figure 9: **FlexDeepONet architecture for the shifting hyperbolic function test case.** A pre-net composed of a shifting FNN is introduced to guarantee the alignment of the different scenarios. An additional neuron is added to the output layer of the branch net to permit scenario-specific centering.

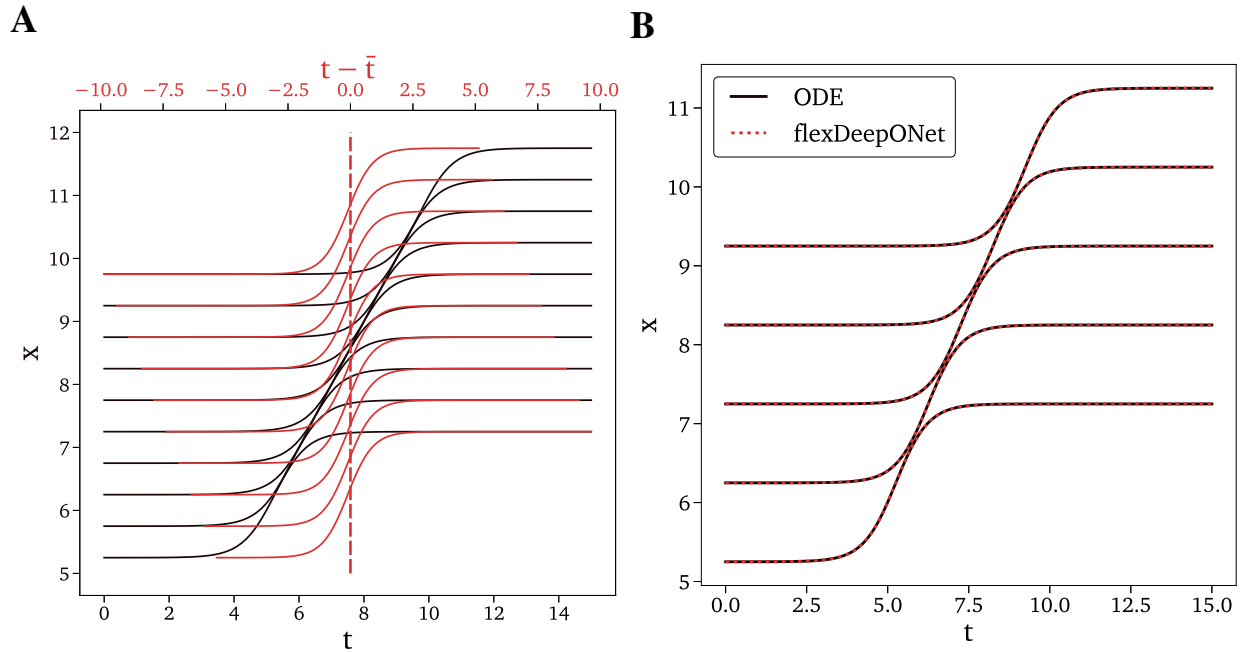


Figure 10: **FlexDeepONet applied to the shifting hyperbolic function test case.** (A): Time-integrated  $x$  for the test scenarios as a function of the simulation time (black lines) and the simulation time corrected by the shift net (red lines). (B):  $x$  at five test scenarios as the results of the ODE integration (solid black lines) and as predicted by flexDeepONet (red dotted lines) with structure as in Fig. 9.



extremely decreased compared to the vanilla DeepONet employed above, and, in this new configuration, the trunk net has only one output. Two outputs are instead used for the branch net, one of which represents the centering coefficient,  $c$ , assumed to be a function of the initial conditions to improve the generalization capabilities of the architecture. As explained while discussing the first test case, the scaling  $d$  is implicitly learned by the vanilla DeepONet as part of the  $b_i$  outputs, and it is not considered here to avoid redundancies. Fig. 10A reports the evolution of  $x$  as a function of the original system of coordinates,  $t$ , and of the moving reference frame (i.e.,  $t$  translated by the output of the shift net,  $\bar{t}$ ). The figure attests that the new block is capable of aligning the different scenarios. Because of this improvement, the flexDeepONet is efficient in projecting the dynamics on a one-dimensional basis (i.e.,  $p = 1$ ), and it can predict the time evolution of  $x$  with excellent accuracy (Fig. 10B) despite the remarkable fact that the number of trainable parameters is reduced by 99.5% (i.e., from 4,880 to 22).

Finally, after having discussed the application of flexDeepONet to the test case under analysis, it is important to mention that the SVD's deficiency in processing translated, rotated, and shifted data is also passed on to the derived techniques, as for POD-based methods [83]. For instance, researchers have extensively worked on developing suitable remedies for the challenges resulting from the symmetries in transport-dominated flows [50, 52, 84–88]. Some of these techniques share strong similarities with the pre-transformation network presented in this work. In particular, it should be mentioned the analogy with the Neural Network shifted-POD (NNsPOD) recently proposed by Papapicco *et al.* [52], which extends the work of Reiss *et al.* [50, 51] on constructing continuous shift operators for POD by automatizing the detection of transport velocities.

### 3.3. Test Case 3: Combustion Chemistry in an Isobaric Reactor

The third test case focuses on a chemical dynamical system of practical relevance, involving the analysis of combustion chemistry dynamics taking place in a high-temperature zero-dimensional isobaric reactor. The chemical system is initially assumed to contain only  $H_2$  and air (assumed to be composed of  $N_2$  and  $O_2$  with respective mole fractions 80% and 20%) at initial temperature  $T_0$  and pressure  $P_0$ , and with relative mole fractions specified by an initial equivalence ratio,  $ER_0$ , defined as [89]:

$$ER_0 = \frac{X_{H_2}/X_{Air}}{(X_{H_2}/X_{Air})_{st}}, \quad (13)$$

where  $X_i$  represents the mole fraction of the  $i$ -th (macro-)species, and the  $st$  suffix identifies the stoichiometric value. The system is then evolved in time, and the overall dynamics of the temperature and the  $N_s$  species are described by the following ODE:

$$\begin{cases} \frac{d\rho y_i}{dt} = \dot{\omega}_i \\ \rho C_p \frac{dT}{dt} = \dot{\omega}'_T \end{cases} \quad (14)$$

where  $\rho$  identifies the mixture density,  $y_i$  denotes the mass fraction of the  $i$ -th species with  $i = 1, \dots, N_s$ , and  $C_p = C_p(T)$  represents the isobaric specific heat capacity. The rate of species production/depletion,  $\dot{\omega}_i$  is defined as:

$$\dot{\omega}_i = \sum_{j=1}^{N_s} \dot{\omega}_{i,j}(y_i, y_j), \quad (15)$$

while the heat release,  $\dot{\omega}'_T$ , is given by:

$$\dot{\omega}'_T = - \sum_{i=1}^{N_s} h_i \dot{\omega}_i(y_i, y_j) \quad (16)$$

with  $h_i$  being the partial specific enthalpies. For details on the analytical dependencies of the reaction rates,  $\dot{\omega}_{i,j}(y_i, y_j)$  on  $y_i$  and  $y_j$ , the reader should refer to [89]. In this work, we employ a sub-component of the GRI-Mech 3.0 reaction scheme [90] to define the  $H_2$  chemistry. The full mechanism would include 325 reactions and 53 species based on the five elements O, H, C, N, and Ar. However, since none of the argon- and carbon-containing chemistry is active, the effective number of reactions produced by the combustion of hydrogen with air is significantly lower, and only eighteen species are considered. This brings to 19 the total number of thermodynamic variables,  $\boldsymbol{x}$ , for the problem under analysis (i.e.,  $\boldsymbol{x} = \{T, \boldsymbol{y}\}$ ). The system of equations is finally closed by the ideal gas law:

$$P = \rho \frac{R}{M} T, \quad (17)$$

where  $R$  and  $M$  respectively represent the ideal gas constant and the mixture molecular weight.

By relying on Cantera [91], an open-source suite of tools for problems involving chemical kinetics, thermodynamics, and transport processes, we generate 500 simulations for as many sets of initial conditions. Each of those is obtained by

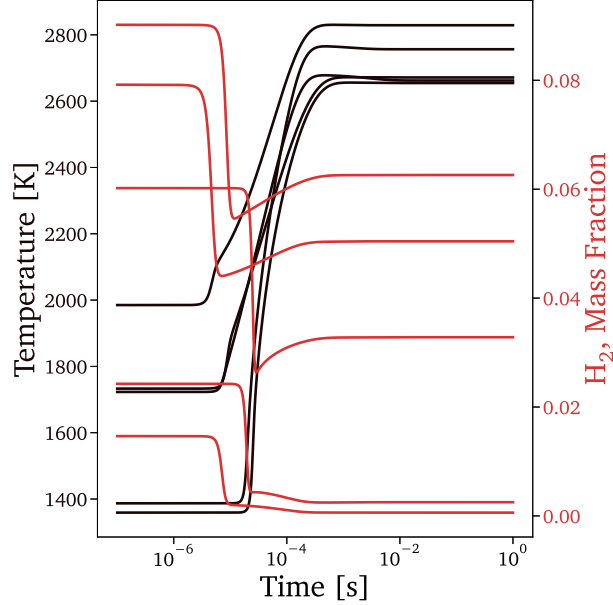


Figure 11: **Training data for the combustion chemistry test case.** Five examples of training scenarios showing the evolution of temperature and  $H_2$  mass fraction. See Fig. S17B for the mass fractions of additional species.

fixing the reactor pressure at  $P_0 = 1$  [atm] and by selecting initial temperatures and initial residence times through Latin hypercube sampling of the space  $(T_0, ER_0) \in (1000$  [K],  $2000$  [K])  $\times$   $(0.5, 4)$ . For each simulation, the solutions are collected at 500 time instants, which altogether form a set of 250,000 data points for the ODE solution  $x : [(T_0, \mathbf{y}_0), t] \mapsto (T, \mathbf{y})$ . Temperature and  $H_2$  mass fractions from five training scenarios are shown in Figs. 11. Given the different order of magnitudes that characterize the thermodynamic variables, feature scaling based on min-max normalization is applied to the data before training all the operator surrogates for this physical system. In analogy with the previous test case and because of what will be discussed later, it is important to highlight that (logarithmic) time shifts are noticeable components of the overall transformations affecting the evolution profiles as functions of the scenarios [92, 93]. It should also be noted that shifts in a logarithmic scale correspond to stretches in a linear scale.

With the resulting data points, we train two vanilla DeepONets that have one branch and one trunk for each of the  $x_j$  thermodynamic variables, with  $j = 1, \dots, 19$ . These blocks are characterized by six hidden layers and  $p$  outputs each, with  $p = 20$  for the first DeepONet and  $p = 32$  for the second. The structures of the two surrogates are shown in Fig. 12, and they respectively contain 297,160 and 738,112 trainable parameters. Predictions on test scenarios are presented in Figs. S19 and S20, and they show significant oscillations in the time instants that immediately preceded and succeed sharp gradients, especially for  $T$  and  $y_{H_2}$ .

In light of what was observed for the previous *tanh* test case, we proceed by investigating the results from the SVD perspective. As before, we create a scenario-aggregated snapshots matrix with dimensions  $[500 \times 500]$  for each of the thermodynamic variables. We then center each of its columns, normalize them based on their standard deviations, and perform SVD. Two interesting results emerge from this procedure. Firstly, in order to preserve 95% of the matrices' cumulative energy content, the number of singular values that must be retained ranges between 5 and 32, depending on the thermodynamic variable under analysis, and at least 20 to 60 must be kept to reach 99% (Fig. S21). The consequences of retaining only 20 and 32 singular values are respectively shown in Fig. S22 and Fig. S23 in terms of SVD's encoding-decoding inaccuracies. After being projected to the reduced basis, the reconstruction of the dynamics results in artificial oscillations similar to those that characterize the vanilla DeepONet's predictions. Secondly, in analogy with what has been observed for the shifting hyperbolic tangent test case, lower singular values are associated with principal components and directions characterized by higher frequencies. As some examples, Fig. 13 shows the principal components corresponding to the 32nd and 64th singular values of  $H_2$ . This should be taken into account while selecting the number of scenarios and time instants to be simulated for generating DeepONet's training data to avoid aliasing-related issues.

Based on these two findings, we deduce that an increase in the number of trunks' outputs reduces DeepONet's approximation error but also complicates trunks' and branches' fitting tasks. As a consequence, the sub-blocks regression errors would rise unless their network expressivities are significantly improved. To summarize, the following aspects should be considered altogether:

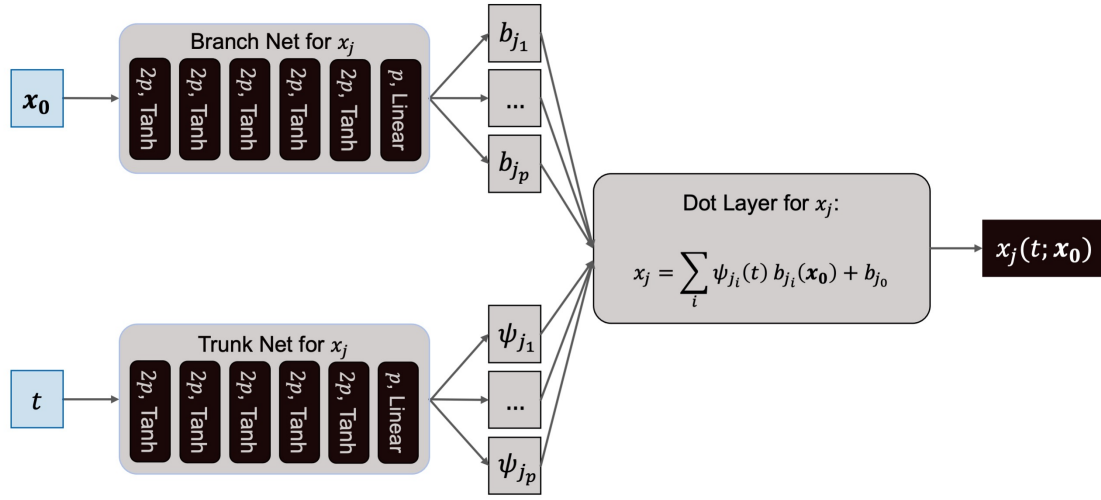


Figure 12: **Architecture of the vanilla DeepONet for one of the 19 thermodynamic variables.**  $j = 1, \dots, 19$ , and each thermodynamic variable has its own trunk and branch nets. We study two separate vanilla DeepONets, respectively characterized by  $p = 20$  and  $p = 32$ .

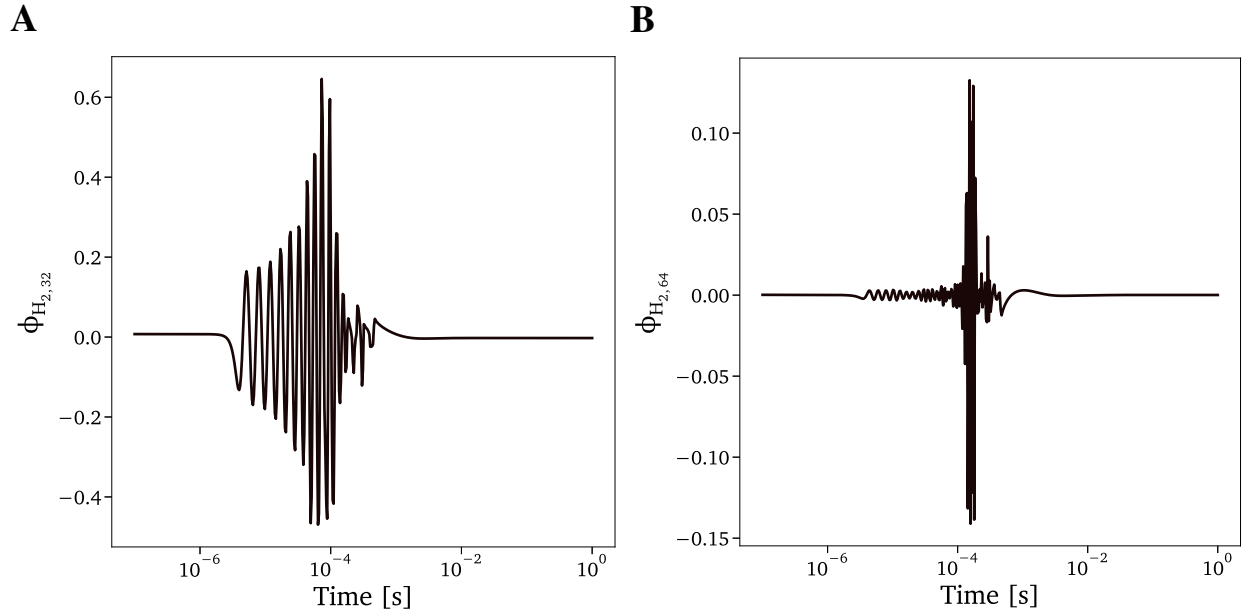


Figure 13: **Principal components of the data matrix constructed with the  $H_2$  scenarios.** Principal components associated with the thirty second (A) and sixty fourth (B) singular values.

- The vanilla DeepONet autonomously performs the projection by means of the dot-layers;
- In the case of an  $\ell_2$ -optimal projection, the information content retained by only 32 singular values is insufficient for retrieving with high accuracy some of the evolving thermodynamic variables;
- In the case of an  $\ell_2$ -optimal projection, some of the trunk and branch nets are asked to reproduce highly oscillatory modes.

As discussed concerning the previous test case, by representing the dynamics on a coordinate system that moves as a function of the initial conditions, it is possible to take into account the geometrical similarities between the evolution profiles for different scenarios and improve the projection to the reduced basis. Following this intuition, Lemke *et al.* [92] developed a reduced-order model for a 0-D isobaric reactor. Their test case was similar to the one we are proposing, but i) had methane as the fuel, ii) the initial mass fractions were not changed while varying scenarios, and iii) the initial temperatures were selected from a smaller range (i.e., 1020 - 1080 [K]). Lemke *et al.*'s strategy for constructing a data-driven surrogate capable of predicting the reactor's thermodynamic state for unseen initial conditions relied on the following steps: i) time-shifting the scenarios so that their maximum temperature gradients matched in time, ii) performing SVD, and iii) interpolating the coefficients of the projection matrix. As their data alignment allowed the SVD to improve the singular values' rate of decay, an autonomously-discovered shifting reference frame would empower the DeepONet to project the operator dynamics on a lower-dimensional basis. In this sense, the flexDeepONet architecture has the capability of transforming the Lemke *et al.*'s approach to a fully AI-operated surrogate construction. We now build a flexDeepONet for the present test case. Compared to the vanilla architecture,

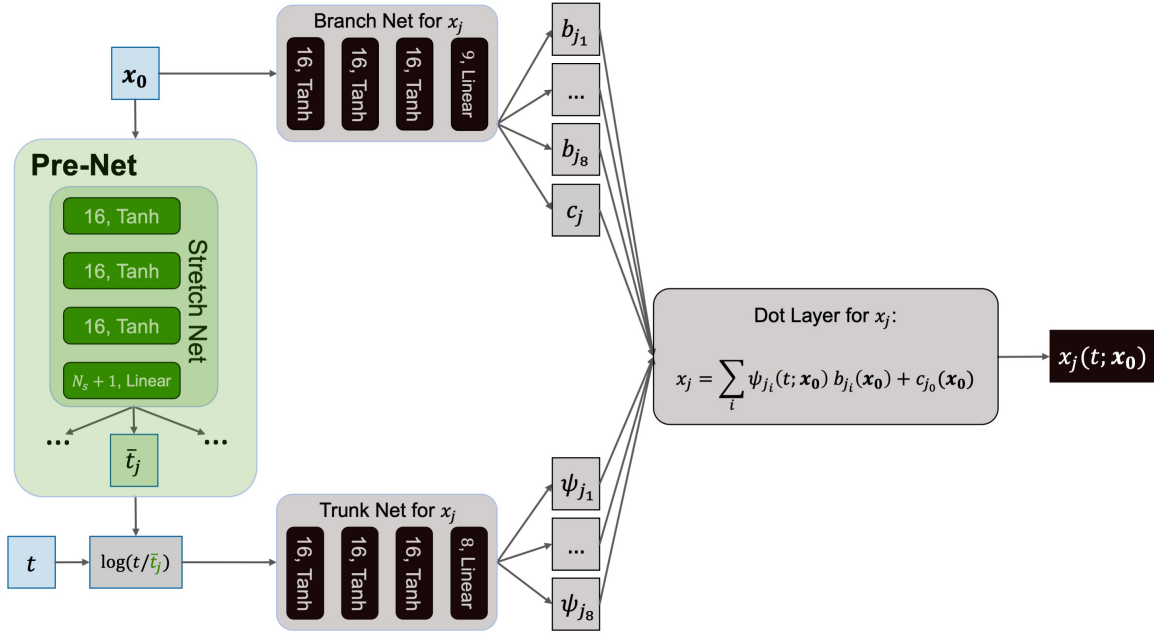


Figure 14: **FlexDeepONet architecture for the  $j$ -th thermodynamic state variable of the combustion chemistry test case.** The DeepONet is composed of  $N_s + 1$  trunks,  $N_s + 1$  branches, and a single pre-net made of one stretching FNN, where  $N_s = 18$  represents the number of chemical species. The stretching block is introduced to guarantee the alignment of the different scenarios, and it outputs  $N_s + 1$  factors, one for each of the trunk nets. An additional neuron is added to the output layer of each branch net to permit scenario-specific centering.

the surrogate prepends a single pre-transformation network. This block is shared by all the thermodynamic variables, and it outputs one quantity for each of them,  $\bar{t}_j$ , that can be either seen as a stretching factor operating in a linear scale or as a shifting bias in a logarithmic scale. Additionally, we add one output to each branch net to learn scenario-dependent centering. These two simple improvements permit a decrease in the number of DeepONet's projection basis (i.e.,  $p$ ). As less expressivity is required from the trunks and branches, the depths and widths of these nets can be significantly reduced. The flexDeepONet structure used for this test case is reported in Fig. 14. Overall, the number of trainable parameters is lowered to 34,038. Fig. 15A shows the values of the scaling factors discovered by the stretch net for some thermodynamic variables as functions of the initial temperature. Thanks to these quantities, the scenario-dependent dynamics are well aligned with respect to the scaled system of coordinates, as testified by Fig. 15B. The effectiveness of

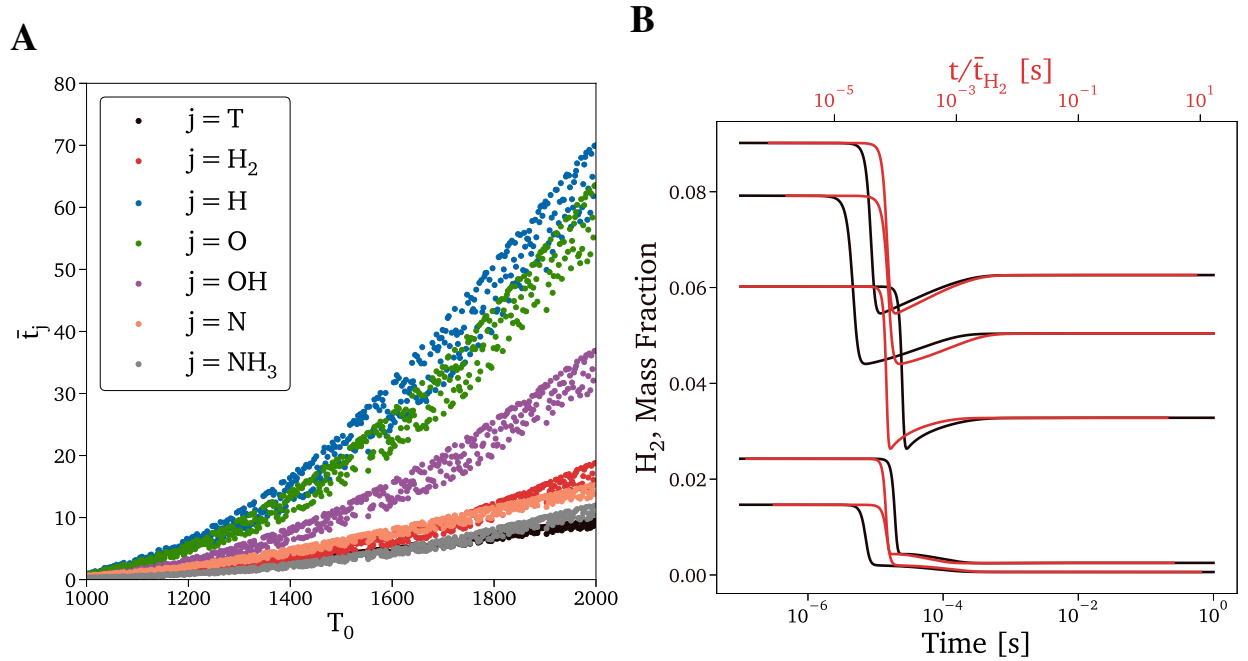


Figure 15: **Contributions of the shift net to the scenario alignment.** (A): Some outputs of the stretch net, corresponding to the scaling factors of some thermodynamic states. The predictions are plotted for all the training scenario as function of their initial temperatures. (B): Time-integrated  $H_2$  mass fractions for some of the test scenarios as functions of the simulation time (black lines) and of the simulation time corrected by the stretch net (red lines). See Fig. S25 for additional mass fractions, and Fig. 14 for details about the flexDeepONet’s structure.

DeepONet’s projections increases, and the oscillations in the predictions are removed (Fig. 16). Despite the 89%/95% reduction in the number of trainable parameters compared to the vanilla architectures with  $p = 20/32$ , flexDeepONet appreciably enhances the accuracy in predicting temperature and mass fractions, as reported in Table S1. It should be noted that the few species that are not improved by the flexDeepONet are also the ones that are not remarkably affected by shifts in their dynamics and that can effectively be compressed to a small number of modes.

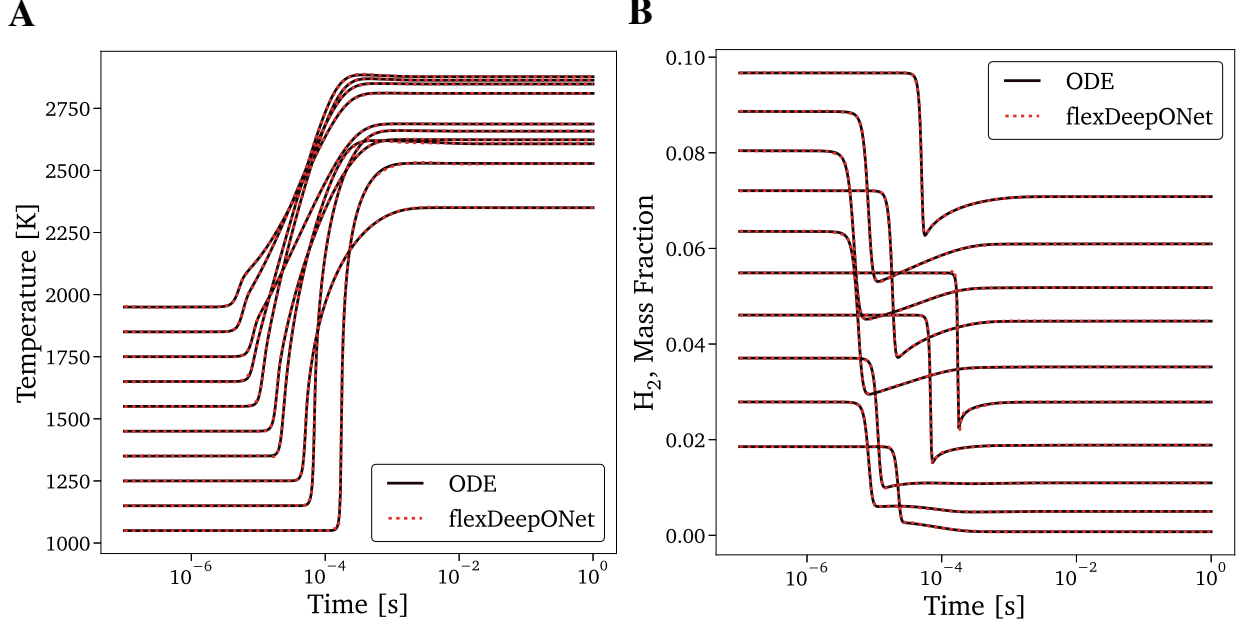


Figure 16: **FlexDeepONet predictions of the thermodynamic variables.** Temperature (A) and  $H_2$  mass fraction (B) for ten test scenarios as the results of the ODE integration (solid black lines) and as predicted by flexDeepONet (red dotted lines) with structure as in Fig. 14. See Fig. S24 for additional mass fractions.

#### 4. Test Case 4: POD and DeepONet Analysis of a Rotating-Translating-Stretching Rigid Body

The three test cases above showed how SVD perspectives on the DeepONet can improve the technique’s flexibility and interpretability. However, we believe that the links between the two methodologies are bidirectional and that some of DeepONet’s peculiarities can significantly facilitate and extend applications of SVD-based methods, such as PCA, DMD, and POD. This sub-section briefly proposes an example of such a promising research direction. This last test case’s objective is to reproduce 2D rigid body dynamics, the rotation, translation, and stretch of which are non-linear functions of time (a cosine, a spiral, and a sine, respectively). The equations used for producing the test case can be found in Sec. S4 of the supplementary material, and some time-snapshots of the dynamics are reported in Fig. 17. In the following, we assume that we have no knowledge of the PDE that governs the motion and are forced to reconstruct the dynamics fully from the data. At this point, it is important to highlight the conceptual differences between this problem and the three test cases previously analyzed. In the examples above, we studied the full operators for a wide range of scenarios. Here, instead, we are interested in a particular instance of the dynamics based on a single (i.e., predefined) initial condition. As a consequence, the analysis of the problem from an SVD-based perspective involves the construction of a time-aggregated snapshot matrix consistently with the POD methodology [83]. Such a matrix is generated by selecting 200 time instants in the dynamics between  $t = 0$  [s] and  $t = 10$  [s] and by populating the

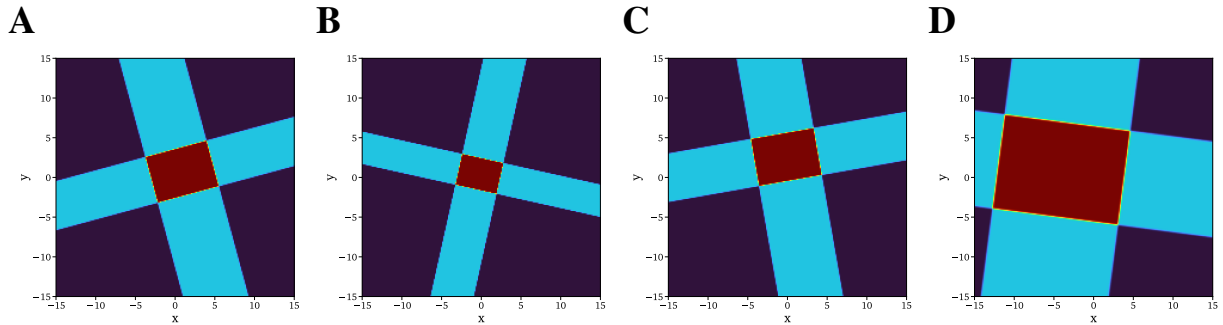


Figure 17: **Four time snapshots for the dynamics of the rotating-translating-stretching rigid body.** The snapshots are produced at  $t = \{0, 3.33, 6.67, 10\}$  [s]. See Fig. S26 for additional time instants.

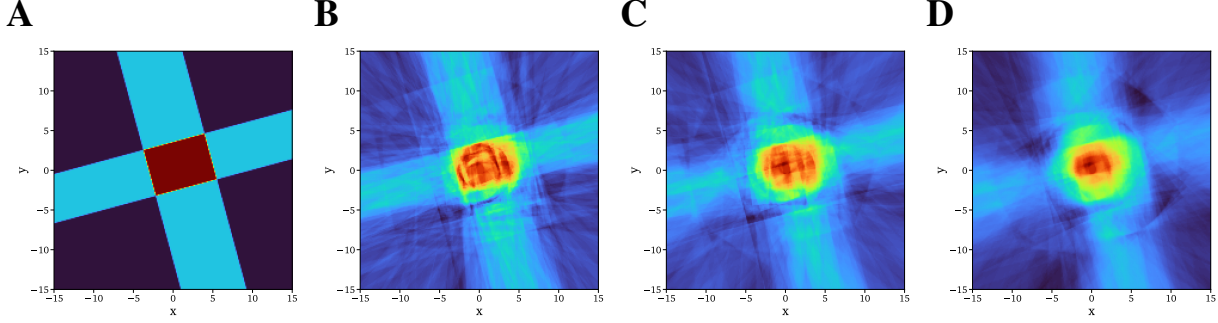


Figure 18: **Time snapshot decomposed and reconstructed via POD.** Time snapshot at  $t = 0$  [s] as generated by the original equations (first column from the left) and after being encoded-decoded based on POD’s first 128, 64, and 32 modes (second, third, and fourth columns, respectively). See Fig. S28 for additional encoded-decoded time snapshots.

columns with the solution corresponding to a  $[200 \times 200]$   $x - y$  grid at each specific time, appropriately reshaped to a  $[40,000 \times 1]$  vector. Due to the motion being dominated by symmetries, the SVD fails to discover an accurate low-rank decomposition, and the application of the classical POD method requires more than 150 modes to recover 95% of the dynamics’ cumulative energy (Fig. S27). As demonstrated in Fig. 18, the encoding-decoding errors generated by the compression of the time-aggregated snapshots matrix into the dominant POD modes are visible even when 128 singular solutions are retained.

With the aim of learning the body’s dynamics, we test two separate DeepONet architectures. In contrast to the three cases above, the  $t$  (i.e., time) variable is used as the branch’s input, while the  $x$  and  $y$  space coordinates are passed to the trunk. This unconventional application of the DeepONet architecture should be emphasized: instead of employing it as a neural operator, it is here used for the automatic generation of a reduced-order surrogate of the single scenario. Moreover, this type of approach should not be confused with the POD-DeepONet technique by Lu *et al.* [53], still applied to the neural operator construction and in which the trunk net is replaced by the modes of the scenario-aggregated data matrix. In order to further demonstrate DeepONet’s capabilities, we train the surrogates with a data set that has two remarkable differences from the one employed in the POD analysis above:

- Instead of using the 8,000,000 data points distributed in two hundred equally-spaced time snapshots with the same grid of  $[200 \times 200]$   $x$  and  $y$  nodes, we randomly sample 1,000,000 data points in the  $(x, y; t)$  space. 80% of them are used for training, and the remaining 20% for validation.
- Rather than generating training data in a  $(x, y) \in (-15, 15) \times (-15, 15)$  domain, we restrict the sampling of the spatial coordinates to the  $(x, y) \in (-10, 10) \times (-10, 10)$  subset region. Time, instead, is sampled over the full  $t \in (0, 10)$  domain.

We firstly train a relatively large vanilla DeepONet, in which branch and trunk nets rely on 128 outputs and are composed of six hidden layers and 128 neurons each, for a total of 165,761 parameters. Consistent with the extremely slow decay of the singular values and with what we observed in the previous test cases, the vanilla DeepONet is

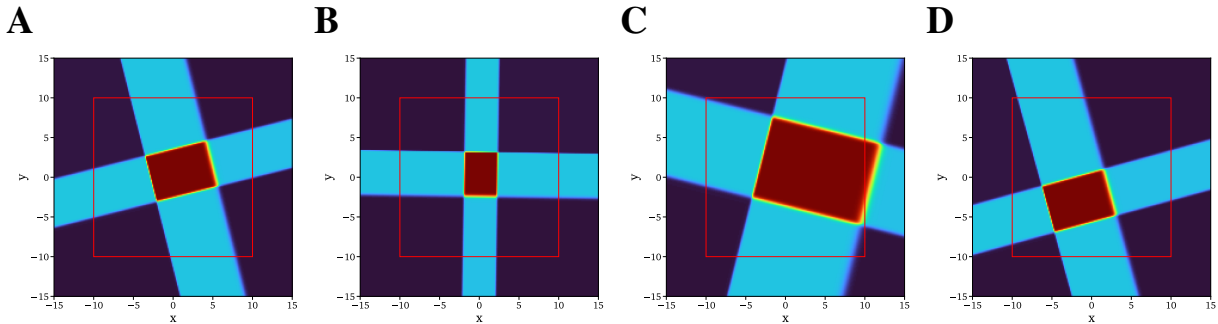


Figure 19: **FlexDeepONet predictions of the rigid body’s dynamics.** The snapshots are produced at  $t = \{0, 3.33, 6.67, 10\}$  [s]. Note: FlexDeepONet’s training relied only on data randomly-selected inside the  $x - y$  domain represented by the red squares. Predictions outside the red squares are extrapolations. See Fig. S31 for FlexDeepONet’s structure and Fig. S32 for additional time snapshots.

noticeably inaccurate, as reported in the supplementary material at sixteen testing times. The surrogate is tested for predictions at locations contained in the  $(x, y) \in (-10, 10) \times (-10, 10)$  training domain but also for extrapolations outside the square. The body’s shape is highly distorted by the ineffective compression to the 128 bases and by the difficulties of the sub-nets in retrieving the modes and the related coefficients. The erroneous patterns are even accentuated outside the training domain, as expected.

We then apply the flexDeepONet to the same regression task. Given the different types of symmetries involved in the dynamics, the pre-net employed in this test case outputs four different variables: a rotation angle,  $\bar{\theta}$ , a stretching factor,  $\bar{s}$ , and two shifting parameters,  $\bar{x}$  and  $\bar{y}$ . These four quantities are here autonomously regressed from data through three separate blocks (i.e., rotation net, stretch net, and shift net, as reported in Fig. S31), as an alternative to using a single FNN. The coefficients are then passed to a transformation layer, which combines them with the spatial coordinates via a scaled rotation matrix, based on  $\bar{s}$  and  $\bar{\theta}$ , and a shifting vector, formed as  $[\bar{x}, \bar{y}]^T$ . The two quantities outputted by this transformation layer are finally passed to the trunk net as inputs. The flexDeepONet’s branch and trunk nets are significantly smaller than the vanilla’s correspondent sub-nets, as we impose  $p = 1$ . In this way, the trunk net is asked to retrieve only one mode from the data. However, because this basis is defined in the moving reference frame discovered by the pre-net, the single mode that the trunk sees and aims to reconstruct is the full rigid body itself, rather than one of the dynamics’ low-energy-content components. This key aspect has vital consequences on the surrogate’s generalizing capabilities. As shown in Fig 19, flexDeepONet remarkably improves the predictions/extrapolations of the rigid body’s dynamics for  $x, y$  coordinates both inside and outside the training window at unseen time instants. Furthermore, these advancements are achieved by relying on only 1,921 trainable parameters, which corresponds to a 98.8% reduction compared to the vanilla architecture.

## 5. Summary and Discussion

Recent in-depth analysis and applications to real-world problems in many fields have demonstrated the unprecedented capabilities of DeepONet as a neural operator surrogate approach. The effectiveness and efficiency of the technique are in part attributable to the projection component of the architecture, which is implemented as dot-product layers. Some unique characteristics make DeepONet significantly more flexible than the classical fully data-driven projection-based methods, as it overcomes many limitations of the latter. For instance, it allows the construction of physics-informed surrogates by also relying on sparse and multifidelity datasets. In this paper, we have shown that there are also shortcomings that DeepONet inherits from the projection-based attribute, and we propose suitable remedies that can extend its flexibility.

We initially applied DeepONet to learn the operators underlying three dynamical systems, all described by relatively simple ODEs. The first test case was based on a mass-spring-damper model and allowed us to propose a novel approach to DeepONet training: SVD-DeepONet. While the applicability of this technique to real-world problems might be limited to cases in which the data is available on scenario-spatio-temporal grids (i.e., cases in which the data allows to perform SVD), it has the instructive purpose of drawing parallels between data decompositions methods and the DeepONet architecture. In fact, we showed that its trunk and branch nets regress the modes and the related coefficients discovered by the projection. Moreover, if SVD can be performed on subsets of DeepONet’s training data, the SVD-approach can be employed in an exploratory phase, in which the number of trunk outputs and the capacity of the subnets (e.g., depths and widths) need to be decided.

From the analogy with projection-based methods, we also developed a shared-trunk formulation. This modification can be seen as a dimensionality reduction of the full DeepONet architecture, as multiple state variables share the same trunk net under the assumption of underlying similarities in their modes. In future work, we will analyze other strategies for combining dimensionality reduction techniques to multi-output DeepONets, such as projecting the state variables into lower-dimensional spaces or grouping them into macro-variables [30]. These approaches will include PCA, non-linear manifold learning, and coarse-graining. Furthermore, in light of the connections between low-rank decompositions and DeepONet, an additional research direction is the analysis of multi-input DeepONets [94, 95] under the perspective of tensor decomposition [96].

The second and third test cases revealed DeepONet’s inefficiencies in surrogating dynamics characterized by symmetries. Scenario-aggregated SVDs need many modes of increasing complexity for accurately projecting operators affected by translations, rotations, and/or scalings. Similarly, the vanilla DeepONet architecture requires several trunk outputs and remarkably expressive subnets for the same applications. This significantly increases computational costs and challenges of both the training and prediction phases. Therefore, we employed a simple but effective modification to the original structure. We added a pre-transformation block that acted as an artificial intelligence (AI)-operated data alignment aimed at symmetry removal. This sub-net automatically discovered a moving frame of reference with respect to which the multiple scenarios were efficiently compressible in fewer modes. We also included an additional branch output to learn the underlying scenario-based centering. The resulting architecture, called flexDeepONet, drastically reduced the size of the surrogate without compromising its accuracy. In particular, flexDeepONet’s trainable parameters for



emulating the combustion chemistry test case (19 state variables spanning many orders of magnitudes) were about 95% less than those of vanilla DeepONets characterized by larger generalization errors. Thanks to the resulting speed-ups, we believe that flexDeepOnet can benefit the surrogation of operators with latent symmetries, particularly in real-time applications and digital twins.

The present comparative analysis of DeepONet and SVD-based methodologies is far from being exhaustive. More work needs to be done in constructing rigorous mathematical definitions of the analogies mentioned above. Together with the extension to PDEs, this will be a core focus of future work. Overall, this paper specifically aims to interpret the DeepONet structure and suggest a promising research direction. In light of these parallelisms, multiple concepts behind refined SVD-based methods can be adapted and introduced to DeepONet. For example, underlying ideas can be recovered from robust PCA to work with corrupted data and probabilistic PCA to represent the uncertainties caused by limited information.

We also believe that the contributions between DeepONet and SVD-based methods can be mutual, and the flexibility of the former can extend some of the PCA, DMD, and POD applications. For this purpose, we included a fourth test case that applied the DeepONet to the surrogation of a two-dimensional rigid body’s dynamics characterized by a combination of rotations, translations, and stretching constructed as non-linear functions of time. Our employment of the architecture was by design inconsistent with the neural operator formulation, and the resulting surrogate was only meant to reproduce a single scenario of the dynamics. However, the purpose of this last test case was to show that the DeepONet has the potential to extend the applicability of POD’s frameworks in two main directions:

- The training data is not required to be aligned on spatial and temporal grids
- Predictions can be obtained at generic spatial and temporal coordinates

Additionally, the flexDeepONet extension adds significant advantages for problems that involve symmetries and for which POD-based strategies require a large number of modes:

- It increases the surrogate’s interpretability, as the dynamics are learned on an automatically-discovered moving reference frame. This allows the isolation of the rigid features and the a-posteriori analysis of the frame’s coordinates
- It augments the generalization capabilities as a direct consequence of the previous point. In the last test case, we showed that the flexDeepOnet is able to accurately reconstruct the rigid body even outside the borders of the spatial training window
- It drastically increases the efficiency of the surrogate, as it improves the effectiveness of the projection. For the last test case in which POD needed 150 modes to retain 95% of the cumulative energy, a flexDeepOnet was constructed with only 1,921 trainable parameters, which is 98.8% less than that required by the vanilla architecture, which still resulted in extremely low accuracy

## Acknowledgments

This research was supported by the Exascale Computing Project (17-SC-20-SC), a collaborative effort of the U.S. Department of Energy Office of Science and the National Nuclear Security Administration. Sandia National Laboratories is a multimission laboratory managed and operated by National Technology and Engineering Solutions of Sandia, LLC., a wholly owned subsidiary of Honeywell International, Inc., for the U.S. Department of Energy’s National Nuclear Security Administration under contract DE-NA-0003525. This paper describes objective technical results and analysis. Any subjective views or opinions that might be expressed in the paper do not necessarily represent the views of the U.S. Department of Energy or the United States Government.

## References

- [1] K. Lee and K. T. Carlberg. “Model reduction of dynamical systems on nonlinear manifolds using deep convolutional autoencoders”. In: *Journal of Computational Physics* 404 (2020), p. 108973. ISSN: 0021-9991. DOI: <https://doi.org/10.1016/j.jcp.2019.108973>.
- [2] S. L. Brunton, B. R. Noack, and P. Koumoutsakos. “Machine Learning for Fluid Mechanics”. In: *Annual Review of Fluid Mechanics* 52.1 (2020), pp. 477–508. DOI: 10.1146/annurev-fluid-010719-060214. eprint: <https://doi.org/10.1146/annurev-fluid-010719-060214>.
- [3] E. Qian et al. “Lift & Learn: Physics-informed machine learning for large-scale nonlinear dynamical systems”. In: *Physica D: Nonlinear Phenomena* 406 (2020), p. 132401. ISSN: 0167-2789. DOI: <https://doi.org/10.1016/j.physd.2020.132401>.

- [4] M. Reichstein et al. “Deep learning and process understanding for data-driven Earth system science”. In: *Nature* 566 (Feb. 2019), p. 195. DOI: 10.1038/s41586-019-0912-1.
- [5] M. Raissi, P. Perdikaris, and G. Karniadakis. “Physics-informed neural networks: A deep learning framework for solving forward and inverse problems involving nonlinear partial differential equations”. In: *Journal of Computational Physics* 378 (2019), pp. 686–707. ISSN: 0021-9991. DOI: <https://doi.org/10.1016/j.jcp.2018.10.045>.
- [6] J. Sirignano and K. Spiliopoulos. “DGM: A deep learning algorithm for solving partial differential equations”. In: *Journal of Computational Physics* 375 (2018), pp. 1339–1364. ISSN: 0021-9991. DOI: <https://doi.org/10.1016/j.jcp.2018.08.029>.
- [7] G. Karniadakis et al. “Physics-informed machine learning”. In: *Nat Rev Phys* 3 (May 2021), pp. 422–440. DOI: 10.1038/s42254-021-00314-5.
- [8] Z. Li et al. “Neural operator: Graph kernel network for partial differential equations”. In: *arXiv preprint arXiv:2003.03485* (2020).
- [9] Z. Li et al. “Fourier neural operator for parametric partial differential equations”. In: *arXiv preprint arXiv:2010.08895* (2020).
- [10] N. Kovachki et al. “Neural Operator: Learning Maps Between Function Spaces”. In: *arXiv preprint arXiv:2108.08481* (2021).
- [11] T. Chen and H. Chen. “Universal approximation to nonlinear operators by neural networks with arbitrary activation functions and its application to dynamical systems”. In: *IEEE Transactions on Neural Networks* 6.4 (1995), pp. 911–917. DOI: 10.1109/72.392253.
- [12] L. Lu, P. Jin, and G. E. Karniadakis. “DeepONet: Learning nonlinear operators for identifying differential equations based on the universal approximation theorem of operators”. In: (Oct. 2019). DOI: 10.1038/s42256-021-00302-5.
- [13] L. Lu et al. “Learning nonlinear operators via DeepONet based on the universal approximation theorem of operators”. In: *Nature Machine Intelligence* 3 (3 Mar. 2021), pp. 218–229. ISSN: 25225839. DOI: 10.1038/s42256-021-00302-5.
- [14] K. Bhattacharya et al. “Model Reduction and Neural Networks for Parametric PDEs”. In: *arXiv preprint arXiv:2005.03180* (2020).
- [15] N. Trask et al. “GMLS-Nets: A framework for learning from unstructured data”. In: *arXiv preprint arXiv:1909.05371* (2019).
- [16] C. Gin et al. “DeepGreen: deep learning of Green’s functions for nonlinear boundary value problems”. In: *Scientific Reports* 11 (2021).
- [17] R. G. Patel et al. “A physics-informed operator regression framework for extracting data-driven continuum models”. In: *Computer Methods in Applied Mechanics and Engineering* 373 (2021), p. 113500. ISSN: 0045-7825. DOI: <https://doi.org/10.1016/j.cma.2020.113500>.
- [18] H. You et al. “Nonlocal Kernel Network (NKN): a Stable and Resolution-Independent Deep Neural Network”. In: *arXiv preprint arXiv:2201.02217* (2022).
- [19] G. Kissas et al. “Learning Operators with Coupled Attention”. In: *arXiv preprint arXiv:2201.01032* (2022).
- [20] S. De et al. *Bi-fidelity Modeling of Uncertain and Partially Unknown Systems using DeepONets*. 2022. DOI: 10.48550/ARXIV.2204.00997.
- [21] A. A. Howard et al. *Multifidelity Deep Operator Networks*. 2022. DOI: 10.48550/ARXIV.2204.09157.
- [22] L. Lu et al. *Multifidelity deep neural operators for efficient learning of partial differential equations with application to fast inverse design of nanoscale heat transport*. 2022. DOI: 10.48550/ARXIV.2204.06684.
- [23] C. Lin et al. “Operator learning for predicting multiscale bubble growth dynamics”. In: *The Journal of Chemical Physics* 154.10 (2021), p. 104118. DOI: 10.1063/5.0041203. eprint: <https://doi.org/10.1063/5.0041203>.
- [24] C. Lin et al. “A seamless multiscale operator neural network for inferring bubble dynamics”. In: *Journal of Fluid Mechanics* 929 (2021), A18. DOI: 10.1017/jfm.2021.866.
- [25] S. Cai et al. “DeepM&Mnet: Inferring the electroconvection multiphysics fields based on operator approximation by neural networks”. In: *Journal of Computational Physics* 436 (2021), p. 110296. ISSN: 0021-9991. DOI: <https://doi.org/10.1016/j.jcp.2021.110296>.
- [26] P. C. Di Leoni et al. “Deeponet prediction of linear instability waves in high-speed boundary layers”. In: *arXiv preprint arXiv:2105.08697* (2021).
- [27] K. M. Gitushi, R. Ranade, and T. Echehki. “Investigation of deep learning methods for efficient high-fidelity simulations in turbulent combustion”. In: *Combustion and Flame* 236 (2022), p. 111814. ISSN: 0010-2180. DOI: <https://doi.org/10.1016/j.combustflame.2021.111814>.

- [28] Z. Mao et al. “DeepM&Mnet for hypersonics: Predicting the coupled flow and finite-rate chemistry behind a normal shock using neural-network approximation of operators”. In: *Journal of Computational Physics* 447 (2021), p. 110698. ISSN: 0021-9991. DOI: <https://doi.org/10.1016/j.jcp.2021.110698>.
- [29] M. P. Sharma, S. Venturi, and M. Panesi. “Application of DeepOnet to model inelastic scattering probabilities in air mixtures”. In: *AIAA AVIATION 2021 FORUM*. DOI: 10.2514/6.2021-3144. eprint: <https://arc.aiaa.org/doi/pdf/10.2514/6.2021-3144>.
- [30] I. Zanardi, S. Venturi, and M. Panesi. “Towards Efficient Simulations of Non-Equilibrium Chemistry in Hypersonic Flows: A Physics-Informed Neural Network Framework”. In: *AIAA SCITECH 2022 Forum*. DOI: 10.2514/6.2022-1639. eprint: <https://arc.aiaa.org/doi/pdf/10.2514/6.2022-1639>.
- [31] J. D. Osorio et al. “Forecasting solar-thermal systems performance under transient operation using a data-driven machine learning approach based on the deep operator network architecture”. In: *Energy Conversion and Management* 252 (2022), p. 115063. ISSN: 0196-8904. DOI: <https://doi.org/10.1016/j.enconman.2021.115063>.
- [32] S. Goswami et al. “A physics-informed variational DeepONet for predicting crack path in quasi-brittle materials”. In: *Computer Methods in Applied Mechanics and Engineering* 391 (2022), p. 114587. ISSN: 0045-7825. DOI: <https://doi.org/10.1016/j.cma.2022.114587>.
- [33] V. Oommen et al. *Learning two-phase microstructure evolution using neural operators and autoencoder architectures*. 2022. DOI: 10.48550/ARXIV.2204.07230.
- [34] M. Yin et al. “Simulating progressive intramural damage leading to aortic dissection using DeepONet: an operator-regression neural network”. In: *Journal of the Royal Society, Interface* 19.187 (Feb. 2022), p. 20210670. ISSN: 1742-5689. DOI: 10.1098/rsif.2021.0670.
- [35] L. Liu and W. Cai. “Multiscale DeepONet for Nonlinear Operators in Oscillatory Function Spaces for Building Seismic Wave Responses”. In: *arXiv preprint arXiv:2111.04860* (2021).
- [36] I. M. S. Leite, J. D. M. Yamim, and L. G. da Fonseca. “The DeepONets for Finance: An Approach to Calibrate the Heston Model”. In: *Progress in Artificial Intelligence*. Ed. by G. Marreiros et al. Cham: Springer International Publishing, 2021, pp. 351–362.
- [37] C. Remlinger, J. Mikael, and R. Elie. *Robust Operator Learning to Solve PDE*. Working Papers hal-03599726. HAL, Mar. 2022.
- [38] S. Wang and P. Perdikaris. “Long-time integration of parametric evolution equations with physics-informed DeepONets”. In: *arXiv preprint arXiv:2106.05384* (June 2021).
- [39] S. Wang, H. Wang, and P. Perdikaris. “Improved architectures and training algorithms for deep operator networks”. In: *arXiv preprint arXiv:2110.01654* (Oct. 2021).
- [40] S. Wang, H. Wang, and P. Perdikaris. “Learning the solution operator of parametric partial differential equations with physics-informed DeepONets”. In: *Science Advances* 7.40 (2021), eabi8605. DOI: 10.1126/sciadv.abi8605. eprint: <https://www.science.org/doi/pdf/10.1126/sciadv.abi8605>.
- [41] E. Beltrami. “On bilinear functions”. In: *SVD and Signal Processing III*. Ed. by M. Moonen and B. De Moor. Amsterdam: Elsevier Science B.V., 1995, pp. 5–18. ISBN: 978-0-444-82107-2. DOI: <https://doi.org/10.1016/B978-044482107-2/50002-9>.
- [42] C. Jordan. “Mémoire sur les formes bilinéaires.” In: *Journal de Mathématiques Pures et Appliquées* 19 (1875), pp. 35–54.
- [43] G. Stewart. “Stewart, G.W.: On the early history of the singular value decomposition. *SIAM Rev.* 35(4), 551-566”. In: *SIAM Review* 35 (Mar. 2001). DOI: 10.1137/1035134.
- [44] L. Sirovich. “Turbulence and the Dynamics of Coherent Structures Part III: Dynamics and Scaling”. In: *Quarterly of Applied Mathematics* 45.3 (1987), pp. 583–590. ISSN: 0033569X, 15524485.
- [45] G. Berkooz, P. Holmes, and J. L. Lumley. “The Proper Orthogonal Decomposition in the Analysis of Turbulent Flows”. In: *Annual Review of Fluid Mechanics* 25.1 (1993), pp. 539–575. DOI: 10.1146/annurev.fl.25.010193.002543. eprint: <https://doi.org/10.1146/annurev.fl.25.010193.002543>.
- [46] M. Rathinam and L. R. Petzold. “A New Look at Proper Orthogonal Decomposition”. In: *SIAM Journal on Numerical Analysis* 41.5 (2004), pp. 1893–1925. ISSN: 00361429.
- [47] M. Hinze and S. Volkwein. “Proper Orthogonal Decomposition Surrogate Models for Nonlinear Dynamical Systems: Error Estimates and Suboptimal Control”. In: *Dimension Reduction of Large-Scale Systems*. Ed. by P. Benner, D. C. Sorensen, and V. Mehrmann. Berlin, Heidelberg: Springer Berlin Heidelberg, 2005, pp. 261–306. ISBN: 978-3-540-27909-9.
- [48] S. L. Brunton and J. N. Kutz. “Singular Value Decomposition (SVD)”. In: *Data-Driven Science and Engineering: Machine Learning, Dynamical Systems, and Control*. Cambridge University Press, 2019, pp. 3–46. DOI: 10.1017/9781108380690.002.

- [49] P. S. Hadorn. “Shift-DeepONet: Extending Deep Operator Networks for Discontinuous Output Functions”. PhD thesis. ETH Zurich, Seminar for Applied Mathematics, Mar. 2022.
- [50] J. Reiss et al. “The Shifted Proper Orthogonal Decomposition: A Mode Decomposition for Multiple Transport Phenomena”. In: *SIAM Journal on Scientific Computing* 40.3 (2018), A1322–A1344. DOI: 10.1137/17M1140571. eprint: <https://doi.org/10.1137/17M1140571>.
- [51] J. Reiss. “Model reduction for convective problems: formulation and application”. In: *IFAC-PapersOnLine* 51.2 (2018). 9th Vienna International Conference on Mathematical Modelling, pp. 186–189. ISSN: 2405-8963. DOI: <https://doi.org/10.1016/j.ifacol.2018.03.032>.
- [52] D. Papapicco et al. “The Neural Network shifted-proper orthogonal decomposition: A machine learning approach for non-linear reduction of hyperbolic equations”. In: *Computer Methods in Applied Mechanics and Engineering* 392 (2022), p. 114687. ISSN: 0045-7825. DOI: <https://doi.org/10.1016/j.cma.2022.114687>.
- [53] L. Lu et al. “A comprehensive and fair comparison of two neural operators (with practical extensions) based on FAIR data”. In: *Computer Methods in Applied Mechanics and Engineering* 393 (2022), p. 114778. ISSN: 0045-7825. DOI: <https://doi.org/10.1016/j.cma.2022.114778>.
- [54] S. Lanthaler, S. Mishra, and G. Karniadakis. “Error estimates for DeepONets: a deep learning framework in infinite dimensions”. In: *Transactions of Mathematics and Its Applications* 6 (Mar. 2022). DOI: 10.1093/imatrm/tnac001.
- [55] B. Deng et al. “Convergence rate of DeepONets for learning operators arising from advection-diffusion equations”. In: *arXiv preprint arXiv:2102.10621* (2021).
- [56] C. Marcati and C. Schwab. “Exponential Convergence of Deep Operator Networks for Elliptic Partial Differential Equations”. In: *arXiv preprint arXiv:2112.08125* abs/2112.08125 (2021).
- [57] Martín Abadi et al. *TensorFlow: Large-Scale Machine Learning on Heterogeneous Systems*. Software available from tensorflow.org, 2015.
- [58] D. P. Kingma and J. Ba. “Adam: A method for stochastic optimization”. In: *arXiv preprint arXiv:1412.6980* (2014).
- [59] K. F. Pearson. “LIII. On lines and planes of closest fit to systems of points in space”. In: *The London, Edinburgh, and Dublin Philosophical Magazine and Journal of Science* 2.11 (1901), pp. 559–572. DOI: 10.1080/14786440109462720. eprint: <https://doi.org/10.1080/14786440109462720>.
- [60] H. Hotelling. “Analysis of a complex of statistical variables into principal components.” In: *Journal of Educational Psychology* 24.6 (1933), pp. 417–441. DOI: 10.1037/h0071325.
- [61] I. T. Jolliffe. “Principal Component Analysis”. In: *International Encyclopedia of Statistical Science*. Ed. by M. Lovric. Berlin, Heidelberg: Springer Berlin Heidelberg, 2011, pp. 1094–1096. ISBN: 978-3-642-04898-2. DOI: 10.1007/978-3-642-04898-2\_455.
- [62] I. T. Jolliffe and J. Cadima. “Principal component analysis: a review and recent developments”. In: *Philosophical Transactions of the Royal Society A: Mathematical, Physical and Engineering Sciences* 374 (2016).
- [63] K. Karhunen. *Ueber lineare Methoden in der Wahrscheinlichkeitsrechnung*. Soumalainen Tiedekatemia, 1947.
- [64] M. Loeve. *Probability Theory*. 4th ed. London: New York, Van Nostrand Reinhold, 1963. ISBN: 0387902104.
- [65] P. C. Hansen. “Computation of the singular value expansion”. In: *Computing* 40 (1988), pp. 185–199.
- [66] P. Schmid and J. Sesterhenn. “Dynamic Mode Decomposition of numerical and experimental data”. In: *Journal of Fluid Mechanics* 656 (Nov. 2008). DOI: 10.1017/S0022112010001217.
- [67] P. Schmid. “Dynamic mode decomposition of numerical and experimental data”. In: 25 (July 2010), pp. 249–259.
- [68] S. L. Brunton and J. N. Kutz. “Data-Driven Dynamical Systems”. In: *Data-Driven Science and Engineering: Machine Learning, Dynamical Systems, and Control*. Cambridge University Press, 2019, pp. 229–275. DOI: 10.1017/9781108380690.008.
- [69] D. B. Lloyd Trefethen. *Numerical Linear Algebra*. Philadelphia: SIAM, 1997.
- [70] R. A. van den Berg et al. “Centering, scaling, and transformations: improving the biological information content of metabolomics data”. In: *BMC Genomics* 7 (2006), pp. 142–142.
- [71] A. Parente and J. C. Sutherland. “Principal component analysis of turbulent combustion data: Data pre-processing and manifold sensitivity”. In: *Combustion and Flame* 160.2 (2013), pp. 340–350. ISSN: 0010-2180. DOI: <https://doi.org/10.1016/j.combustflame.2012.09.016>.
- [72] E. Armstrong and J. C. Sutherland. “A technique for characterising feature size and quality of manifolds”. In: *Combustion Theory and Modelling* 25.4 (2021), pp. 646–668. DOI: 10.1080/13647830.2021.1931715. eprint: <https://doi.org/10.1080/13647830.2021.1931715>.
- [73] K. Zdybal et al. “PCAFold: Python software to generate, analyze and improve PCA-derived low-dimensional manifolds”. In: *SoftwareX* 12 (2020), p. 100630.

- [74] M. D. McKay, R. J. Beckman, and W. J. Conover. “Comparison of Three Methods for Selecting Values of Input Variables in the Analysis of Output from a Computer Code”. In: *Technometrics* 21.2 (1979), pp. 239–245. DOI: 10.1080/00401706.1979.10489755. eprint: <https://doi.org/10.1080/00401706.1979.10489755>.
- [75] P. G. Constantine et al. “Model Reduction With MapReduce-enabled Tall and Skinny Singular Value Decomposition”. In: *SIAM Journal on Scientific Computing* 36.5 (2014), S166–S191. DOI: 10.1137/130925219. eprint: <https://doi.org/10.1137/130925219>.
- [76] B. Meuris, S. Qadeer, and P. Stinis. “Machine-learning custom-made basis functions for partial differential equations”. In: *arXiv preprint arXiv:2111.05307* (2021).
- [77] K. Kontolati et al. *On the influence of over-parameterization in manifold based surrogates and deep neural operators*. 2022. DOI: 10.48550/ARXIV.2203.05071.
- [78] J. S. Hesthaven and S. Ubbiali. “Non-intrusive reduced order modeling of nonlinear problems using neural networks”. In: *Journal of Computational Physics* 363 (June 2018), pp. 55–78. ISSN: 10902716. DOI: 10.1016/j.jcp.2018.02.037.
- [79] Q. Wang, J. S. Hesthaven, and D. Ray. “Non-intrusive reduced order modeling of unsteady flows using artificial neural networks with application to a combustion problem”. In: *Journal of Computational Physics* 384 (May 2019), pp. 289–307. ISSN: 10902716. DOI: 10.1016/j.jcp.2019.01.031.
- [80] S. Wang, H. Wang, and P. Perdikaris. “Improved architectures and training algorithms for deep operator networks”. In: *arXiv preprint arXiv:2110.01654* (2021).
- [81] R. Mojjani and M. Balajewicz. *Physics-aware registration based auto-encoder for convection dominated PDEs*. 2020. DOI: 10.48550/ARXIV.2006.15655.
- [82] J. Zhang, S. Zhang, and G. Lin. *MultiAuto-DeepONet: A Multi-resolution Autoencoder DeepONet for Nonlinear Dimension Reduction, Uncertainty Quantification and Operator Learning of Forward and Inverse Stochastic Problems*. 2022. DOI: 10.48550/ARXIV.2204.03193.
- [83] S. L. Brunton and J. N. Kutz. “Reduced Order Models (ROMs)”. In: *Data-Driven Science and Engineering: Machine Learning, Dynamical Systems, and Control*. Cambridge University Press, 2019, pp. 375–402. DOI: 10.1017/9781108380690.012.
- [84] N. Cagniard, Y. Maday, and B. Stamm. “Model Order Reduction for Problems with Large Convection Effects”. In: Jan. 2019, pp. 131–150. ISBN: 978-3-319-78324-6. DOI: 10.1007/978-3-319-78325-3\_10.
- [85] R. Mojjani and M. Balajewicz. “Arbitrary Lagrangian Eulerian framework for efficient projection-based reduction of convection dominated nonlinear flows”. In: *APS Division of Fluid Dynamics Meeting Abstracts*. APS Meeting Abstracts. Nov. 2017, M1.008, p. M1.008.
- [86] D. Rim, S. Moe, and R. J. LeVeque. “Transport Reversal for Model Reduction of Hyperbolic Partial Differential Equations”. In: *SIAM/ASA Journal on Uncertainty Quantification* 6.1 (2018), pp. 118–150. DOI: 10.1137/17M1113679. eprint: <https://doi.org/10.1137/17M1113679>.
- [87] N. J. Nair and M. Balajewicz. “Transported snapshot model order reduction approach for parametric, steady-state fluid flows containing parameter-dependent shocks”. In: *International Journal for Numerical Methods in Engineering* 117.12 (2019), pp. 1234–1262.
- [88] T. Taddei. “A Registration Method for Model Order Reduction: Data Compression and Geometry Reduction”. In: *SIAM Journal on Scientific Computing* 42.2 (2020), A997–A1027. DOI: 10.1137/19M1271270. eprint: <https://doi.org/10.1137/19M1271270>.
- [89] T. Poinso and D. Veynante. “Theoretical and Numerical Combustion”. In: *Prog. Energy Combust. Sci.* 28 (Jan. 2005).
- [90] G. Smith et al. “GRI-Mech 3.0”. In: <http://www.me.berkeley.edu/gri-mech/> (Jan. 1999).
- [91] D. G. Goodwin et al. *Cantera: An Object-oriented Software Toolkit for Chemical Kinetics, Thermodynamics, and Transport Processes*. <https://www.cantera.org>. Version 2.5.1. 2021. DOI: 10.5281/zenodo.4527812.
- [92] M. Lemke et al. “Model Reduction of Reactive Processes”. In: *Active Flow and Combustion Control 2014*. Ed. by R. King. Cham: Springer International Publishing, 2015, pp. 397–413. ISBN: 978-3-319-11967-0.
- [93] M. Lemke et al. “Adjoint-based sensitivity analysis of quantities of interest of complex combustion models”. In: *Combustion Theory and Modelling* 23.1 (2019), pp. 180–196. DOI: 10.1080/13647830.2018.1495845. eprint: <https://doi.org/10.1080/13647830.2018.1495845>.
- [94] P. Jin, S. Meng, and L. Lu. *MIONet: Learning multiple-input operators via tensor product*. 2022. DOI: 10.48550/ARXIV.2202.06137.
- [95] L. Tan and L. Chen. *Enhanced DeepONet for Modeling Partial Differential Operators Considering Multiple Input Functions*. 2022. DOI: 10.48550/ARXIV.2202.08942.

- [96] A. Bernardi et al. “General tensor decomposition, moment matrices and applications”. In: *Journal of Symbolic Computation* 52 (2013). International Symposium on Symbolic and Algebraic Computation, pp. 51–71. ISSN: 0747-7171. DOI: <https://doi.org/10.1016/j.jsc.2012.05.012>.

## S1. Supplementary Material for Test Case 1

### S1.1. Training and Test Scenarios

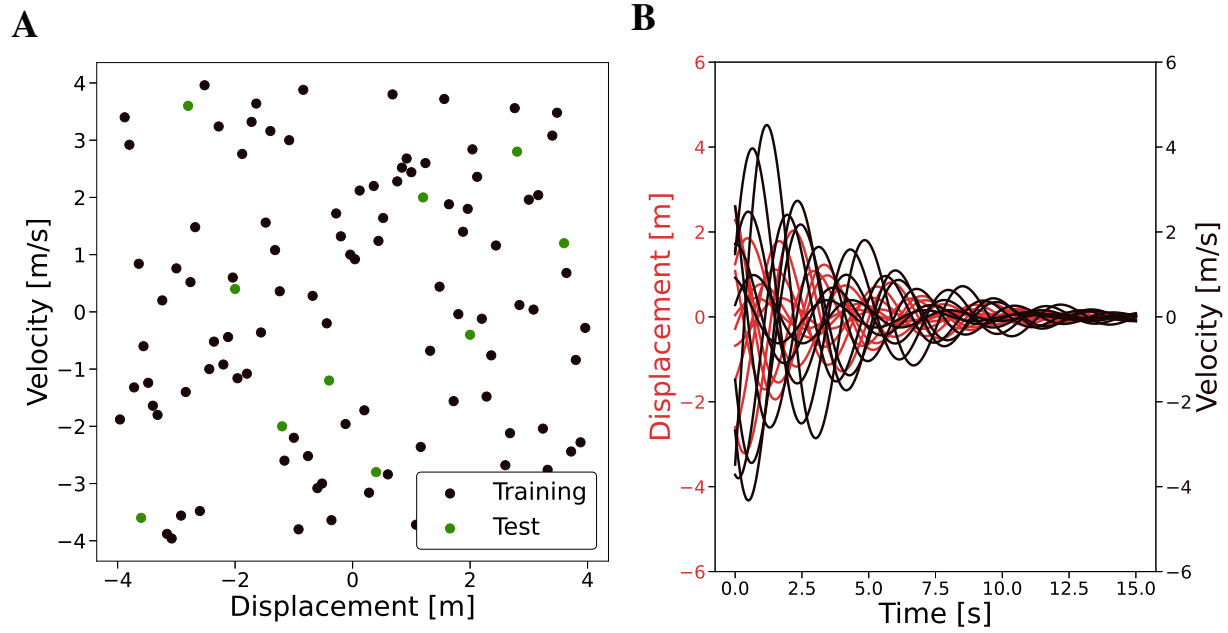


Figure S1: **Training and test data for the mass-spring-damper test case.** (A): Initial conditions, randomly selected based on Latin hypercube sampling. (B): Ten examples of training scenarios.

## S1.2. Vanilla Deep Operator Network (DeepONet)

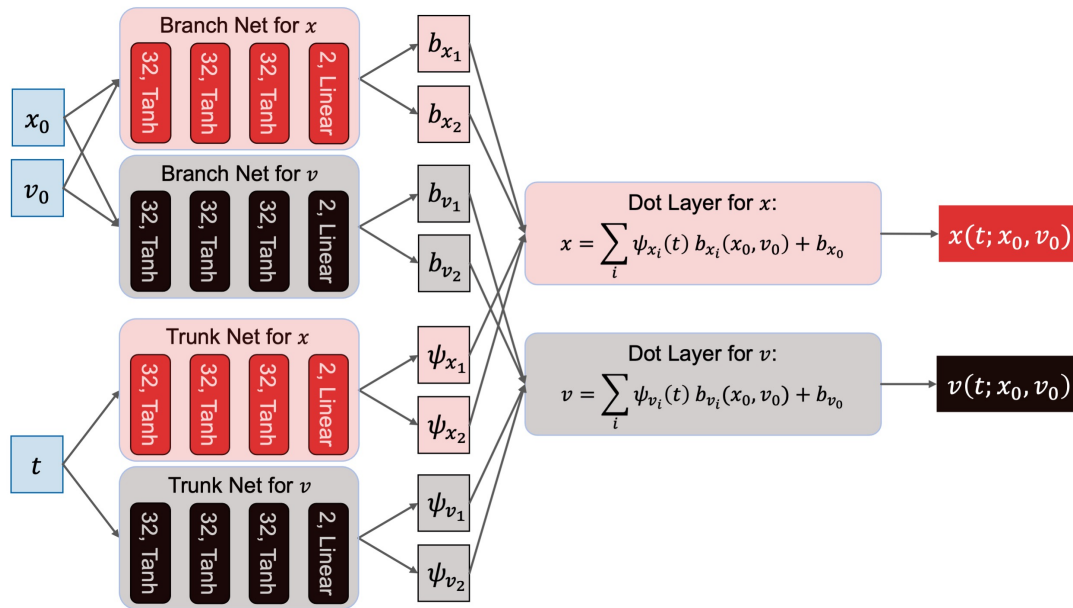


Figure S2: **Architecture of the vanilla DeepONet for the mass-spring-damper test case.** The same architecture is used at both training and prediction phases.



S1.3. Singular Value Decomposition Deep Operator Network (SVD-DeepONet)

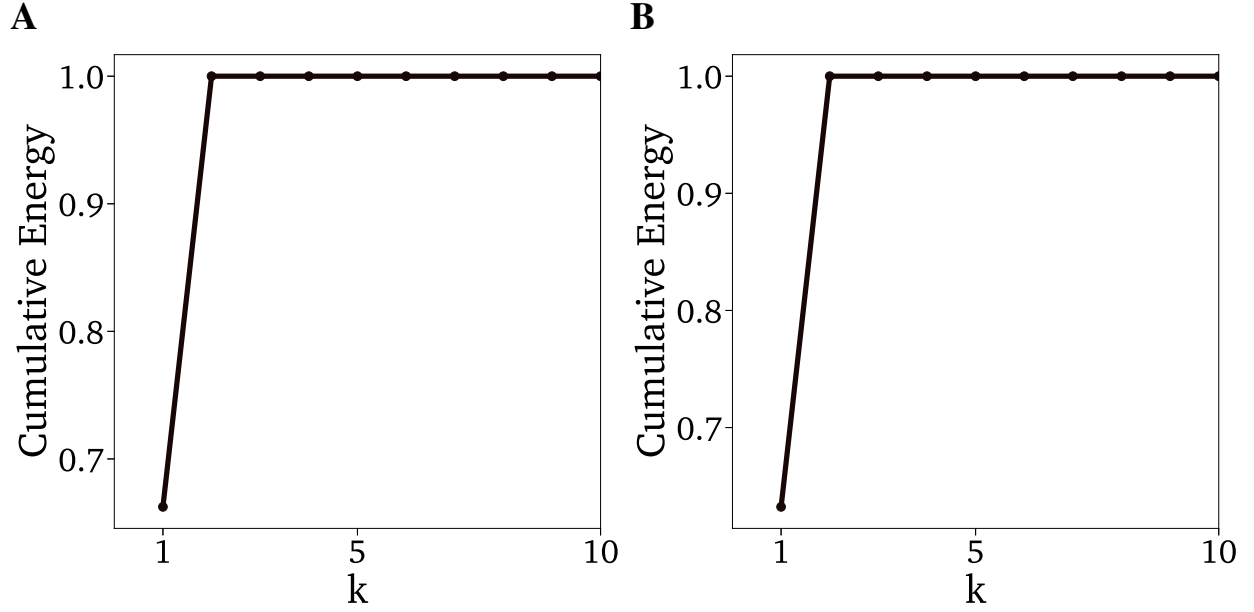


Figure S3: **Cumulative energies of the X and V matrices from the mass-spring-damper test case.** Cumulative energies contained in the first k singular values of X (A) and V (B).

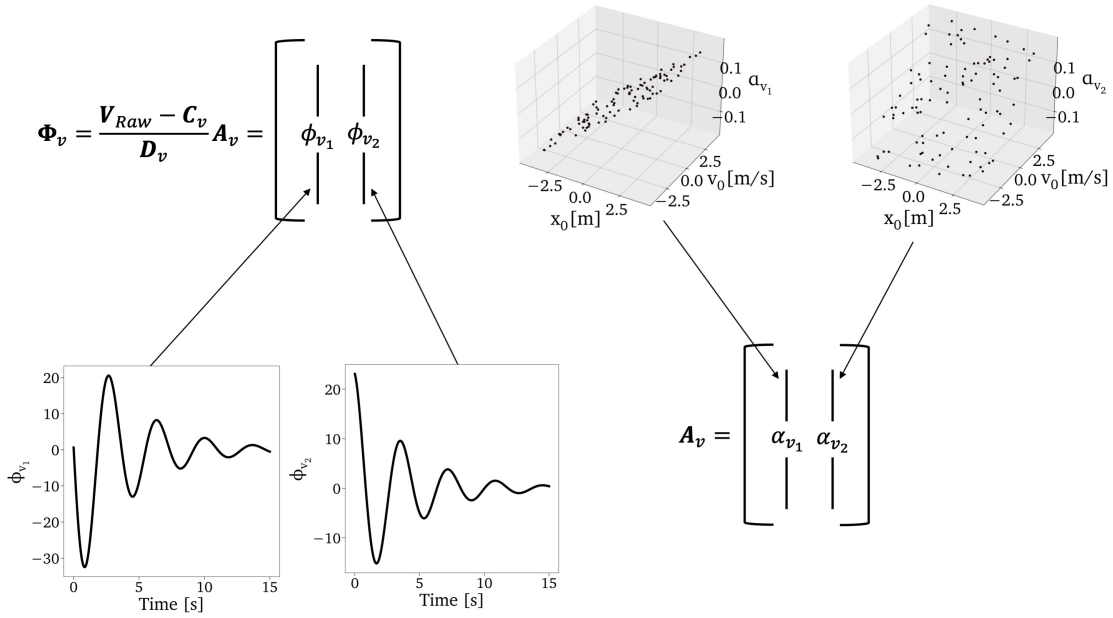


Figure S4: **SVD of the velocity data matrix from the mass-spring-damper test case.** Schematics of the columns resulting from the decomposition.

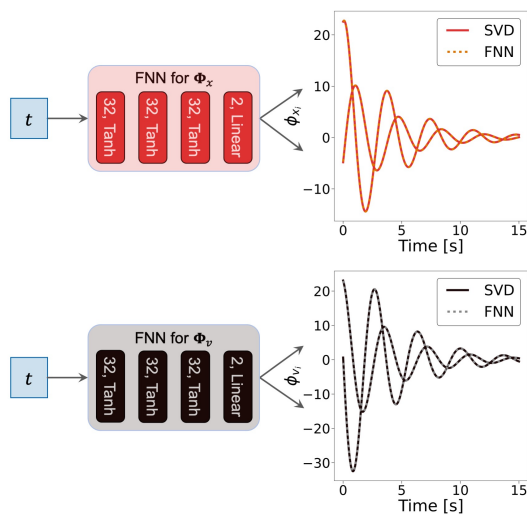
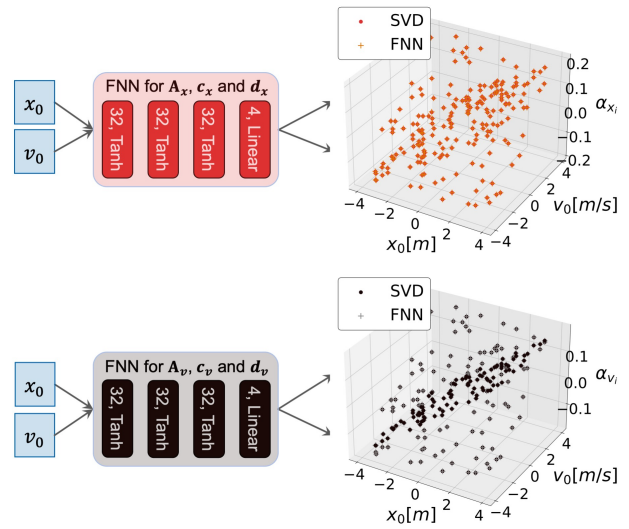
**A****B**

Figure S5: **Architectures of the building blocks for the SVD-DeepONet in the mass-spring-damper test case.** (A): Two feed-forward neural networks (FNN) are trained to reproduce the principal components of  $\mathbf{X}$  and  $\mathbf{V}$ , respectively. (B): Two FNNs are independently trained to retrieve the two columns principal directions, the centering coefficient, and the scaling coefficient for each of the two state variables.

S1.4. Shared-Trunk SVD-DeepONet

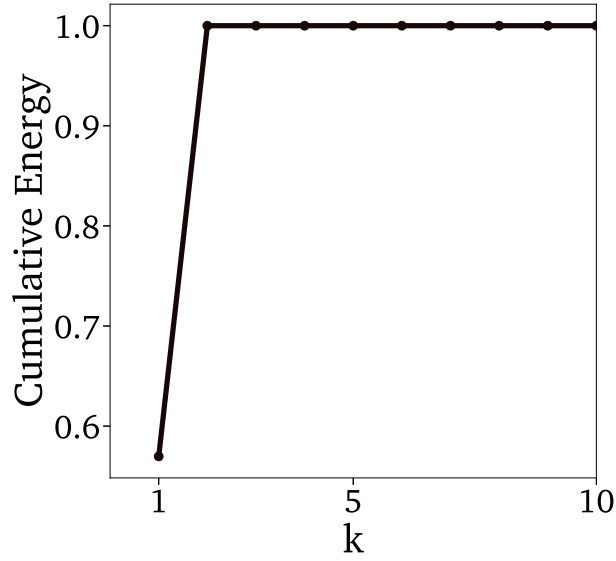


Figure S6: **Cumulative energies of the displacement-velocity combined data matrix,  $Z$ , from the mass-spring-damper test case.** Cumulative energies contained in the first  $k$  singular values of  $Z$ .

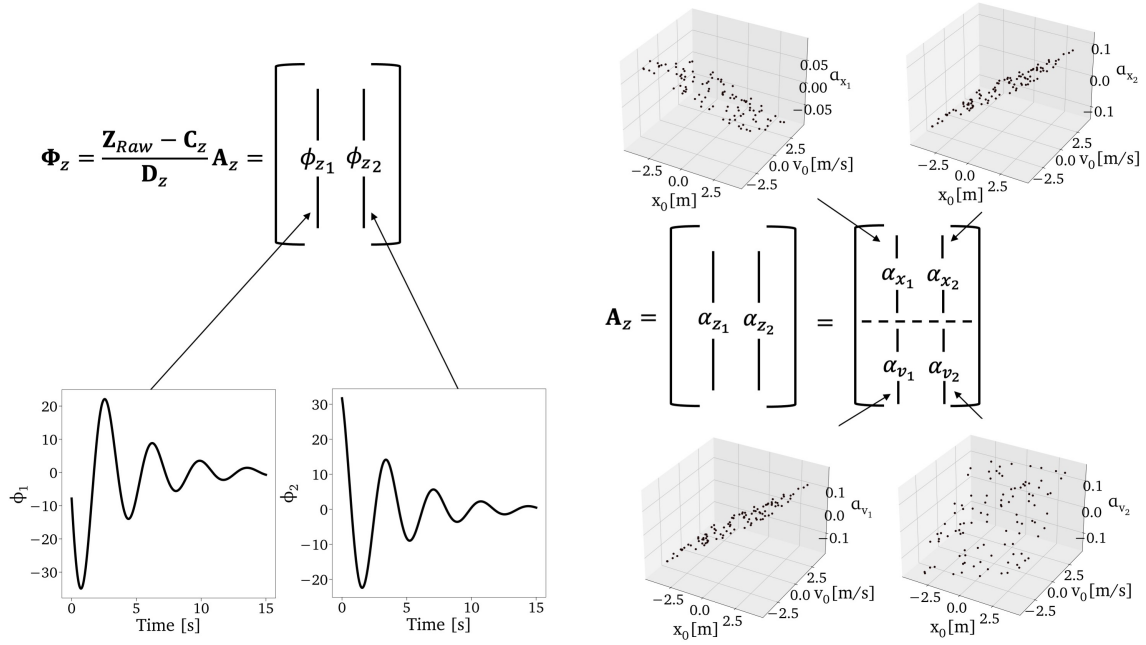


Figure S7: **SVD of the displacement-velocity combined data matrix,  $Z$ , from the mass-spring-damper test case.** Schematics of the columns resulting from the decomposition.

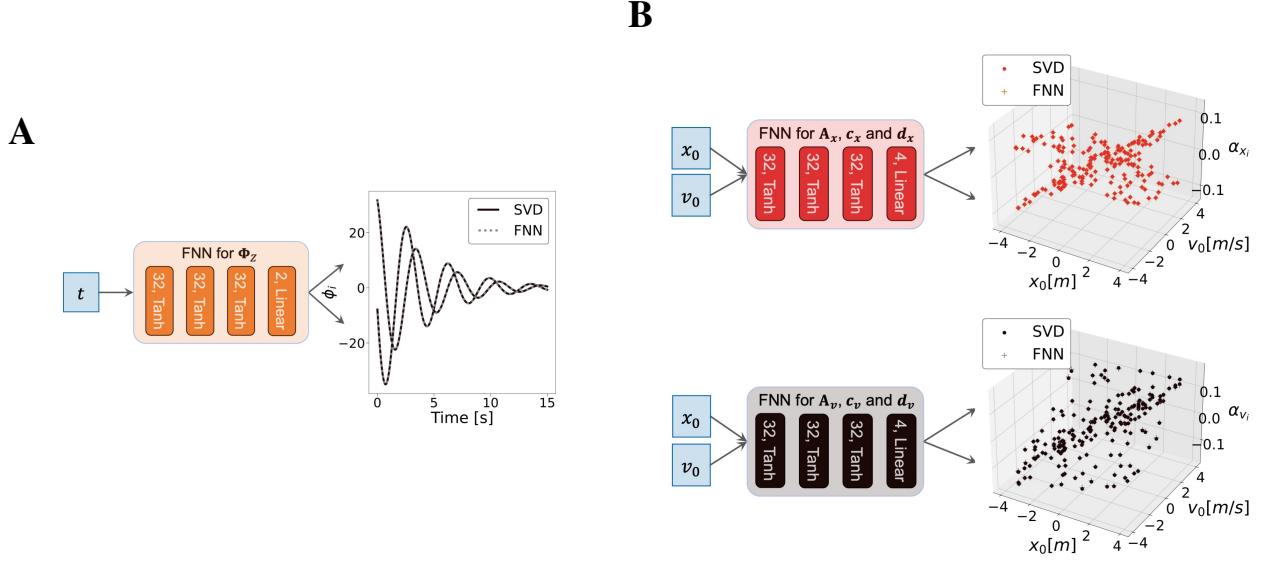


Figure S8: **Architectures of the building blocks for the shared-trunk SVD-DeepONet in the mass-spring-damper test case.** (A): One feed-forward neural networks (FNNs) is trained for reproducing the two principal components of  $\mathbf{Z}$ . (B): Two FNNs are independently trained for retrieving the two principal directions, the centering coefficient, and the scaling coefficient for each of the two state variables.

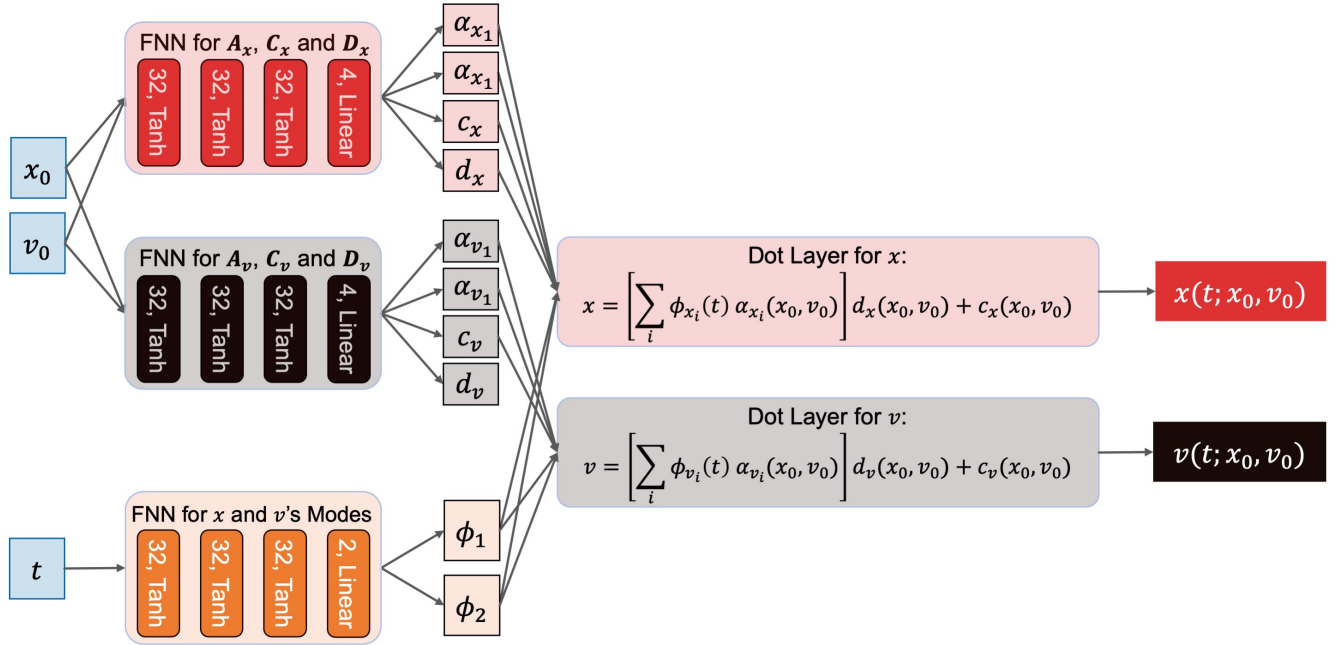


Figure S9: **Assembled architecture of the shared-trunk SVD-DeepONet for the mass-spring-damper test case.** After being independently trained as feed-forward neural networks (FNNs), the three blocks are assembled as DeepONet's trunk net and branch nets to predict displacements and velocities at unseen times and for unseen initial conditions.

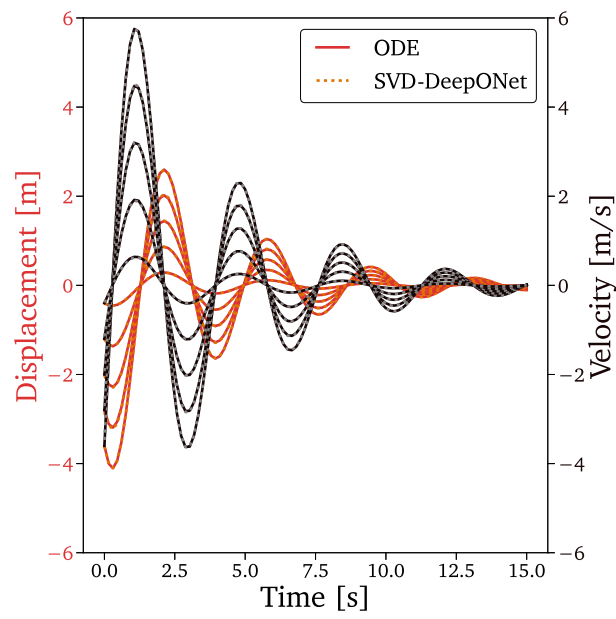


Figure S10: **SVD-DeepONet applied to the mass-spring-damper test case.** Displacements and velocities at five test scenarios from the ODE integration (solid lines) and as predicted by the shared-trunk SVD-DeepONet (overlapping dotted lines).

## S2. Supplementary Material for Test Case 2

### S2.1. Training Scenarios

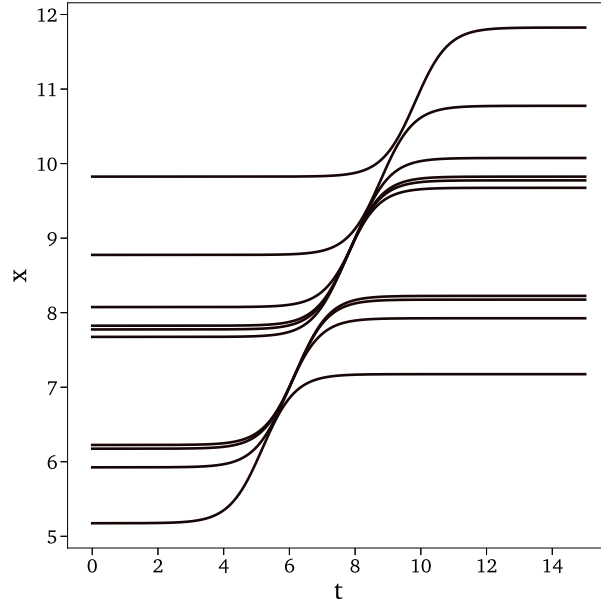


Figure S11: **Training data for the shifting hyperbolic function test case.** Ten examples of training scenarios.

### S2.2. Vanilla Deep Operator Network (DeepONet)

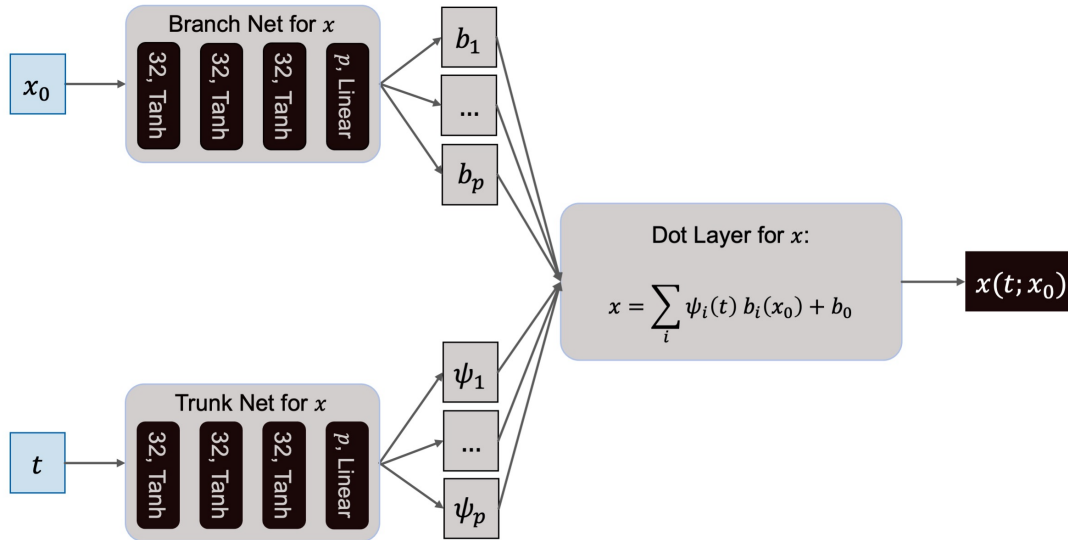


Figure S12: **Architecture of the vanilla DeepONet for the shifting hyperbolic function test case.** We tested multiple configurations with different numbers of trunk and branch's outputs,  $p$ .

### S2.3. Singular Value Decomposition (SVD)

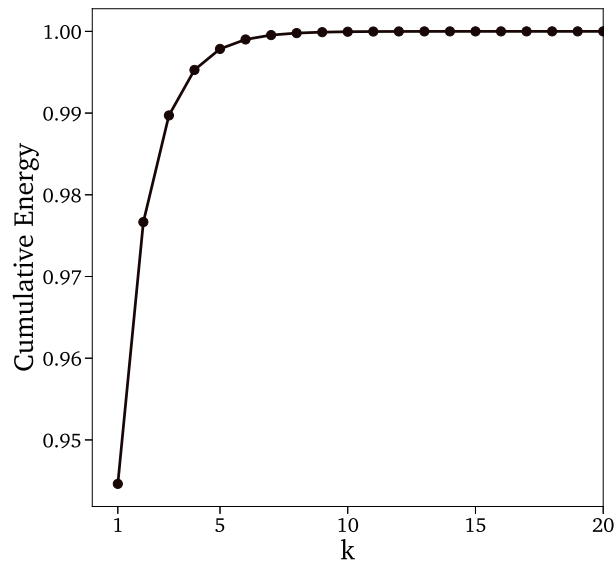


Figure S13: **Cumulative energies of the position data matrix from the shifting hyperbolic function test case.** Cumulative energies contained in  $\mathbf{X}$ 's first  $k$  singular values.

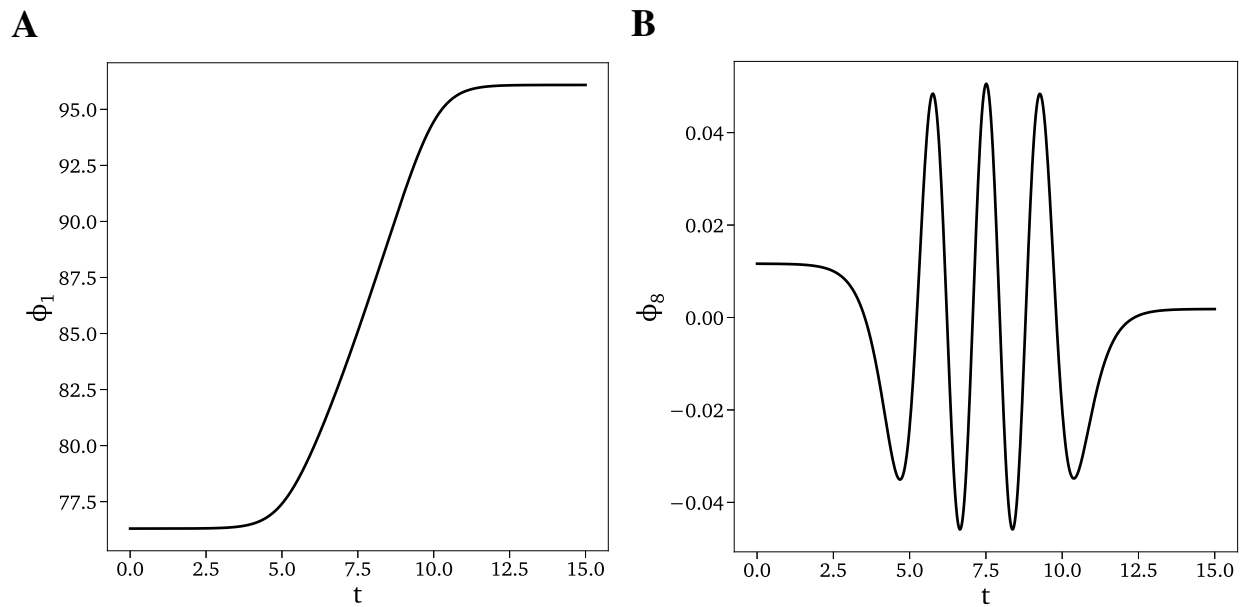


Figure S14: **Principal components of the position data matrix from the shifting hyperbolic function test case.** First (**A**) and eight (**B**) principal components of  $\mathbf{X}$ .

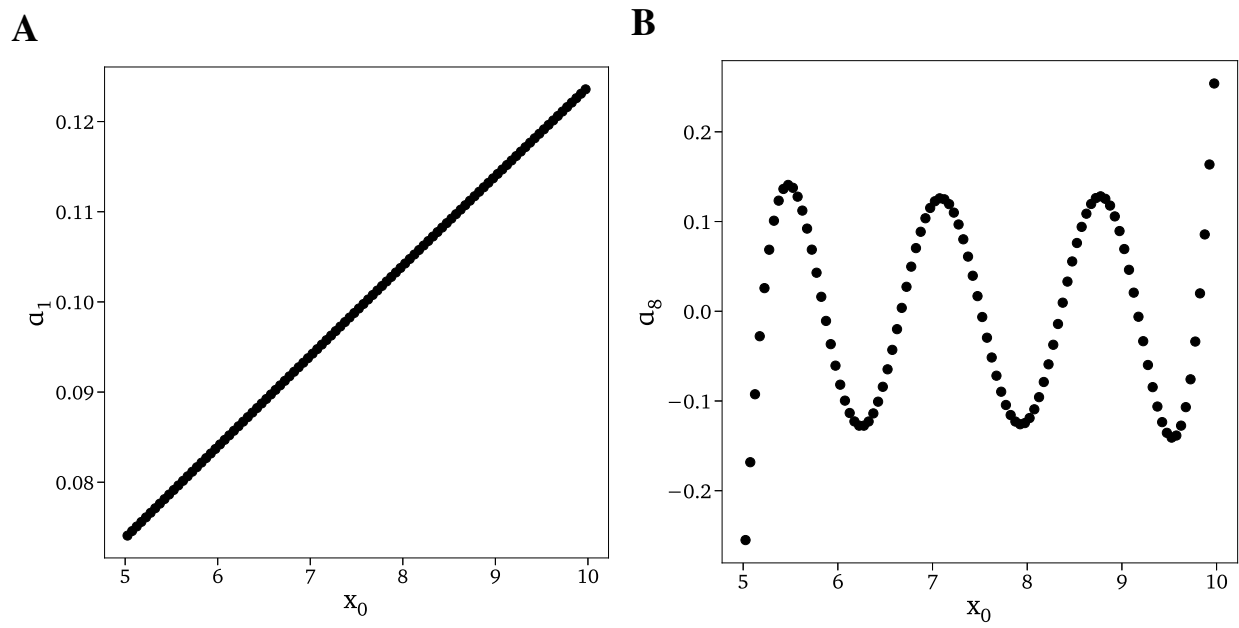


Figure S15: **Coefficients of the principal direction matrix for the shifting hyperbolic function test case.** First (A) and eight (B) columns of  $A_x$ .



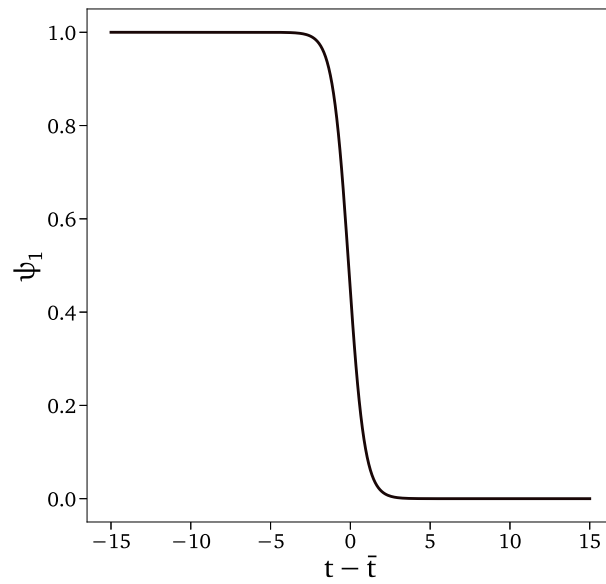
*S2.4. Flexible Deep Operator Network (flexDeepONet)*

Figure S16: **Output of flexDeepONet's trunk for the shifting hyperbolic function test case.** Output of the flexDeepONet's trunk net as function of its input (i.e., as function of the time processed by the shifting block).

### S3. Supplementary Material for Test Case 3

#### S3.1. Training and Test Scenarios

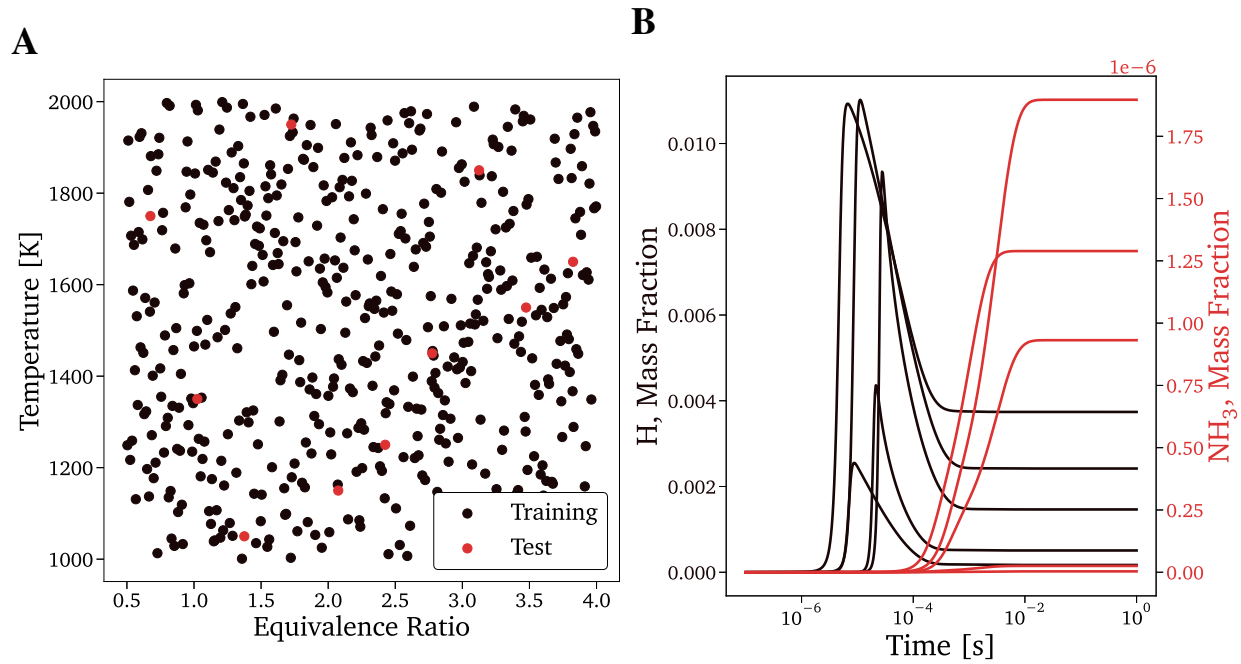


Figure S17: **Training and test data for the combustion chemistry test case.** (A): Initial conditions, randomly selected based on Latin hypercube sampling. (B): Five examples of training scenarios for H and NH<sub>3</sub> mass fractions.

## S3.2. Vanilla DeepONet

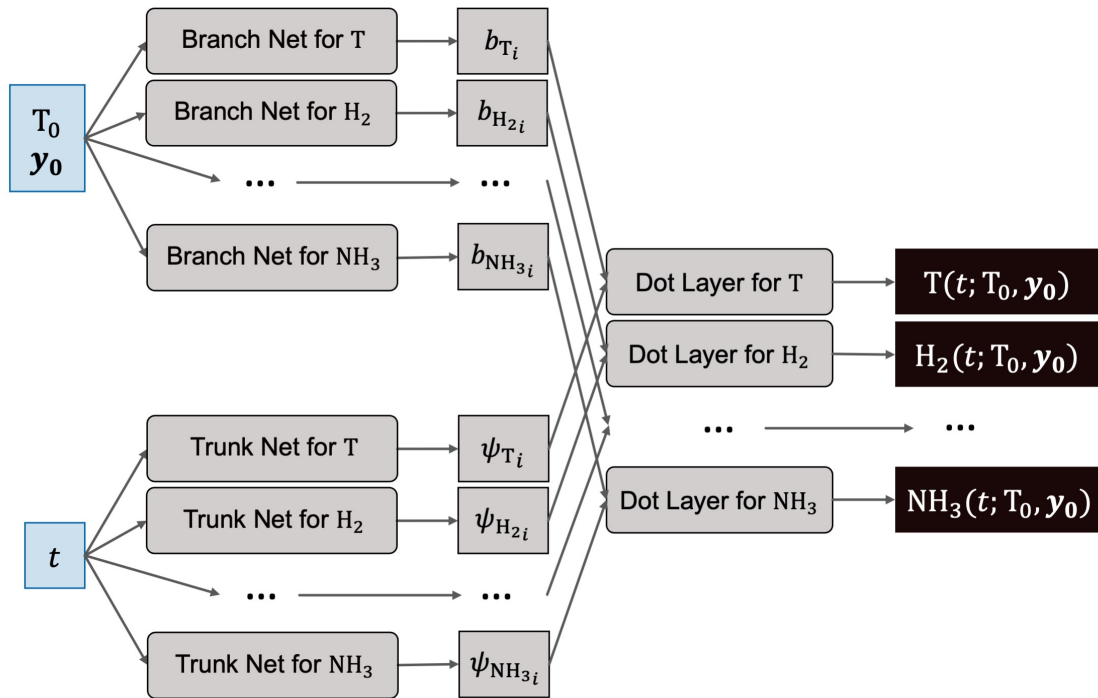


Figure S18: **FlexDeepONet architecture for the combustion chemistry test case.** Each of the 19 thermodynamic state variables has its own trunk and branch nets.

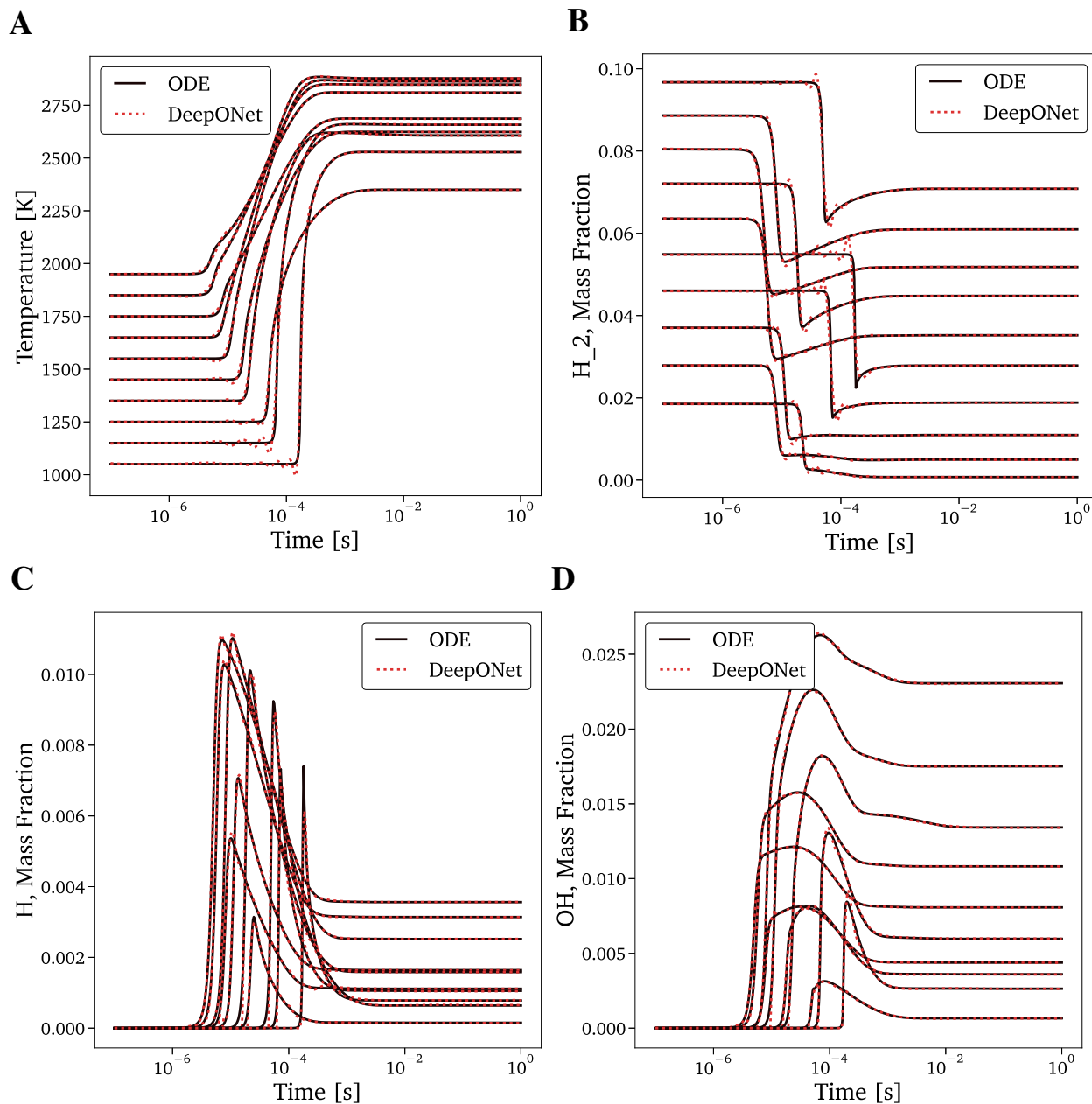


Figure S19: **Predictions of the thermodynamic variables from the Vanilla DeepONet with  $p = 20$ .** Temperature (A), and mass fractions of H<sub>2</sub> (B), H (C), and OH (D) for ten test scenarios as the results of the ODE integration (solid black lines) and as predicted by the Vanilla DeepONet with 20 trunk outputs (red dotted lines).

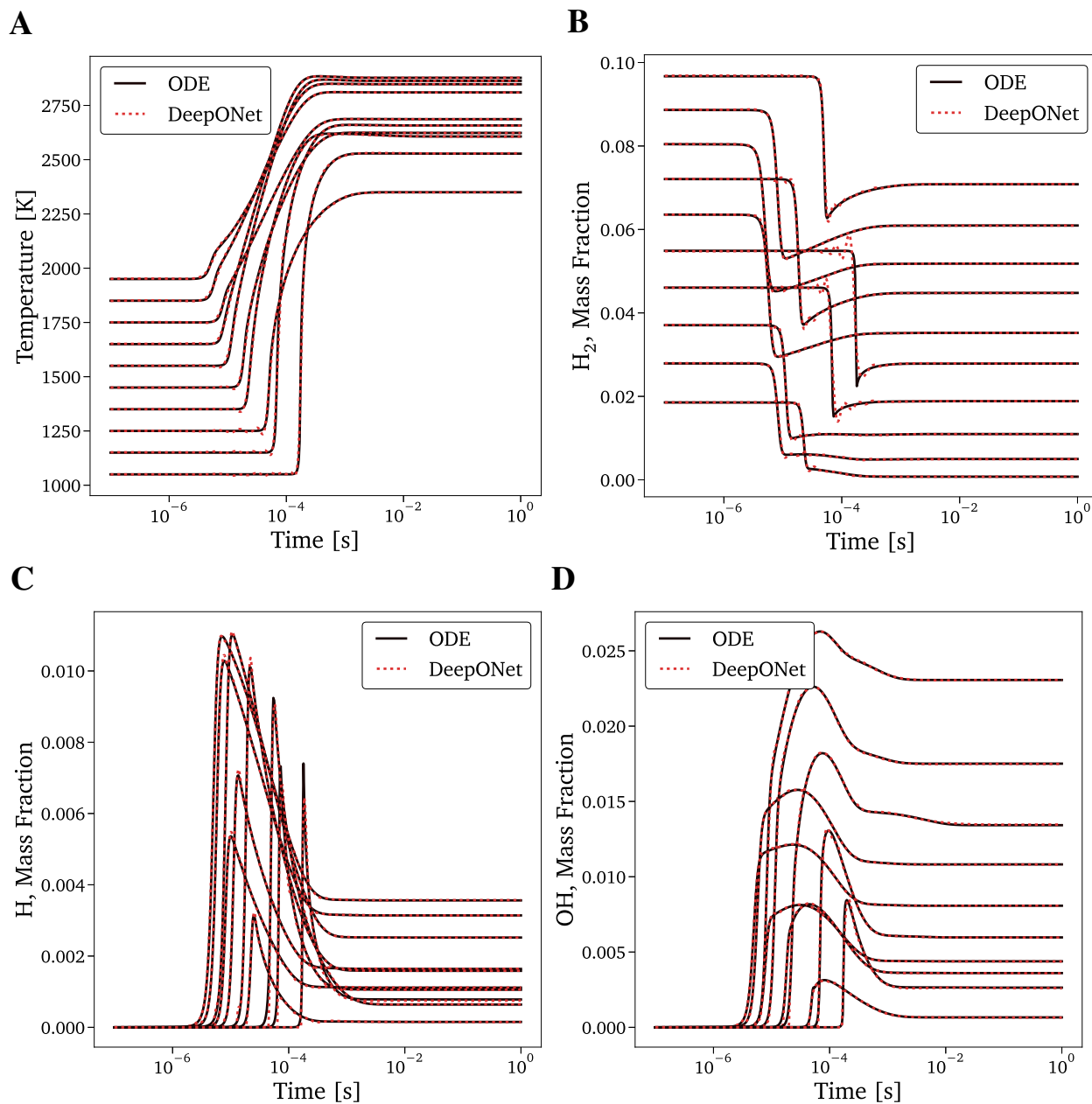


Figure S20: **Predictions of the thermodynamic variables from the vanilla DeepONet with  $p = 32$ .** Temperature (A), and mass fractions of  $H_2$  (B), H (C), and OH (D) for ten test scenarios as the results of the ODE integration (solid black lines) and as predicted by vanilla DeepONet with 32 trunk outputs (red dotted lines).

## S3.3. Singular Value Decomposition (SVD)

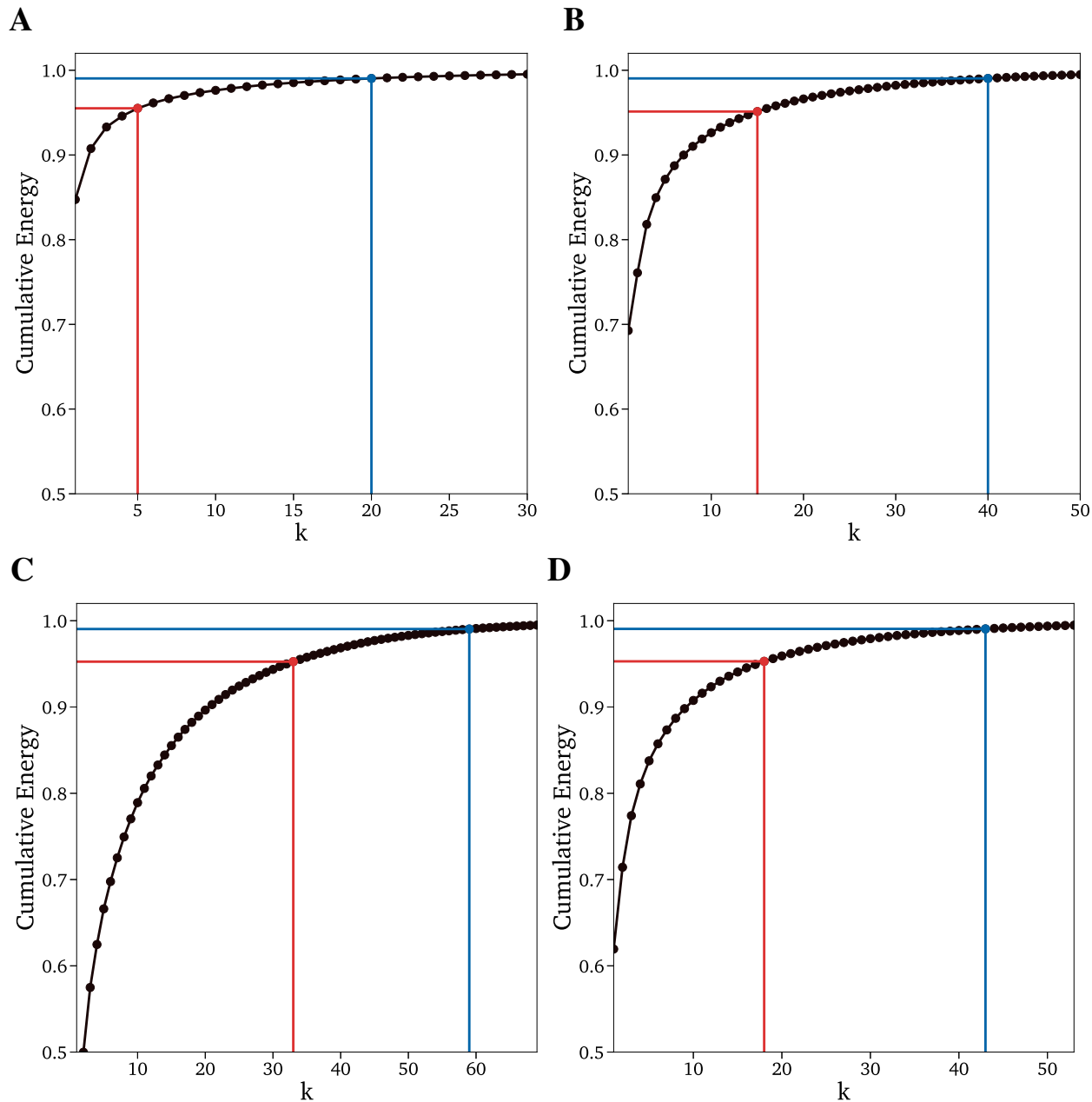


Figure S21: **Cumulative energies of the scenario-aggregated data matrices from the combustion chemistry test case.** Cumulative energies contained in the first  $k$  singular values of the matrices for the temperature (A) and the mass fractions of  $H_2$  (B), H (C), and OH (D). The red and blue dots identify cumulative energies corresponding to 95% and 99%, respectively.

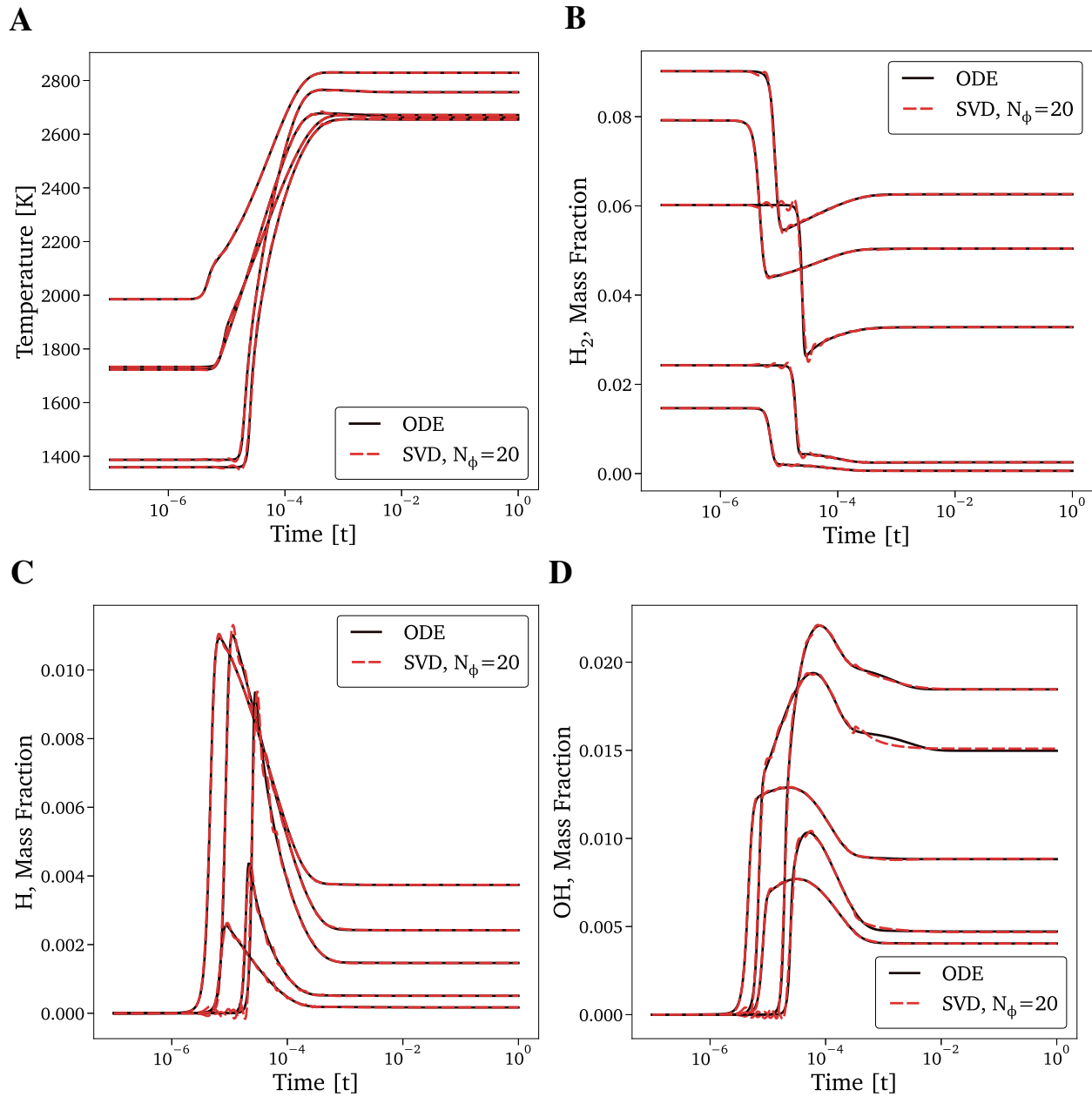


Figure S22: **Training scenarios decomposed and reconstructed via SVD.** Five of the training scenarios from the ODE integration (black solid lines) and after being encoded-decoded based on SVD's first twenty singular values (red dotted lines).

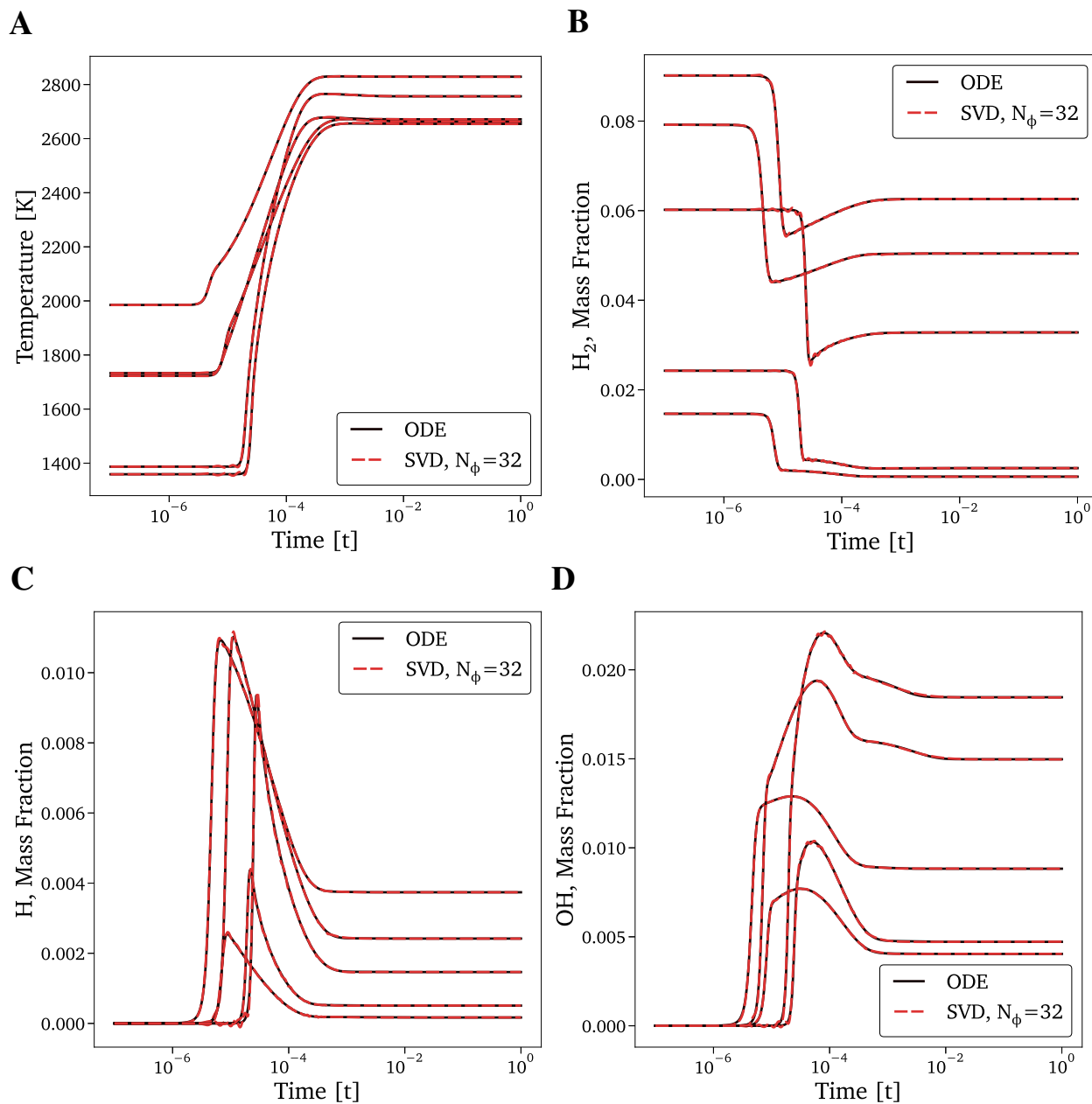


Figure S23: **Training scenarios decomposed and reconstructed via SVD.** Five of the training scenarios from the ODE integration (black solid lines) and after being encoded-decoded based on SVD's first thirty two singular values (red dotted lines).



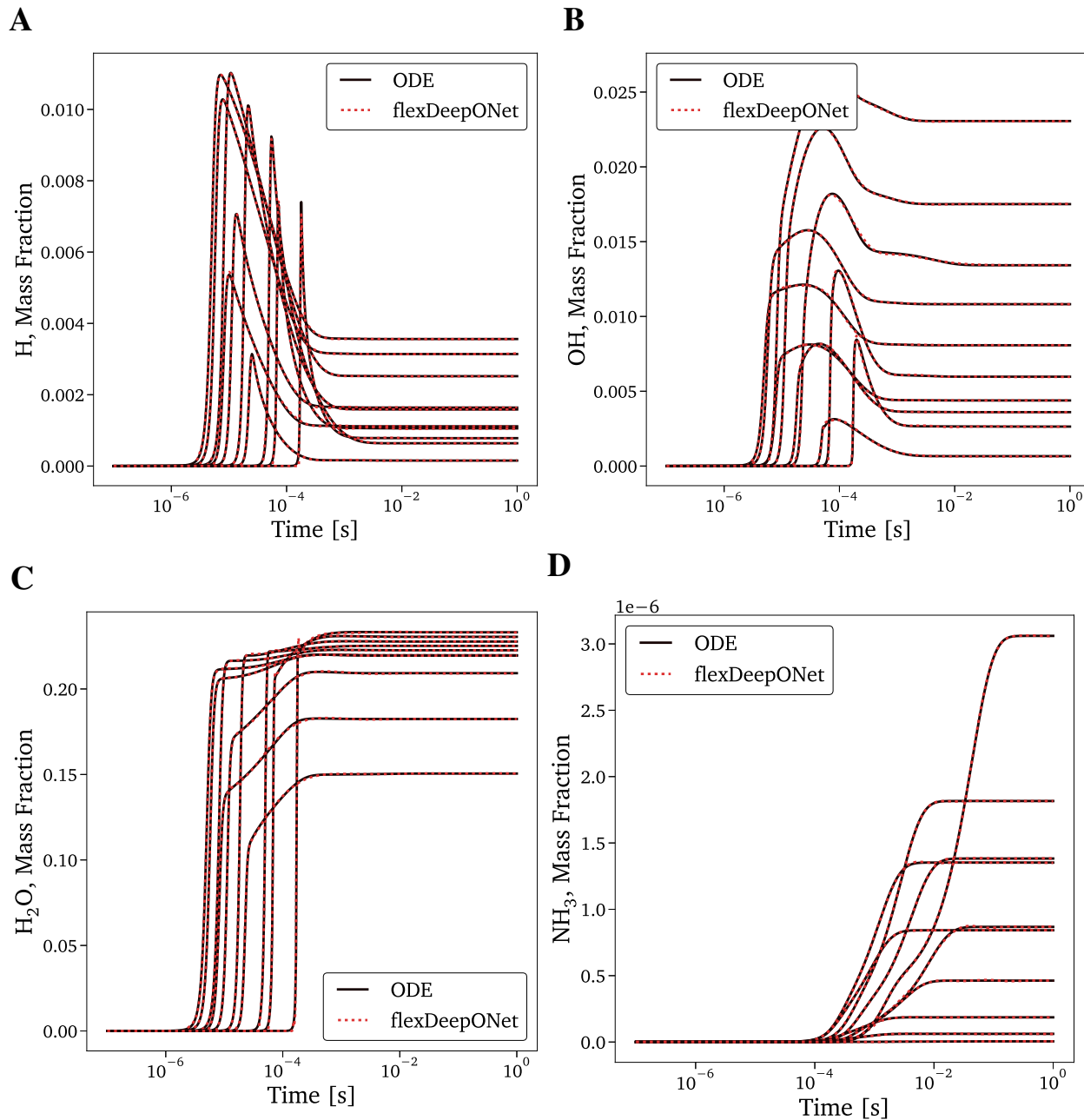
S3.4. *flexDeepONet*

Figure S24: **FlexDeepONet** predictions of the thermodynamic variables. H (A), OH (B),  $H_2O$  (C), and  $NH_3$  (D) mass fractions for ten test scenarios as the results of the ODE integration (solid black lines) and as predicted by flexDeepONet (red dotted lines).

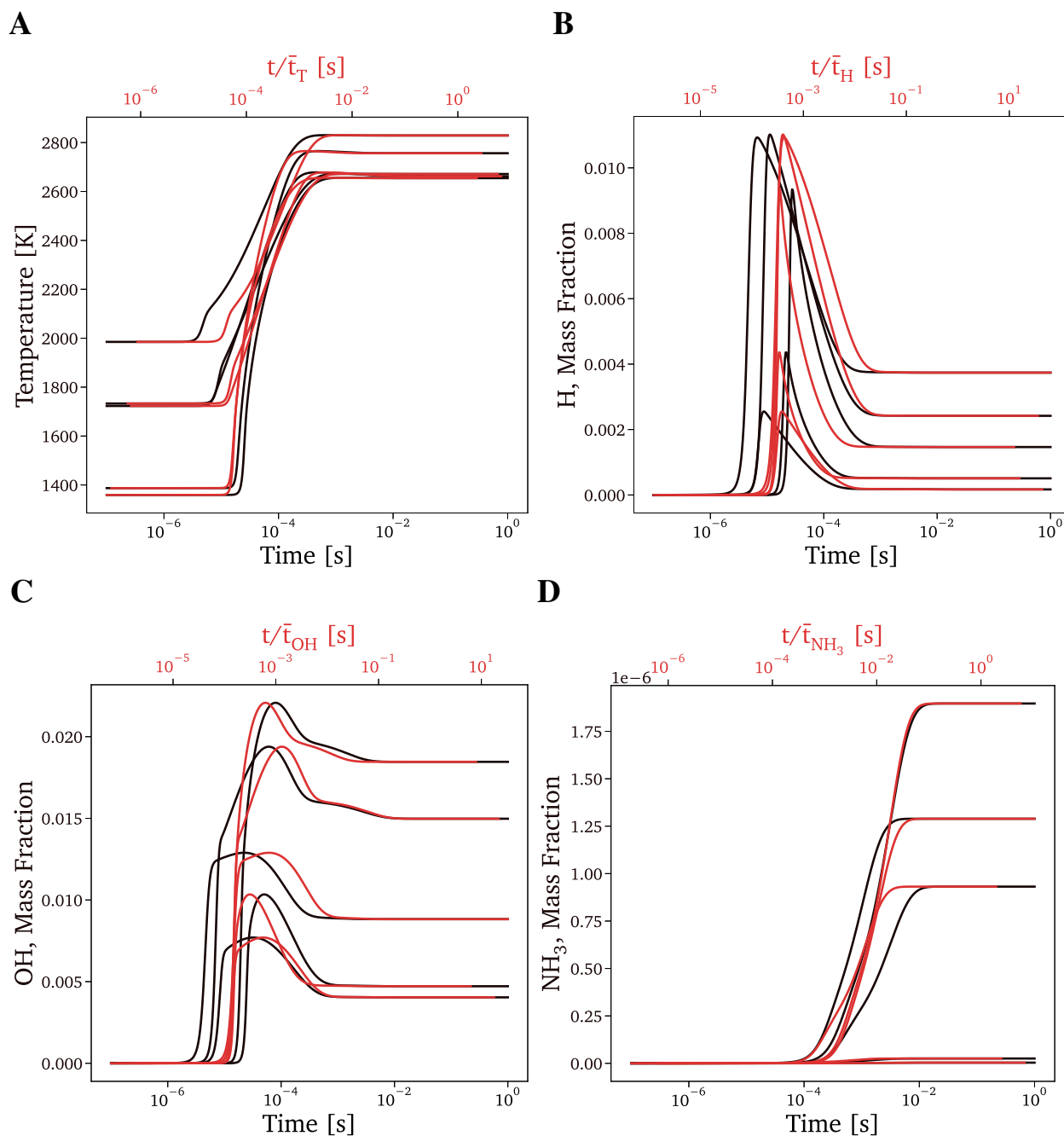


Figure S25: **Contributions of the shift net to the scenario alignment.** Time-integrated temperature (A) and H (B), OH (C), and  $NH_3$  (D) mass fractions for some of the test scenarios as functions of the simulation time (black lines) and of the simulation time corrected by the stretch net (red lines).

## S3.5. Comparisons of Test Errors

Thermodynamic Variable	$k$ for 99% Cumulative Energy	Vanilla DeepONet $p = 20$	Vanilla DeepONet $p = 32$	FlexDeepONet
Temperature	20	6.5343	4.8777	1.6221
H <sub>2</sub> , Mass Fraction	40	4.8288e-04	4.0068e-04	8.4160e-05
H, Mass Fraction	59	7.3692e-05	5.8817e-05	2.2152e-05
O, Mass Fraction	59	1.0889e-04	9.4795e-05	3.2952e-05
O <sub>2</sub> , Mass Fraction	50	1.6776e-03	1.2024e-03	3.3926e-04
OH, Mass Fraction	43	9.3048e-05	7.4898e-05	4.4956e-05
H <sub>2</sub> O, Mass Fraction	45	1.7943e-03	1.2758e-03	4.4578e-04
HO <sub>2</sub> , Mass Fraction	68	1.0318e-06	9.7360e-07	4.7141e-07
H <sub>2</sub> O <sub>2</sub> , Mass Fraction	73	9.0057e-08	6.6456e-08	2.7920e-08
N, Mass Fraction	21	4.3961e-09	4.1303e-09	4.6392e-09
NH, Mass Fraction	12	7.2799e-10	6.9256e-10	1.1066e-09
NH <sub>2</sub> , Mass Fraction	6	3.2438e-10	2.9449e-10	4.7751e-10
NH <sub>3</sub> , Mass Fraction	7	1.3849e-09	1.2024e-09	2.3153e-09
N <sub>2</sub> H, Mass Fraction	55	1.6741e-09	1.1895e-09	4.8906e-10
NO, Mass Fraction	5	4.3394e-06	4.4647e-06	9.7594e-06
NO <sub>2</sub> , Mass Fraction	5	3.2447e-09	2.8758e-09	5.0837e-09
N <sub>2</sub> O, Mass Fraction	25	1.0795e-09	1.2455e-09	1.5516e-09
HNO, Mass Fraction	5	4.9636e-10	4.7546e-10	6.8450e-10
N <sub>2</sub> , Mass Fraction	1	6.2394e-05	2.1945e-05	5.6685e-05

Table S1: **DeepONets' prediction errors.** Comparisons of the root mean squared errors (RMSE) from the vanilla DeepONets and flexDeepONet's predictions for the ten test scenarios. The second column contains the number of singular values to be retained in order to preserve 99% of the training data's cumulative energy.

#### S4. Supplementary Material for Test Case 4

##### S4.1. Equations of Motion and Data

The fourth test case is created based on the following equations in space coordinates ( $x$  and  $y$ ) and time ( $t$ ):

$$z(x, y; t) = \exp\left(z_x(x, y; t) + z_y(x, y; t)\right) z_s(t), \quad (18)$$

where:

$$z_s(t) = z_0 + v_z t. \quad (19)$$

$z_x(x, y; t)$  and  $z_y(x, y; t)$  are defined as:

$$\begin{cases} z_x(x, y; t) = \frac{1}{2} \tanh\left(a_x(x_I + l_x)\right) + \frac{1}{2} \tanh\left(b_x(x_I - l_x)\right) \\ z_y(x, y; t) = \frac{1}{2} \tanh\left(a_y(y_I + l_y)\right) + \frac{1}{2} \tanh\left(b_y(y_I - l_y)\right). \end{cases} \quad (20)$$

The  $x_I(x, y; t)$  and  $y_I(x, y; t)$  (i.e., the coordinates in the rotated-shifted-translated reference frame) are obtained from  $x$  and  $y$  (i.e., the original reference frame's coordinates) via:

$$\begin{bmatrix} x_I(x, y; t) \\ y_I(x, y; t) \end{bmatrix} = s(t) \begin{bmatrix} \cos \theta(t) & -\sin \theta(t) \\ \sin \theta(t) & \cos \theta(t) \end{bmatrix} \begin{bmatrix} x \\ y \end{bmatrix} + \begin{bmatrix} x_c(t) \\ y_c(t) \end{bmatrix}, \quad (21)$$

where the rotation angle,  $\theta(t)$ , is defined as:

$$\theta(t) = \theta_0 + v_\theta \cos(\omega_\theta t + \phi_\theta). \quad (22)$$

Additionally, the stretching factor,  $s(t)$ , is given by:

$$s(t) = s_0 + v_s \sin(\omega_s t + \phi_s). \quad (23)$$

Finally, the shifting coefficients,  $x_c(t)$  and  $y_c(t)$ , are constructed as:

$$\begin{cases} x_c(t) = x_{c_0} + v_\xi \xi(t) * \cos(\xi) \\ y_c(t) = y_{c_0} + v_\xi \xi(t) * \sin(\xi), \end{cases} \quad (24)$$

where  $\xi(t) = \omega_\xi t$ . The values of the equation parameters are reported in Table S2.

Name	Value
$z_0$	1
$v_z$	0.2
$l_x$	8
$l_y$	6
$a_x$	10
$b_x$	10
$a_y$	10
$b_y$	10
$\theta_0$	0
$v_\theta$	$\pi$
$\omega_\theta$	$\frac{2\pi}{t_{End}} \pi$
$t_{End}$	10
$\phi_\theta$	2
$s_0$	2
$v_s$	1
$\omega_s$	$\frac{2\pi}{t_{End}} \pi$
$\phi_s$	0
$x_{c_0}$	1
$y_{c_0}$	-0.5
$v_\xi$	0.5
$\omega_\xi$	$\frac{5\pi}{18}$

Table S2: Equation parameters used for generating the fourth test case.

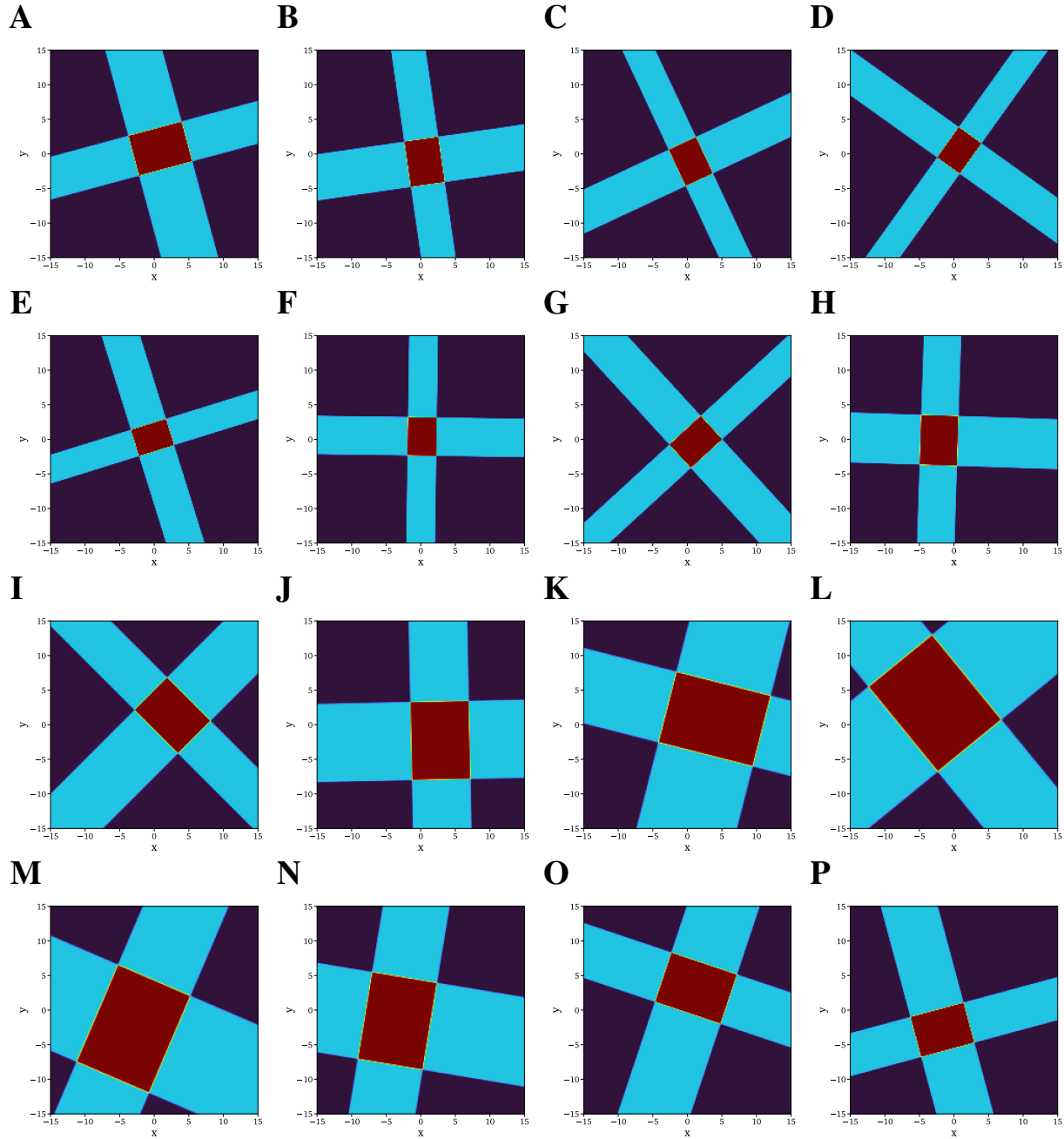


Figure S26: Some of the time snapshots for the dynamics of the rotating-translating-stretching rigid body. The snapshots are produced at sixteen time instants uniformly spaced between  $t = 0$  [s] and  $t = 10$  [s].

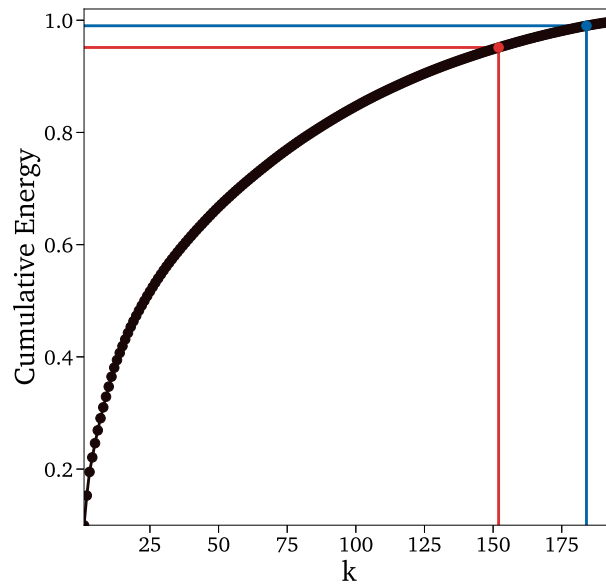
*S4.2. Proper Orthogonal Decomposition (POD)*

Figure S27: **Cumulative energies of the  $[400,000 \times 200]$  time-aggregated snapshots matrix from the rotating-translating-stretching rigid body test case.** Cumulative energies contained in the first  $k$  singular values. The red and blue dots identify cumulative energies corresponding to 95% and 99%, respectively.

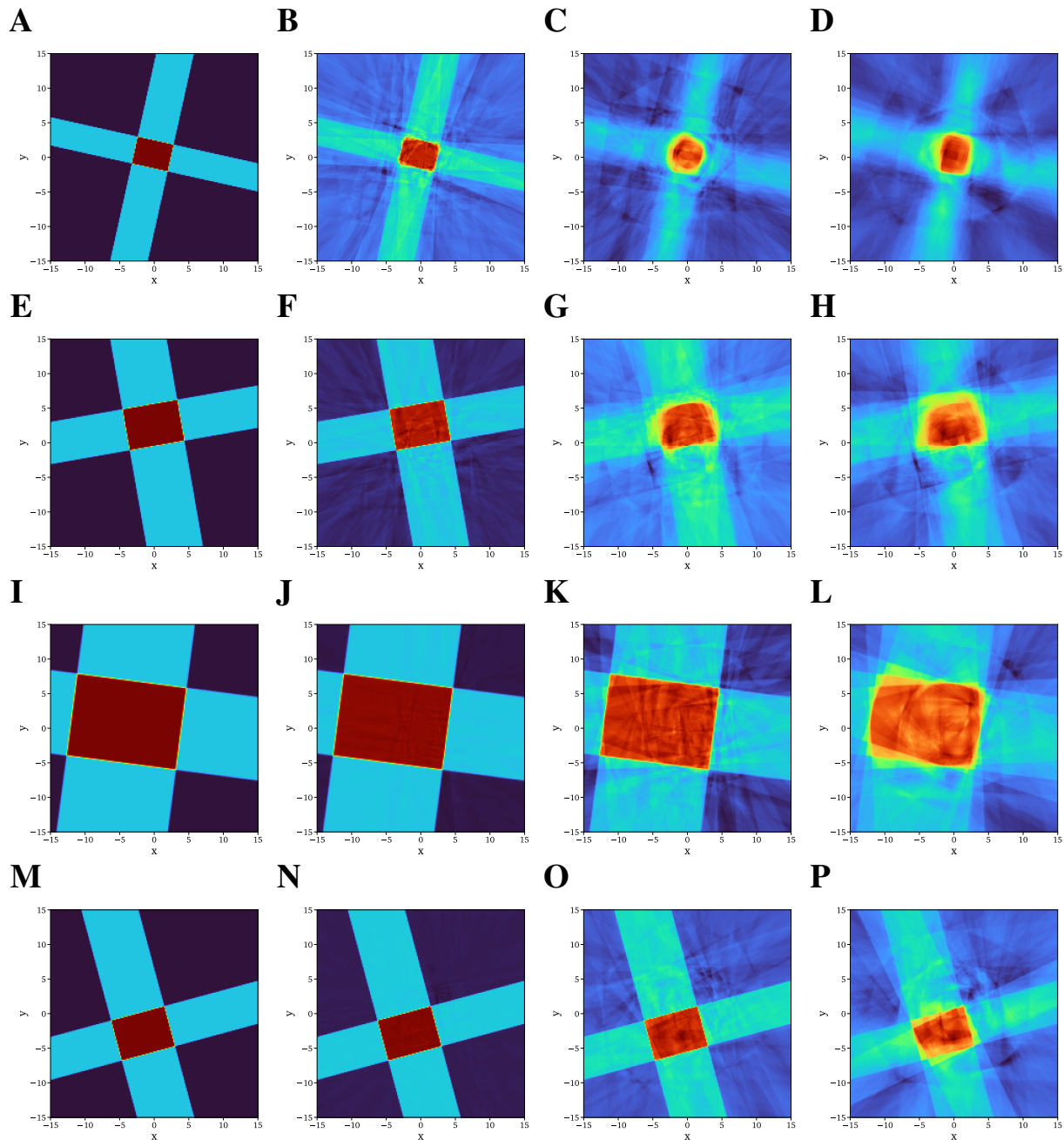


Figure S28: **Time snapshots decomposed and reconstructed via POD.** Four of the time snapshots as generated by the original equations (first column from the left) and after being encoded-decoded based on POD's first 128, 64, and 32 modes (second, third, and fourth columns, respectively). The time snapshots are taken at  $t = \{2.5, 5, 7.5, 10\}$  [s] (rows from top to bottom).



## S4.3. Vanilla DeepONet

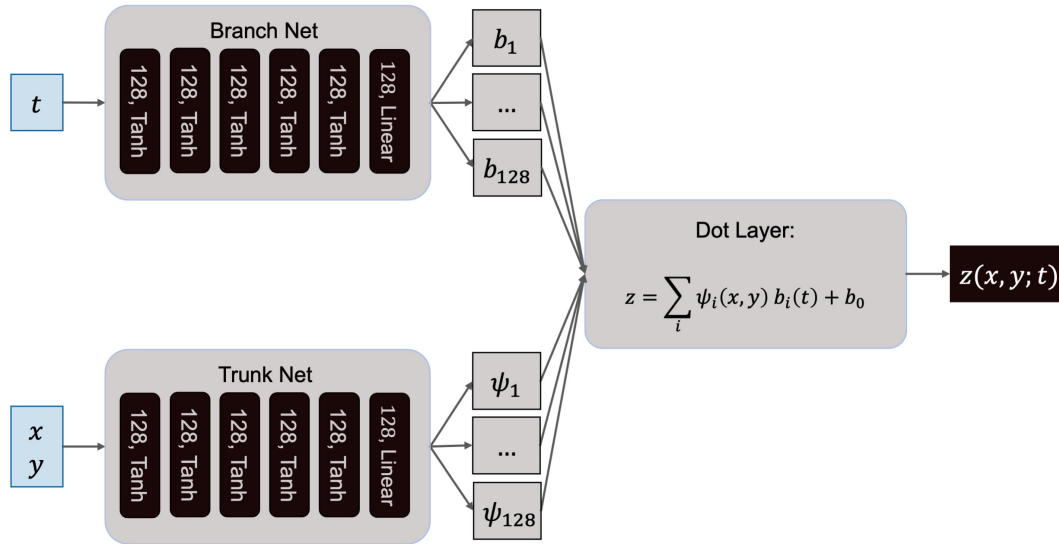


Figure S29: **Architecture of the vanilla DeepONet for the rotating-translating-stretching rigid body test case.** Note: the combination of hyperbolic tangent and exponential activation functions is here employed consistently with the test cases' generative equations.

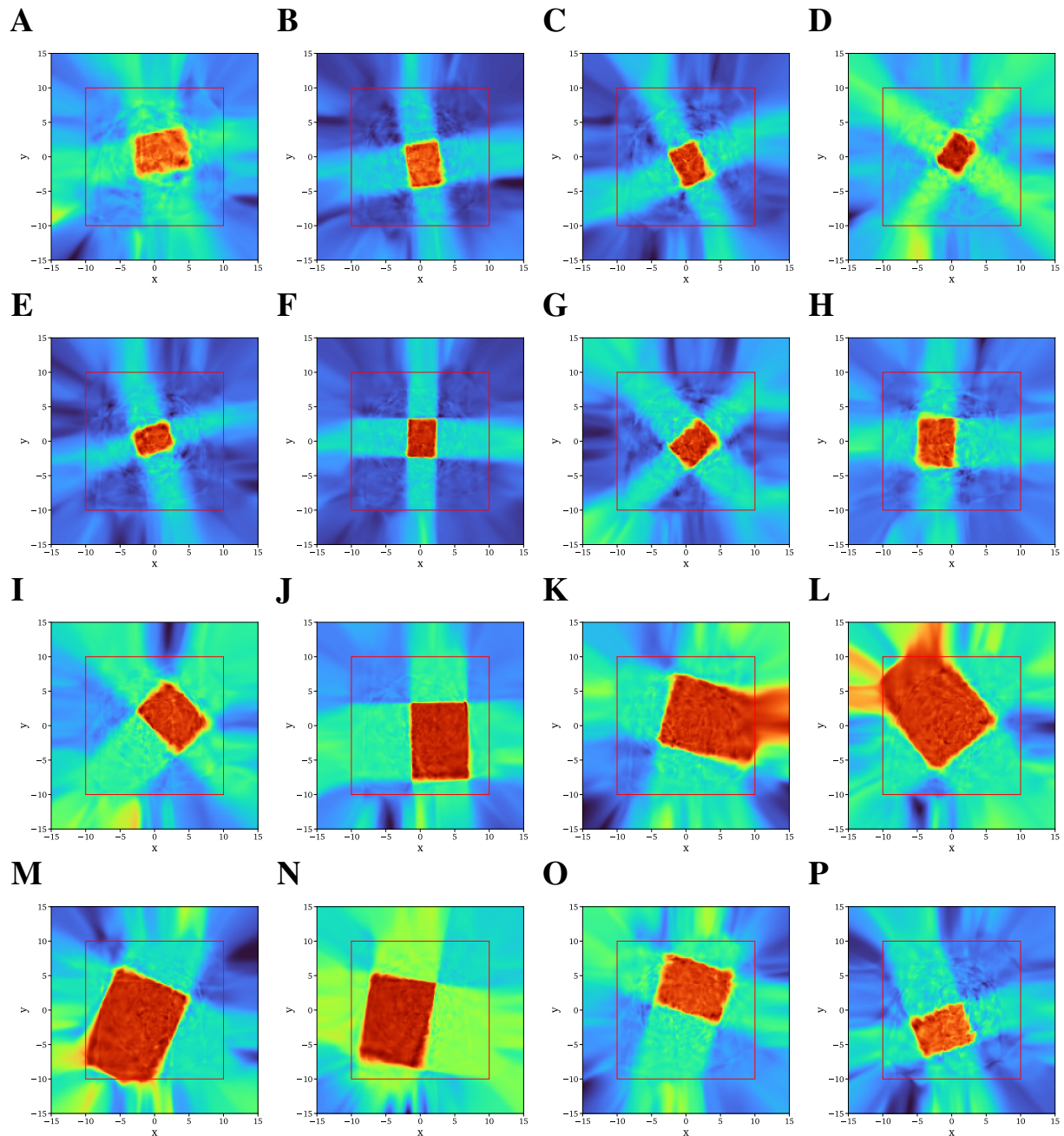


Figure S30: **Vanilla DeepONet predictions of the rigid body's dynamics.** The snapshots are produced at sixteen time instants uniformly spaced between  $t = 0$  [s] and  $t = 10$  [s]. Note: the training of the vanilla DeepONet relied only on data randomly selected inside the  $x - y$  domain represented by the red squares. Predictions outside the red squares are extrapolations.

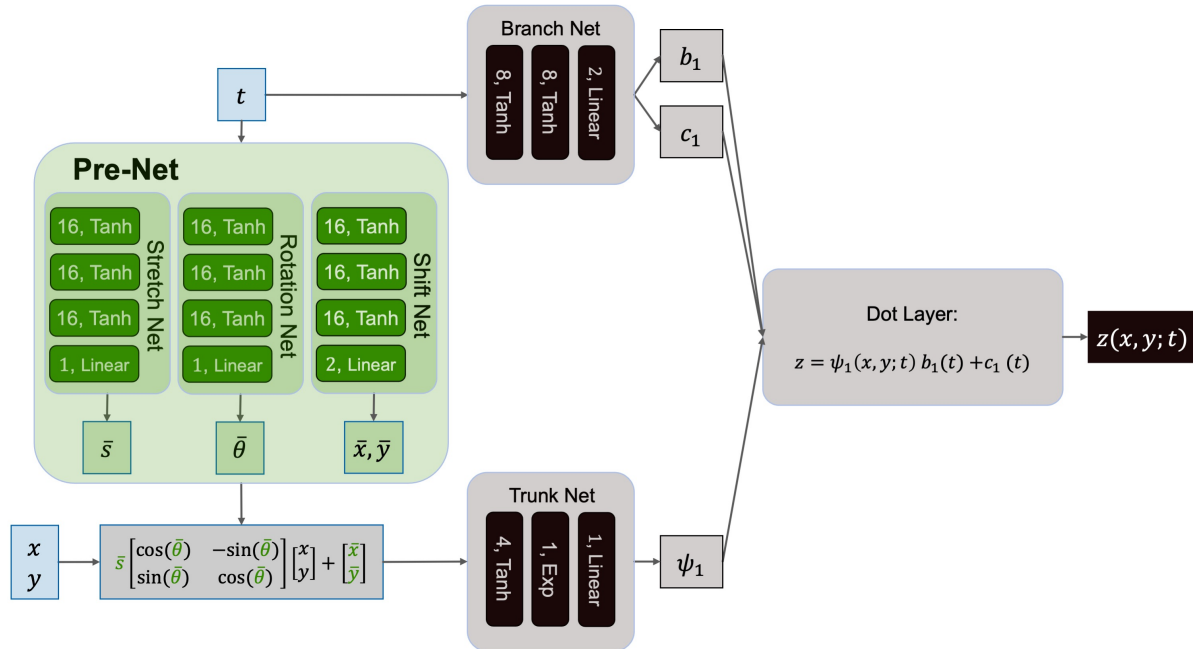
S4.4. *flexDeepONet*

Figure S31: **FlexDeepONet architecture for the rotating-translating-stretching rigid body test case.** A pre-net composed of three separate blocks is introduced to guarantee the alignment of the different time snapshots. An additional neuron is added to the output layer of the branch net to permit time-dependent centering. Note: the combination of hyperbolic tangent and exponential activation functions is here employed consistently with the test cases' generative equations.

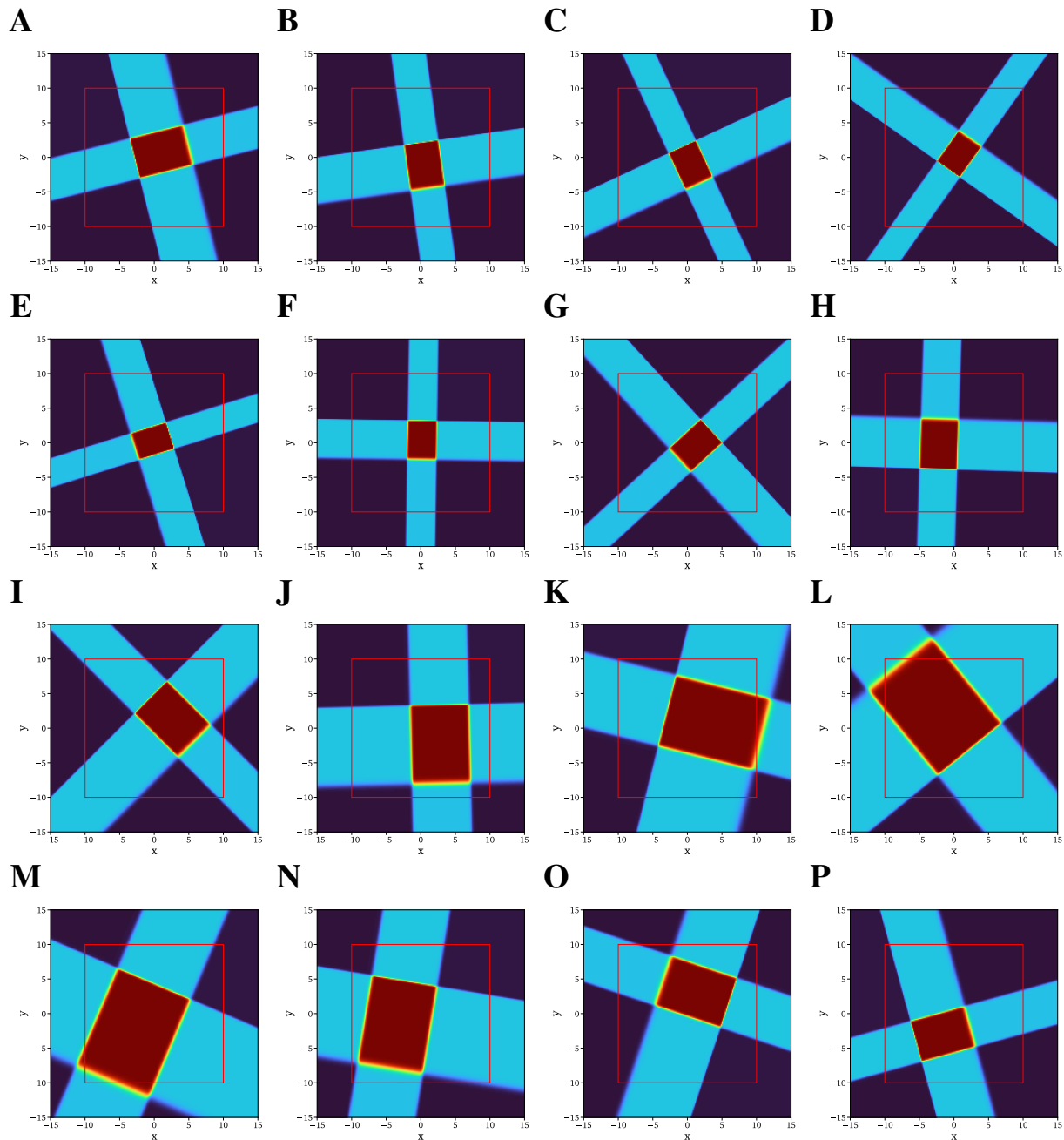


Figure S32: **FlexDeepONet predictions of the rigid body's dynamics.** The snapshots are produced at sixteen time instants uniformly spaced between  $t = 0$  [s] and  $t = 10$  [s]. Note: FlexDeepONet's training relied only on data randomly selected inside the  $x - y$  domain represented by the red squares. Predictions outside the red squares are extrapolations.